

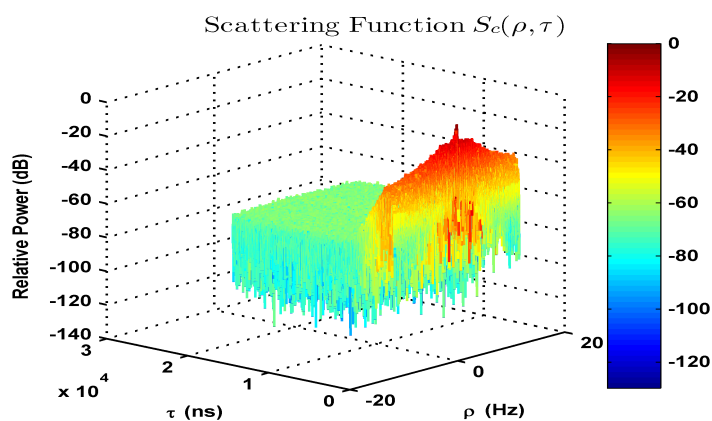
THESIS FOR MASTER OF SCIENCE IN COMMUNICATION ENGINEERING

CHALMERS



Wireless channel characterization of the reverberation chamber at NIST

SYED MIR HAIDER ALI SHAH



Antenna Research Group

Department of Signals and System

CHALMERS UNIVERSITY OF TECHNOLOGY

Gothenburg, Sweden 2011

Wireless channel characterization of the reverberation chamber at NIST

Syed Mir Haider Ali Shah

Copyright © Syed Mir Haider Ali Shah, 2011.

Department of Signals and System

Antenna Research Group

Antenna Division

Chalmers University of Technology

SE-412 96 Gothenburg, Sweden

Phone: +46 (0)31-772 10 00

Author e-mail: hyder.a.shah@gmail.com

Cover:

Chalmers University Logo

Scattering function in a reverberation chamber

Printed by Chalmers

Gothenburg, Sweden 2011

Wireless channel characterization of the reverberation chamber at NIST

Syed Mir Haider Ali Shah

Antenna Division, Chalmers University of Technology

ABSTRACT

This study is to show that a reverberation chamber can be used as a controlled facility for evaluating over-the-air performance of wireless devices in a Rayleigh and Rician fading environment. A reverberation chamber is a metallic cavity that is stirred to emulate a Rayleigh fading environment. Frequency domain techniques have been used to study and characterize the wireless channel in the chamber at the National Institute of Standards and Technology (NIST), Boulder, Colorado, USA. It is shown that by loading the chamber with radio frequency absorber blocks, the delay spread of the channel can be changed. This gives a degree of freedom to emulate a channel with desired coherence bandwidth and to study the performance of modulated signals in narrowband and wideband fading channels.

Stirrers are used in the chambers to stir the electromagnetic fields. It is determined that the speed of the stirrers can be controlled to obtain a certain Doppler spread in the channel. This gives a second degree of freedom to control the coherence time of the channel and study the effect of fast and slow fading channels on modulated signals. The Rician K-factor plays an important role in wireless communication and determines the type of fading environment and its effects on the bit-error-rate (BER) performance of a modulated signal. K-factor gives a third degree of freedom to control the delay spread of the channel inside a chamber. In propagation measurements the envelope statistics of the fading signal are usually known, therefore, a method based on maximum likelihood estimation of K-factor from the signal envelope statistics is also studied and compared with a method proposed in the literature which utilizes both amplitude and phase information usually available in laboratory designed experiments. The latter method gives more accurate results since it makes use of in-phase and quadrature components of the signal.

Finally the bit-error-rate performance of a GSM and wideband-CDMA system has been evaluated in a BlueTest chamber in narrowband and wideband fading channels by using a base station simulator at Chalmers University. Performance of binary-phase shift keying (BPSK) modulated signal is studied by using vector signal generator and analyzer in a static fading environment in the chamber at NIST.

Keywords: Channel Characterization, K-Factor, Maximum likelihood estimation, Modulated signals, Channel impairments, Emulating multipath environment, Doppler spread.

Preface

This Master of Science thesis focuses on the use of reverberation chambers as a potential repeatable wireless device testing facility. It is envisioned that in the near future the wireless industry would use reverberation chambers as a standard way of testing performance of different wireless devices, particularly those which operate in a multipath environment. The reverberation chamber serves as a reference environment for testing devices that are designed to operate in a multipath environment just as anechoic chambers are used as a reference environment for testing devices that are meant to operate in free space. This work is a joint collaboration between Chalmers University of Technology, Gothenburg, Sweden and the National Institute of Standards and Technology (NIST), Boulder, Colorado, USA.

The author is a student of Chalmers University and has been working at NIST as a guest researcher. This thesis work has been funded by NIST and the author has spent 6 months for this research. NIST has been using their reverberation chambers for electromagnetic compatibility (EMC) and electromagnetic interference (EMI) testing for more than three decades. For the past few years their research is being geared toward the use of chambers for wireless measurements. In this study the chamber at NIST has been characterized in both the time and frequency domain. It is a comprehensive study on how to use a reverberation chamber as a wireless channel emulator and tune the channel to exhibit desired properties suitable for testing a wireless device of interest. Bit-error-rate measurements have been performed by modulating a signal using laboratory grade equipment to study the channel impairments in a reverberation chamber. System level measurements have also been performed using commercially available base station simulator.

The first chapter is an introduction to reverberation chambers. The second chapter discusses how a wireless channel can be emulated in the chamber and channel parameters which should be taken into consideration. The third chapter is a study on characterizing a wireless channel in the chamber both in time

and frequency domain and discusses how to control the channel to exhibit desired properties. In the fourth chapter the chamber is tested by emulating a channel with desired properties and transmitting a modulated signal through it. The sources of errors that contribute to the received signal's bit-error-rate are identified and only the errors due to the channel itself are studied. In the last chapter this work has been summarized and future research has been proposed. The author concludes that by emulating a channel that exhibits the same properties as real world environment, the bit-error-rate performance of the modulated signal in the chamber is the same as reported in many literatures where measurements have been done in the real world environment. Concepts used in this thesis have been published in the following journal.

- ▷ Kate A. Remley, *Senior Member, IEEE*, Sander J. Floris, **Haider A. Shah** and Christopher L. Holloway, *Fellow, IEEE*, "Static- and Dynamic-Propagation-Channel Impairments in Reverberation Chambers" in *IEEE Transactions on Electromagnetic Compatibility*. (Accepted for publication)

Acknowledgments

The author would like to acknowledge all the people who have helped during this thesis with their knowledge and support and made it a successful completion. Author is grateful to examining professor Per-Simon Kildal at the Department of Signals and Systems at Chalmers University for providing with the opportunity to work at NIST and for his contribution on various topics that helped resolve conceptual problems. Thanks to Christopher L. Holloway and Kate A. Remley for their supervision and support through every step in this thesis work. A special thanks to Ryan J. Pirkl at NIST for his valuable contributions and discussion on various topics that helped a lot in learning and getting through with programming and conceptual difficulties. Kristian Carlson has been a great help during the preparatory work for this thesis at Chalmers. He helped with bit-error-rate measurements and processing of the data. I would like to thank him for his valuable discussions. Also, thanks to Chih-Ming Wang at NIST for his help regarding statistical processing and uncertainty analysis and fellow student Christian Lotback Patane for his valuable and helpful discussion regarding K-factor estimation methods.

Finally, the author would like to thank his family for their support. A special thanks to my parents who have been great support throughout my life and studies especially during this time I have spent at Chalmers and NIST.

Thanks to all for everything that you have done for my career, and for this thesis. Finally, I would like to thank God for making everything a success.

Syed Mir Haider Ali Shah
Gothenburg, February 2011

Contents

Abstract	i
Preface	iii
Acknowledgments	v
I THESIS REPORT	1
1 Introduction	3
1.1 The Reverberation Chamber	3
2 Emulating a Wireless Channel in RC	7
2.1 Measurement Setup	8
2.2 Emulating Rayleigh and Rician channel	9
2.3 K-Factor estimation by Maximum Likelihood	13
2.4 Effective number of samples for estimation of K-factor	23
2.5 Uncertainty in estimation of K-factor	26
2.6 Conclusion	29
3 Characterization of a Wireless Channel in RC	31
3.1 Time-Varying Channel Impulse Response	31
3.2 Frequency Domain Technique for Channel Sounding	32
3.3 Impulse response of a Rayleigh Fading Channel	32
3.3.1 Power Delay Profile	37
3.4 Impulse response of a Rician Fading Channel	44
3.5 Coherence Bandwidth	46
3.5.1 Measurements in reverberation chamber	47

3.6	Coherence Time	53
3.6.1	Measurements in reverberation chamber	54
3.6.2	Fading	60
3.7	Fast fading	65
3.8	Slow fading	65
3.9	Level Crossing Rate	66
3.10	Average Fade Duration	69
3.11	Doppler Spread	70
3.12	Shape of the Doppler Spectrum	74
3.12.1	Measurements in reverberation chamber	75
3.13	Conclusion	80
4	Channel Impairments in RC	87
4.1	Modulated signal measurements in NIST chamber	87
4.2	Modulated signal measurements in BlueTest chamber	91
4.3	Conclusion	95
5	Summary	97
II	Appendices	103
A	Characterization of a Wireless Channel	105
A.1	Characterization of Wireless Channel	105
A.2	Time-Varying Channel Impulse Response	106
A.3	Narrowband Fading Model	107
A.3.1	Envelope and Power Distribution	109
A.3.2	Level Crossing Rate and Average Fade Duration	110
A.4	Wideband Fading Model	111
A.4.1	Power Delay Profile	112
A.4.2	Coherence Bandwidth	113
A.4.3	Coherence Time	114
A.4.4	Doppler Spread	115
B	Fourier Theory	117
B.1	Frequency Sampling	117

<i>CONTENTS</i>	ix
C Electromagnetic Theory of RC	121
C.1 Quality Factor of the Reverberation Chamber	121

List of Figures

1.1	BlueTest Chamber (1.9 m * 2.0 m * 1.4 m)	4
1.2	NIST Chamber (2.9 m * 4.2 m * 3.6 m)	4
2.1	Measurement Setup at NIST.	9
2.2	Scatter Plot of Measured S_{21} for two cross-polarized antennas in NIST RC at 2 GHz	10
2.3	Scatter Plot of Measured S_{21} for two co-polarized antennas in NIST RC at 2 GHz	11
2.4	PDFs of Measured S_{21} for two co and cross polarized antennas in NIST RC at 2 GHz	14
2.5	Estimated K-Factor for co-polarized and cross-polarized antenna configurations	18
2.6	Estimated K-factor after 3 point moving averaging ν for cross- polarized antenna configuration	19
2.7	Estimated σ for co-polarized and cross-polarized antenna config- uration	20
2.8	Estimated $2\sigma^2$ for co-polarized and cross-polarized antenna con- figuration	21
2.9	Estimated ν for co-polarized and cross-polarized antenna config- uration	21
2.10	Estimated ν after 3 point moving averaging window for cross- polarized antenna configuration	22
2.11	Mean of K-factor estimate Vs Number of channel realizations . .	24
2.12	Standard deviation of K-factor estimate Vs Number of channel realizations	25

2.13	Estimated parameters by MLE with 95% confidence intervals, using simulated data with $K=3.5$ dB ($\nu = -13.7$ dB , $\sigma = -16.9$ dB) .	28
2.14	Standard error in K factor estimation	28
3.1	Graphical illustration of Measurement Setup at NIST.	33
3.2	Effect of signal BW on the estimation of channel impulse response	35
3.3	Power delay profile in linear scale averaged over 100 stirrer position for a bandwidth of 5.2 GHz.	36
3.4	Power delay profile in logarithmic scale	36
3.5	Power delay profile in linear scale after discarding the charging time samples	39
3.6	Power delay profile in logarithmic scale after discarding the charging time samples	39
3.7	Power delay profile in logarithmic scale for 0 and 1 Absorber case with no Aliasing	41
3.8	Power delay profile in logarithmic scale for all loading cases with no Aliasing	42
3.9	Simulated Power Delay Profiles to show that the combination of the two power delay profiles is dominated by the one with greater value of τ	42
3.10	Power delay profile in logarithmic scale for all loading cases with average $K=5$ dB	46
3.11	Coherence BW for loading 5 and 3 over 20 MHz BW at center frequency of 1520 MHz	48
3.12	Coherence BW for loading 1 and 0 over 5 MHz BW at center frequency of 1502.5 MHz	49
3.13	Coherence BW for all loadings over 1 GHz bandwidth	50
3.14	Coherence BW for all loading over 5 GHz Bandwidth	50
3.15	Coherence BW for loading 3 and 5 over 40 MHz in the presence of LoS component	51
3.16	Coherence BW for loading 0 and 1 over 5 and 20 MHz respectively in the presence of LoS component	52
3.17	RMS Delay spread calculated from PDP and Coherence bandwidth	52
3.18	Autocorrelation function of the channel with both stirrer 1 and 2 revolving continuously at RPM 1	57

3.19	Autocorrelation function of the channel with both stirrer 1 and 2 revolving continuously at RPM 8	58
3.20	Autocorrelation function of the channel at 2 GHz with all stirrer configurations	58
3.21	Coherence time as a function of frequency and stirrers speeds . .	60
3.22	Coherence time as a function of Loading	60
3.23	Coherence time as a function of stirrers	62
3.24	Channel fluctuations (Fading) for different stirrer configuration @ 2 GHz	63
3.25	Channel fluctuations for different CW frequencies when both the stirrers are moving at RPM 8, Threshold is defined at $\rho = \sqrt{0.5}$.	63
3.26	Envelop Level Crossing Rate for all stirrers configuration at different threshold levels, ρ	67
3.27	Envelop average fade duration for all stirrer configuration at different threshold levels, ρ	70
3.28	Average Doppler spread in the Reverberation Chamber	74
3.29	Doppler spread as a function of Frequency and Stirrers speed for configuration 1 and 2	76
3.30	Doppler spread as a function of Frequency and Stirrers speed for configuration 3	76
3.31	Doppler spread as a function of Stirrer configurations	77
3.32	Autocorrelation of Channel for stirrer configuration 3 and RPM 8	78
3.33	Jakes and Fixed Wireless Communication Doppler spectrum's at $F_{D_{max}}$ 100 Hz and 20 Hz respectively	79
3.34	Convolution of the Jakes and Fixed Wireless Communication Doppler spectrum's. A typical Double Rayleigh channel Doppler spectrum	80
3.35	Doppler spread as a function of Loading	81
4.1	Channel Variations in time and frequency for loading 3	88
4.2	Auto-Correlation of the bit sequence	89
4.3	Performance of BPSK modulated signal at 24.3 kbps in static and dynamic channel environment in the reverberation chamber . . .	90
4.4	Measurement setup at Chalmers	91
4.5	TIS and AFS measurement in BlueTest chamber	92

4.6	Effect of Loading and Doppler shift on BER performance of GMSK modulated signal in BlueTest chamber. 'Q' is used to indicate that stirrers are moving at quarter of the maximum speed settings . . .	93
4.7	Performance of Sony Ericsson T700 in WCDMA and GSM mode, in a multipath fading environment	94
5.1	Channel Gain as a function of Loading	100
A.1	Big Picture of the WSS Uncorrelated Scattering from Erik Strom lecture slides in the course of Wireless Communication at Chalmers University	112
A.2	Typical scattering function in the Reverberation Chamber	113
B.1	(a) Time domain signal with no aliasing (b) Time domain signal with aliasing	119
C.1	Chamber Quality Factor as a function of Frequency and Loading	123

Part I

THESIS REPORT

1

Introduction

1.1 The Reverberation Chamber

In the recent years a wide range of applications for wireless devices have emerged. Wireless technology, like SIMO and MIMO systems, are under development. Consequently, the demand from the industry for an accurate, repeatable and efficient test facility for such devices has increased significantly during the latest years. The reverberation chamber, originally designed for electromagnetic compatibility measurements, has gone through a significant development in order to meet these requirements [1] [2]. A reverberation chamber (also called mode-stirred chamber) is basically a shielded room (metallic walls) with an arbitrarily shaped metallic rotating paddles (stirrers or tuners). The paddles are designed to be non-symmetric and are used to create continuously changing boundary conditions of EM fields in the chambers. Figure (1.1) and (1.2) shows a typical rectangular reverberation chambers with different sizes and stirrers shapes.

Without the rotating paddles, the EM fields in the chamber would be distributed in a fixed set of modes [3]. These modes would result in maximum and minimum field amplitudes (i.e. hot and cold spots) throughout the chamber. On the other



Figure 1.1: *BlueTest Chamber (1.9 m * 2.0 m * 1.4 m)*



Figure 1.2: *NIST Chamber (2.9 m * 4.2 m * 3.6 m)*

hand, if the paddles are continuously stepped or rotated, then all locations in the chamber tend to experience similar maxima and minima of the field amplitudes. In [3] and [4], it is shown that if the chamber is large enough to interact with

and perturb a large number of modes in the chamber, then the real and imaginary parts of the rectangular components of the electric and magnetic field through out the chamber are Gaussian distributed, independent with identical variances. The amplitude of a rectangular component of the electric or magnetic field adheres to either a Rician or Rayleigh probability density function.

The type of distribution (Rician or Rayleigh) is a result of the different characteristics of the chamber and/or antennas used. The statistics of the field in a reverberation chamber are obtained by rotating the paddles. At every point the field will vary from maximum to minimum as the paddles make one rotation, but at each point the field will have some mean value. In this thesis we studied the use of reverberation chamber to develop a controllable test facility that can be used to test wireless devices in a Rayleigh and a wide range of desired Rician multipath propagation environments. The K-factor of the Rician distribution can be used to describe the characteristic of reverberation chambers and antennas. In Chapter 2 it is studied that any desired and repeatable K-factor can be obtained by controlling different parameters in the experiment design. Also a method based on maximum likelihood estimation has been studied to determine the K-factor in the channel by use of the channel amplitude statistics. In laboratory experiments, usually both the amplitude and phase information of the channel is available from the vector network analyzer but for propagation measurement scalar signal analyzers are mostly used. Thus, a method based on amplitude statistics is useful for such measurements.

The method based on maximum likelihood estimation is compared to the conventional method used at NIST, which utilizes S-parameter data directly and uses both amplitude and phase information for K-factor estimation [5]. This method provides more reliable results than other methods which estimates the K-factor based on channel amplitude statistics only. The uncertainty in the maximum likelihood estimation of K-factor is addressed and the minimum number of samples needed for the reliable estimation are studied. In general the measurement procedure involves exposing a Device Under Test (DUT) to a statistical ensemble of field configurations generated by stepping or rotating the stirrers through a large number of positions.

Chapter 3 discusses in detail how the measurements in a reverberation chamber are performed. The data is processed to determine the power delay profile of the channel in the chamber and processing details are discussed. The coherence band-

width in the chamber is estimated and the relation between RMS delay spread and coherence bandwidth is determined. It is important to know the frequency selective behaviour of the channel in order to study its effects on modulated signals. Different parameters that can be adjusted to control the coherence bandwidth and RMS delay spread have been studied. Time selective behaviour of the channel is also studied and coherence time and Doppler spread of the channel are estimated. The parameter which can be used to control the time selectivity in the channel are also studied in this chapter. It is a comprehensive study on how to use a reverberation chamber for emulating a wireless channel with desired delay and Doppler spread.

In Chapter 4 the performance of GSM and W-CDMA systems have been studied in narrowband and wideband fading channels by emulating the channel with desired frequency and time domain properties in the reverberation chamber. These measurements were performed both in dynamic and static environments. BPSK modulated signal performance has also been studied in a static environment to identify the individual sources of error in the bit-error-rate of the received signal and studied only the errors introduced by the channel by eliminating all other sources of error.

Chapter 5 summarizes this study and concludes the findings. Future research topics are also suggested which will help the wireless community learn more about reverberation chambers for their use as a wireless channel emulator.

2

Emulating a Wireless Channel in RC

If we assume that both the antennas inside the reverberation chamber are directed towards each other and are co-polarized, then the total field incident on either of the Rx antenna will have contribution from two sources. The first contribution is referred to as the ‘ unstirred energy ’ which is the energy directly coupled from the Tx antenna to the Rx antenna [The Line-of-sight (LoS) component, or the direct coupling term]. The second contribution is referred to as the ‘ stirred energy ’ which results from all the other energy radiating from the Tx antenna and interacting with the paddles. This include the energy that reflects off the chamber walls and then interacts with the paddles/stirrers. It is assumed that the only unstirred component is the direct coupling term from the transmitting antenna. This assumption is best satisfied for large chambers and large, effective stirrers. It is a reasonable assumption as long as the mode density is significantly large and the paddles are large enough to interact significantly with all modes [3] . In such a case the electric or magnetic field distribution in the chamber is derived in [5] and is given as,

$$f(|E_{\Theta}|) = \frac{|E_{\Theta}|}{\sigma^2} I_0\left(\frac{|E_{\Theta}||E_{d\Theta}|}{\sigma^2}\right) * \exp\left(-\frac{|E_{\Theta}|^2 + |E_{d\Theta}|^2}{2\sigma^2}\right) U(|E_{\Theta}|) \quad (2.1)$$

where E_Θ is the Θ component of the total electric field, Θ is the elevation angle in a standard spherical coordinate system centered at the transmitting antenna. The total Θ component of electric field can be written as the sum of the stirred (s) and unstirred (d) components.

$$E_\Theta = E_{s\Theta} + E_{d\Theta} \quad (2.2)$$

I_0 is the modified Bessel function of zero order and U is the unit step function.

$$U(|E_\Theta|) = \begin{cases} 1, & |E_\Theta| > 0 \\ 0, & |E_\Theta| < 0 \end{cases} \quad (2.3)$$

Rice [6] derived (2.1) in a classic paper. In region where the direct component is insignificant, the magnitude of a scalar component of electric field is expected to be Rayleigh distributed, we require,

$$|E_{d\Theta}|^2 \ll 2\sigma^2 \quad (2.4)$$

where physical interpretation of (2.4) is that the power density of the direct component of the field (i.e., $|E_{d\Theta}|$) is very small compared to the stirred field power density (i.e., $2\sigma^2$, the power in the multipath components) (2.1) then reduces to a Rayleigh distribution.

$$f(|E_\Theta|) = \frac{|E_\Theta|}{\sigma^2} * \exp\left(-\frac{|E_\Theta|^2}{2\sigma^2}\right)U(|E_\Theta|) \quad (2.5)$$

Hill has shown in [3] that under ideal condition (lossless and matched antennas, ideal reverberation chamber and no direct coupling), the real and imaginary part of the currents are independent and normally distributed with zero mean and identical variances. As a result, the real and imaginary components of the stirred component will also be independent and normally distributed with zero mean and identical variances.

2.1 Measurement Setup

The measurement setup used to create Rayleigh/Rician environment in the chamber is shown in Figure (2.1). The chamber at NIST has a volume of 2.9 m x 4.2

m x 3.6 m, the paddles in the chamber can be controlled by a LABVIEW interface on a personal computer (PC), the paddles can operate in a step and continuous rotation mode. The LABVIEW interface also communicates with the Agilent Vector Network Analyzer (Model N5230C PNA-L Network) used to measure the S_{21} or complex channel transfer function between the two antennas. Measuring S_{21} is a common approach used to determine the statistical behaviour of reverberation chamber. In fact Hill have shown in [3] that the statistics of S_{21} are equivalent to the statistics of the field components in the reverberation chamber. This should be no surprise, since a measurement of this type is essentially a measure of the transfer function of a given radio environment, be it LoS, Rayleigh or Rician. In this case the S_{21} measurement gives the transfer function of the reverberation chamber and hence the environment statistics. In this setup two identical DRG horn antennas by A.H. Systems (*DRG Horn Antenna – Model SAS-571*) are used as Tx and Rx antennas.

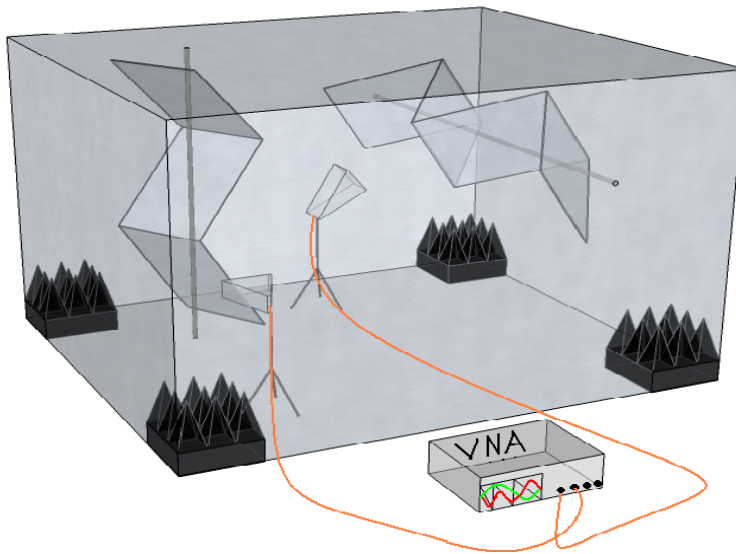


Figure 2.1: *Measurement Setup at NIST.*

2.2 Emulating Rayleigh and Rician channel

To emulate a Rayleigh environment in the chamber the two antennas are adjusted such that they are cross-polarized or they face two different stirrers on each side

of the chamber. In both the configuration it is very unlikely to have a direct (LoS) component between the Tx and Rx antenna. Figure (2.2) shows the complex distribution of the S_{21} measured in the RC, the mean is centered around zero as expected thus the envelope of Gaussian distributed real and imaginary component will result in a Rayleigh fading or channel as discussed earlier. To emulate a Rician environment in the RC the two antennas are adjusted such that they are co-polarized and facing each other in such a configuration it is made sure to have a strong LoS component between the Tx and Rx along with the scattered components, Figure (2.3) shows the distribution of the channel in the RC where mean is now shifted which indicates a strong LoS component is present. To verify the presence or absence of a LoS component there is a need to define a parameter. We study the K-factor which characterize the Rician environment and is defined as the ratio of power in direct path component to the scattered component [7].

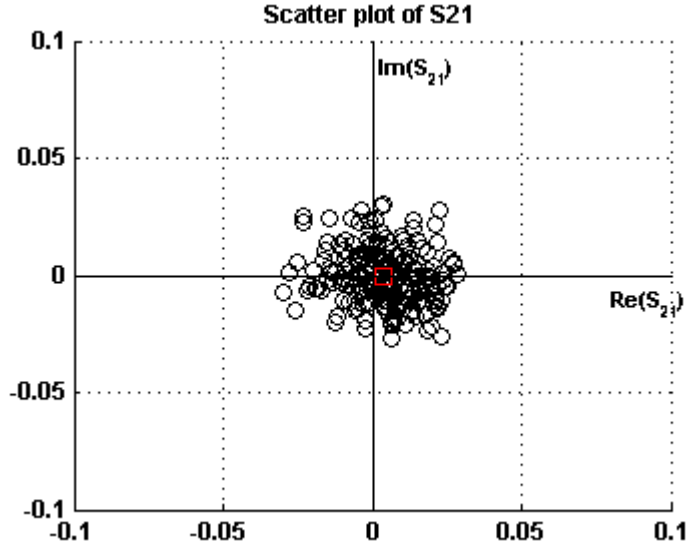


Figure 2.2: Scatter Plot of Measured S_{21} for two cross-polarized antennas in NIST RC at 2 GHz

$$K = \frac{\text{directcomponent}}{\text{scatteredcomponent}} \quad (2.6)$$

Equation (2.6) can be more specifically written in terms of electric field component give as,

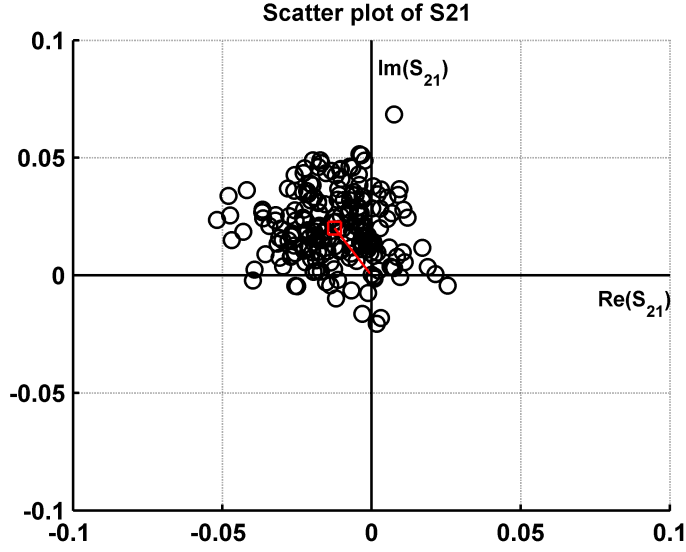


Figure 2.3: Scatter Plot of Measured S_{21} for two co-polarized antennas in NIST RC at 2 GHz

$$K = \frac{|E_{\Theta}|^2}{2\sigma^2} \quad (2.7)$$

if no direct component is present $K = 0$ ($K = -\infty$ dB) and the distribution of electric field magnitude (channel envelope) is Rayleigh. When there is no multipath ($\sigma = 0$), $K = \infty$ dB. The transfer function S_{21} can be expressed as a sum of a direct component (direct coupling term, i.e., LoS term) and a component associated with the stirred energy in the chamber as the following:

$$S_{21} = S_{21_d} + S_{21_s} \quad (2.8)$$

where S_{21_d} is the direct component and S_{21_s} is the stirred component. If no stirred component were present, S_{21} would only have a direct component which would represent a LoS environment.

$$S_{21_{LoS}} = S_{21_d} \quad (2.9)$$

This is the case usually in an Anechoic chamber. The real and imaginary component of the stirred coupling coefficient S_{21_s} , will also be independent and normally distributed with zero mean and identical variances.

$$\langle S_{21_s} \rangle = 0 \quad (2.10)$$

and

$$\begin{aligned} \text{var}[Re(S_{21_s})] &= \text{var}[Im(S_{21_s})] = \langle [Re(S_{21_s})]^2 \rangle \\ &= \langle [Im(S_{21_s})]^2 \rangle = \sigma_R^2 \end{aligned} \quad (2.11)$$

σ_R is the standard deviation measured in the reverberation chamber. On the other hand S_{21_d} has zero variance and a non-zero mean d_R ,

$$\langle S_{21_d} \rangle = d_R \quad (2.12)$$

and

$$\begin{aligned} \text{var}[Re(S_{21_d})] &= \text{var}[Im(S_{21_d})] = \langle [Re(S_{21_d})]^2 \rangle \\ &= \langle [Im(S_{21_d})]^2 \rangle = 0 \end{aligned} \quad (2.13)$$

From (2.11) and (2.13) the variance of S_{21} is given by

$$\begin{aligned} \text{var}[Re(S_{21})] &= \text{var}[Im(S_{21})] = \langle [Re(S_{21})]^2 \rangle \\ &= \langle [Im(S_{21})]^2 \rangle = \sigma_R^2 \end{aligned} \quad (2.14)$$

or they can be written as.

$$2\sigma_R^2 = \langle |S_{21} - \langle S_{21} \rangle|^2 \rangle \quad (2.15)$$

From (2.10) and (2.12), the mean value of S_{21} is related to the direct component.

$$d_R = |\langle S_{21} \rangle| \quad (2.16)$$

From (2.7), (2.12) and (2.15) the Rician K-factor can be related to S_{21} measurement in the reverberation chamber by the following equation.

$$K = \frac{d_R^2}{2\sigma_R^2} = \frac{(|\langle S_{21} \rangle|)^2}{(\langle |S_{21} - \langle S_{21} \rangle|^2 \rangle)} \quad (2.17)$$

This can be visually seen in the scattering plots in Figures (2.2) and (2.3); σ_R is the radius of the clutter of data and d_R is the distance of centroid of the clutter from the origin (shown by a red line). In Figure (2.4) the probability density functions of S_{21} measured in the case of cross-polarized (No-LoS) and co-polarized antennas (LoS) are plotted, it can also be seen that for no LoS case the pdf of channel amplitude ($|S_{21}|$) is Rayleigh distributed where as for LoS case it is a Rician pdf. From the theoretical fit the estimated K-factor for co-polarized antennas at 2 GHz is 3.21 dB where as for the cross-polarized antennas at 2 GHz, the K-factor turns out to be -64.37 dB which clearly indicates an absence of LoS component. The S_{21} measurement approach is the standard way to determine the K-factor in the reverberation chamber. In order to complement and verify this method we studied another method based on the statistics of the data ($|S_{21}|$) or more specifically on the distribution of channel envelope, with this method based on parametric estimation of a defined model, our goal is to estimate the parameter ν and σ of the Rician model which most likely produced the data from the set of probability distribution functions of the model, this is achieved by maximum likelihood estimation; an indispensable tool for many statistical modeling techniques and a preferred method of parameter estimation in statistics [8].

2.3 K-Factor estimation by Maximum Likelihood

A direct line of sight signal can effect the properties of the channel as discussed earlier, such a channel is known to have a Rician distribution [7]. A method based on moments of the channel statistics is studied to estimate the K-factor. Once a model (Rician Model) is specified with its parameters (ν, σ) and data have been collected, one is in a position to evaluate its goodness of fit, i.e. how well the model fits the observed data. Goodness of fit is assessed by finding parameter values of

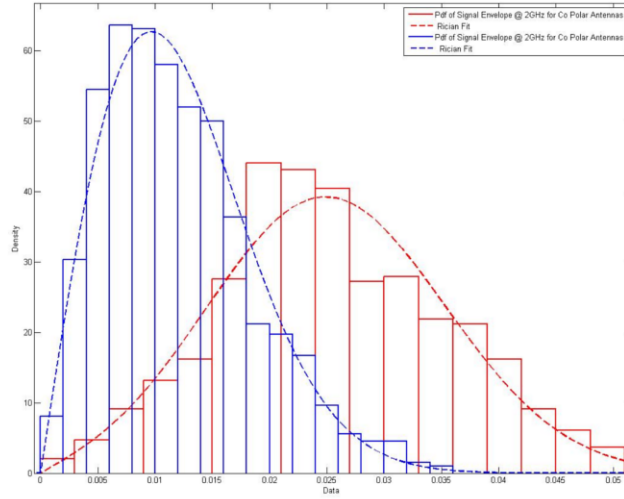


Figure 2.4: PDFs of Measured S_{21} for two co and cross polarized antennas in NIST RC at 2 GHz.

a model that best fits the data. There are two general methods for parameter estimation, the least-square estimation (LSE) and the maximum likelihood estimation (MLE). LSE, which unlike MLE requires no or minimal distributional assumptions and is useful for obtaining a descriptive measure for the purpose of summarizing observed data but it has no basis for testing hypotheses or constructing confidence intervals. MLE is a standard approach to parameter estimation and inference in statistics.

The idea behind maximum likelihood estimation is to determine the parameter that maximizes the probability (likelihood) of the sample data. From statistical point of view, the method of maximum likelihood is considered to be more robust (with some exceptions) and yields estimators with good statistical properties. MLE methods are versatile and apply to most models and to different types of data. In addition they provide efficient method for quantifying uncertainty through confidence bounds. Maximum Likelihood Estimation has many optimal properties in estimation:

- *Sufficiency* (complete information about the parameter of interest contained in its MLE estimator)

- *Consistency* (true parameter value that generated the data recovered asymptotically, i.e. for data of sufficiently large samples)
- *Efficiency* (lowest-possible variance of parameter estimates achieved asymptotically)
- *Parameterization Invariance* (same MLE solution obtained independent of the parameterization used)

Given a set of parameter values, the corresponding probability density function will show that some data are more probable than other data. In reality, however, we have already observed the data. Accordingly, we are faced with an inverse problem, given the observed data and a model of interest, find the one Pdf, among all the probability densities that the model prescribes, that is most likely to have produced the data. To solve this inverse problem, we define the likelihood function by reversing the roles of the data vector \mathbf{y} and the parameter vector \mathbf{w} in $f(\mathbf{y}|\mathbf{w})$, i.e.

$$L(\mathbf{w}|\mathbf{y}) = f(\mathbf{y}|\mathbf{w}) \quad (2.18)$$

Thus represents the likelihood of the parameters \mathbf{w} given the observed data \mathbf{y} ; and as such is a function of \mathbf{w} . There exists an important difference between the Pdf $f(\mathbf{y}|\mathbf{w})$ and the likelihood function $L(\mathbf{w}|\mathbf{y})$. The two functions are defined on different axes, and therefore are not directly comparable to each other. Specifically, the Pdf $f(\mathbf{y}|\mathbf{w})$ is a function of the data given a particular set of parameter values defined on the data scale on the other hand, the likelihood function is a function of the parameter given a particular set of observed data defined on the parameter scale. In short, $f(\mathbf{y}|\mathbf{w})$ gives us the probability of a particular data value for a fixed parameter, whereas $L(\mathbf{w}|\mathbf{y})$ tells us the likelihood (“un-normalized probability”) of a particular parameter value for a fixed data set. Once data (in this case S_{21} or the complex channel transfer function H) have been collected and the likelihood function of a model given the data is determined, one is in a position to make statistical inferences about the population, that is, the probability distribution that underlies the data. Given that different parameter values index different probability distributions, we are interested in finding the parameter value that corresponds to the desired probability distribution. The principle of maximum likelihood estimation states that the desired probability distribution is the one that makes the

observed data ‘most likely’, which means that one must seek the value of the parameter vector that maximizes the likelihood function $L(\mathbf{w}|\mathbf{y})$ (or minimizes the negative-likelihood function). MLE estimates need not exist nor be unique. In this work for computational convenience, the MLE estimate is obtained by maximizing the log-likelihood function, $\ln L(\mathbf{w}|\mathbf{y})$: This is because the two functions, $\ln L(\mathbf{w}|\mathbf{y})$ and $L(\mathbf{w}|\mathbf{y})$; are monotonically related to each other so the same MLE estimate is obtained by maximizing either one. Assuming that the log-likelihood function, $\ln L(\mathbf{w}|\mathbf{y})$; is differentiable, if \mathbf{w}_{MLE} exists, it must satisfy the following partial differential equation known as the likelihood equation:

$$\frac{\partial \ln L(\mathbf{w}|\mathbf{y})}{\partial \mathbf{w}_i} = 0 \quad (2.19)$$

at $\mathbf{w}_i = \mathbf{w}_{i,\text{MLE}}$ for all $i = 1, \dots, k$. This is because the definition of maximum or minimum of a continuous differentiable function implies that its first derivatives vanish at such points. The likelihood equation represents a necessary condition for the existence of an MLE estimate. An additional condition must also be satisfied to ensure that $\ln L(\mathbf{w}|\mathbf{y})$ is a maximum and not a minimum, since the first derivative cannot reveal this. To be a maximum, the shape of the log-likelihood function should be convex (it must represent a peak, not a valley) in the neighborhood of w_i : This can be checked by calculating the second derivatives of the log-likelihoods and showing whether they are all negative at $\mathbf{w}_i = \mathbf{w}_{i,\text{MLE}}$ for all $i = 1, \dots, k$.

$$\frac{\partial^2 \ln L(w|y)}{\partial \mathbf{w}_i^2} = 0 \quad (2.20)$$

In practice, however, it is usually not possible to obtain an analytic form solution for the MLE estimate, especially when the model involves many parameters and its Pdf is highly non-linear. In such situations, the MLE estimate must be sought numerically using non-linear optimization algorithms. The basic idea of non-linear optimization is to quickly find optimal parameters that maximize the log-likelihood. This is done by searching much smaller sub-sets of the multi-dimensional parameter space rather than exhaustively searching the whole parameter space, which becomes intractable as the number of parameters increases. The ‘‘intelligent’’ search proceeds by trial and error over the course of a series of iterative steps. Specifically, on each iteration, by taking into account the results from the previous iteration, a new set of parameter values is obtained by adding

small changes to the previous parameters in such a way that the new parameters are likely to lead to improved performance. Different optimization algorithms differ in how this updating routine is conducted. The iterative process continues until the parameters are judged to have converged on the optimal set of parameters on an appropriately predefined criterion. Examples of the stopping criterion include the maximum number of iterations allowed or the minimum amount of change in parameter values between two successive iterations.

In order to estimate the K-factor from the channel statistics, initial parameters (ν, σ) are calculated from the second and fourth moment of the data assuming the channel has a Rician distribution. The moments of Rician distribution are given by (2.21) and (2.22).

$$\mathbf{E}[X^2] = 2\sigma^2 + \nu^2 \quad (2.21)$$

$$\mathbf{E}[X^4] = 8\sigma^4 + 8\sigma^2\nu^2 + \nu^4 \quad (2.22)$$

Initial values of the parameters are estimated numerically by using the moments as the starting point of the Nelder-Mead non-linear optimizing algorithm. The stopping criteria is set to be a maximum of 200 iterations or when the difference between two consecutive estimated parameters is less than $1 \exp -6$. The parameters obtained after optimization are most likely the ones from which the data set is generated. These parameters are then used to estimate the K-factor.

Figure (2.5) shows the comparison of measured and estimated K-factor. The measured K-factor is obtained by using the conventional method used at NIST for calculating the K-factor (ratio of un-stirred to stirred energy in the RC) as described in [5]. This method is more accurate, especially for small values of K, since it makes use of the phase information or the complex channel where I/Q components are available [9]. Two standard ridged horn antennas are set up in the RC with 3 RF absorbers. Channel transfer function is measured over the frequency range of 0.8 to 6 GHz for 100 different stirrer positions such that the stirrers complete one revolution i.e, 360° , so each stirrer position is a step of 3.6° , such that averaging over the stirrer positions would give an unbiased estimate of the channel. Complex channel transfer function (S_{21}) is measured twice, when the antennas are co-polarized and secondly when the antennas are cross-polarized such that we can

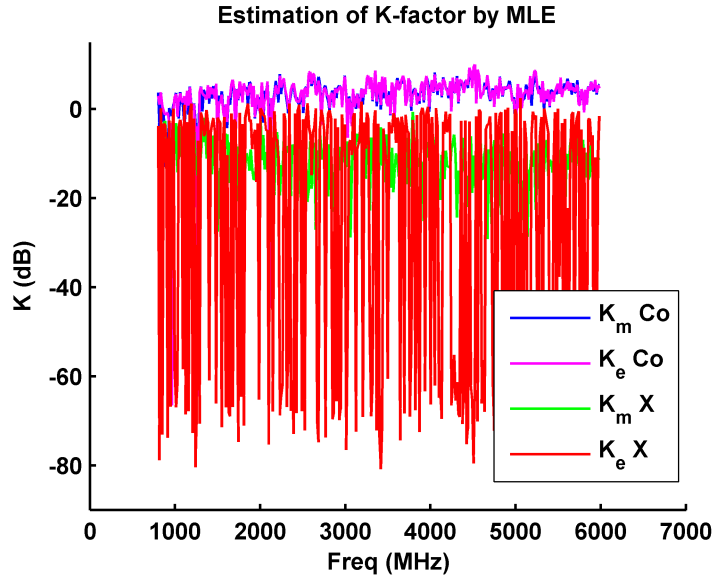


Figure 2.5: Estimated K-Factor for co-polarized and cross-polarized antenna configurations

make sure that no LoS component is present in the later case, as seen in Figure (2.5). The results from the maximum likelihood method agrees with the conventional method for the case when LoS component is present since the MLE is based on the parameter estimation of the Rician model which assumes a LoS component is present. However when the LoS component is absent the estimation based on the Rician model seems to vary a lot around the K-factor estimated by using the standard S_{21} approach for cross-polarized antenna configuration. In the absence of LoS component the K-factor is below 0 dB or 1. In linear scale it corresponds to value between 0 and 1 therefore a small fractional change in the linear value would appear to be large in the log scale. To avoid this misleading fluctuation the estimated K-factor in case of cross-polarized antennas from the Rician model is smoothed out using a 3-point moving window averaging. It can be seen from Figure (2.6) that the variations are much lesser after averaging and the K-factor is in the same order of magnitude as measured by the S_{21} approach. It is important to point out here that even though the estimation of K-factor is in the same order of magnitude which clearly indicates a weak LoS component as compared to the sum of power of all the multipath components arriving at the receiving antenna. The estimate of K-factor does not closely follow the estimate from S_{21} method which

would give a wrong value of K at one particular frequency. Maximum likelihood method is therefore not suitable for estimating K -factor for very weak LoS component when Rician model is specified. In order to prove that the estimation of the parameter ν in the case of cross-polarized antenna degrades the estimate, first the sigma (σ) based on a Rayleigh model is estimated to determine the power in the multipath component and is compared the sigma (σ) estimate based on the Rician model in the case when a strong LoS component was present, In other words the antennas were co-polarized.

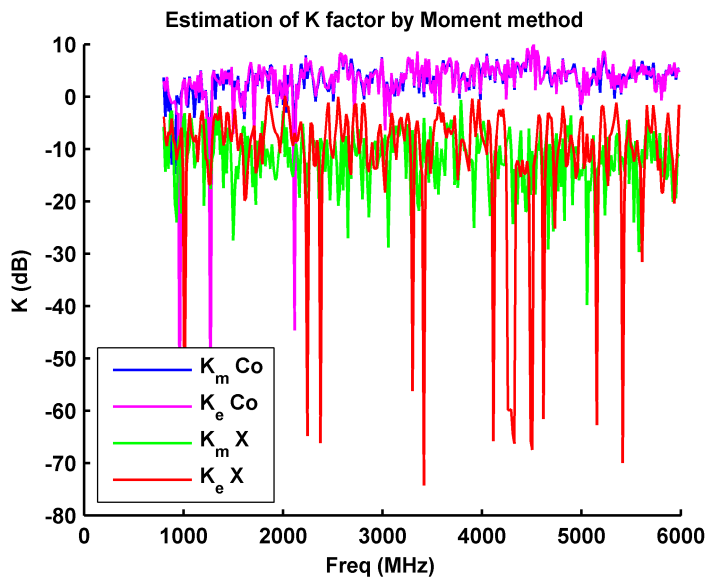


Figure 2.6: Estimated K -factor after 3 point moving averaging ν for cross-polarized antenna configuration

In Figure (2.7), It is evident that in the case of a LoS signal, σ estimated from Rayleigh model is much higher than the σ estimated by the Rician model which shows that defining the correct model for the environment is important otherwise the parameter estimation can be misleading. In case of a LoS component the σ estimate from Rician and conventional method agrees however the σ estimated from Rayleigh model is higher in magnitude as this model could not take into account the LoS component and gives a wrong estimate of the parameter. The log likelihood function would not converge since the Rayleigh model would not for any value of σ within 95% confidence interval, fit the Rician distributed data. Sigma(σ) estimated for no LoS case from Rayleigh model, the conventional method and Rician model

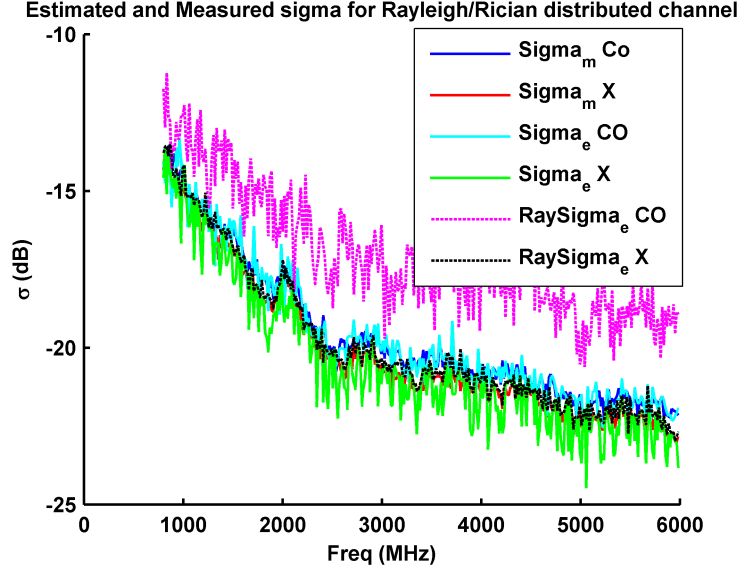


Figure 2.7: Estimated σ for co-polarized and cross-polarized antenna configuration

agrees very well, however Rayleigh and conventional method agrees more closely which is justified since Rayleigh model is precisely designed for such an environment where as the Rician model gives a close result because it is a general model which accounts for the case of no LoS component and converges to a Rayleigh model. It is interesting to note that σ decreases with increasing frequency. The quantity $2\sigma^2$ which is the power in the multipath component will decay with frequency and loading (or Q factor of the chamber). The frequency dependence can be seen with Hills transmission formula derived in [10] and given by (2.23), where V is the volume of the chamber. However there is an additional factor involved here which is loading of the chamber which decays the multipath components in the chamber [5], This behaviour is depicted in Figure (2.8).

$$G_{chamber} = \frac{P_r}{P_t} = \frac{c^3 e_{rad1} e_{rad2}}{16\pi^2 V f^2 \Delta f} \quad (2.23)$$

The estimated LoS component ν is plotted in Figure (2.9) for co and cross polarized antennas and it is evident that ν estimate in case of a LoS component is in good agreement with the standard method at NIST for measuring K-factor from S_{21} or the channel transfer function. The measured average (over frequency) value

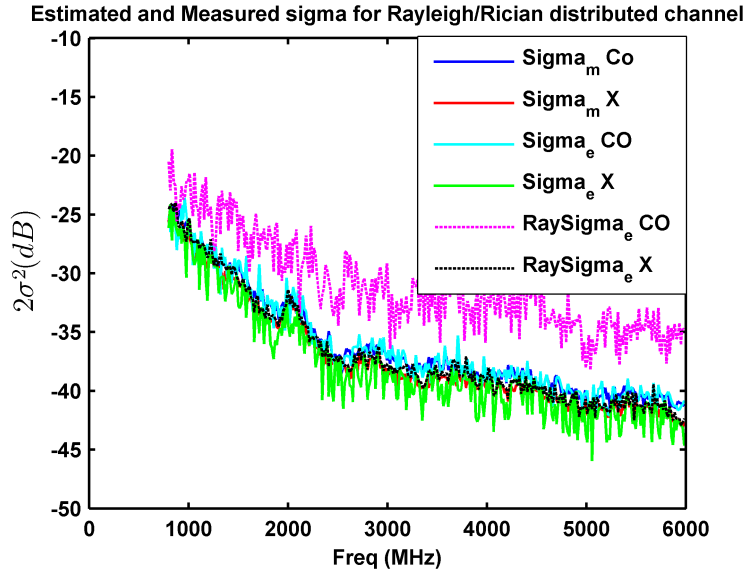


Figure 2.8: Estimated $2\sigma^2$ for co-polarized and cross-polarized antenna configuration

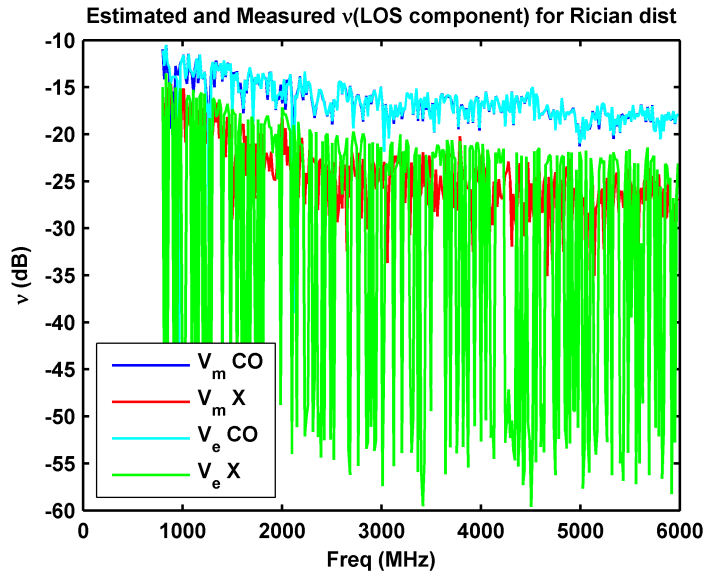


Figure 2.9: Estimated ν for co-polarized and cross-polarized antenna configuration

of $K = 4.1dB$ in case of a LoS component, on the contrary for cross-polarized antennas the average $K = -9.7dB$ which indicates the absence of a LoS component. Figure (2.10) shows that after using a 3 point moving averaging window we can

remove the misleading variation in the graphs which is explained above. It can be seen and justified that ν does not rapidly fall off with frequency instead slightly decays over the frequency range which shows that ν (Mean power or LoS component) is not a function of chamber characteristics (or Q), instead it is a function of directivity, orientation, polarization and physical distance of the receiving antenna relative to transmitting antenna. We can see from Figure (2.9) that ν has a strong dependence on polarization and it also decreases slightly with frequency which is purely justified by (2.24), well known in field of telecommunication and antenna as Friss transmission equation,

$$\frac{P_r}{P_t} = G_t G_r \left(\frac{\lambda}{4\pi R} \right)^2 \quad (2.24)$$

where we can see a decrease in the received power (LoS) purely as a function of frequency, distance and orientation that is incorporated in the gain G_r and G_t of the receiving and transmitting antenna respectively, since LoS component does not interact with the walls of the chamber or the absorbers it is not dependent on the Q and Volume of the chamber, it obeys Friss transmission formula.

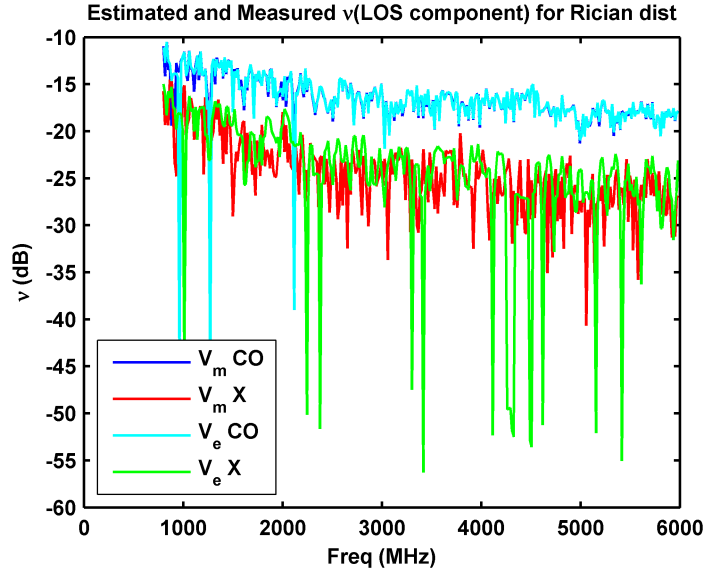


Figure 2.10: Estimated ν after 3 point moving averaging window for cross-polarized antenna configuration

For details on factor effecting ν and σ , [5]. In this thesis the goal is not to study

the factors that can effect ν and σ which would in turn determine the K-factor, however by tuning these factors we can emulate wireless channel with different characteristics depending on the K-factor [11]. The purpose here was to study a robust method for measuring K-factor from the channel amplitude/envelope statistics based on a Rician model. In practice S_{21} parameters are not available and in some applications where non-coherent demodulation is applied, the phase information is absent and only the magnitude of the complex channel or the envelope is received and from which we can determine the distribution of the channel. In such applications maximum likelihood estimation can be used for estimating the K-factor. This method also complements the validity and usability of reverberation chamber as a facility to emulate wireless channel and agrees very well with the standard (S_{21}) method of measuring the K-factor with exception for small values of K.

2.4 Effective number of samples for estimation of K-factor

In order to estimate the K-factor, samples of the channel are collected by rotating the stirrers that emulates dynamic wireless environment in the chamber to replicate a real world wireless channel which changes as a function of time. Here paddles are rotated so the channel can be changed as a function of paddle position, angle or time, either of the domain can be mapped on to other depending upon the subject of study. In this section the number of samples required to get a good estimate of K-factor is studied with respect to paddle position. The mean and standard deviation of the estimate are plotted as a function of paddle position to find out how many samples are needed for these quantities to converge. At each paddle position a sample is collected for a frequency sweep from 0.8 to 6 GHz and K-factor is estimated based on the samples. For paddle position number one, only one sample of the channel is available, in other words one channel realization is available for estimation of K-factor, at second paddle position two channel realizations are available for estimation and so on. Based on these samples or channel realizations across frequency range it is shown in Figure (2.11) and (2.12) that approximately 30 channel realizations are needed for the mean and standard deviation of the estimate of K-factor to converge, respectively. The mean, indicated by μ , is the statistician's jargon for the average value of a signal. It is found by adding all of the samples together, and divide by N. In mathematical form,

$$\mu = \frac{1}{N} \sum_{i=0}^{N-1} x_i \quad (2.25)$$

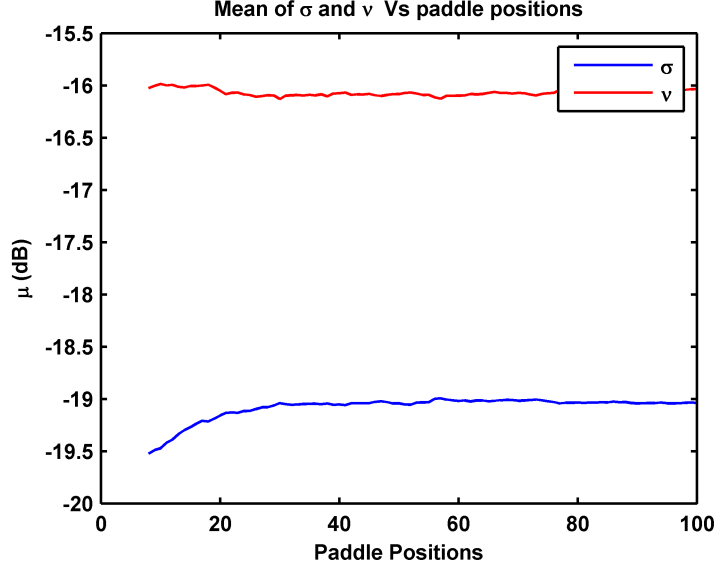


Figure 2.11: Mean of K-factor estimate Vs Number of channel realizations

The standard deviation is similar to the average deviation, except the averaging is done with power instead of amplitude. This is achieved by squaring each of the deviations before taking the average (remember, $power \propto voltage^2$). To finish, the square root is taken to compensate for the initial squaring. In equation form, the standard deviation is calculated as,

$$\sigma = \sqrt{\frac{1}{N} \sum_{i=0}^{N-1} (x_i - \mu)^2} \quad (2.26)$$

Where x_i corresponds to each channel realization. It can be seen in the Figure (2.11) that mean converges to a constant voltage level after 30 samples which is expected as discussed earlier in Section (2.3) that the received signal voltage is in the same order of magnitude and a constant mean was expected. The signal ν and σ are not squared thus the use of term voltage instead of power. The

2.4. EFFECTIVE NUMBER OF SAMPLES FOR ESTIMATION OF K-FACTOR²⁵

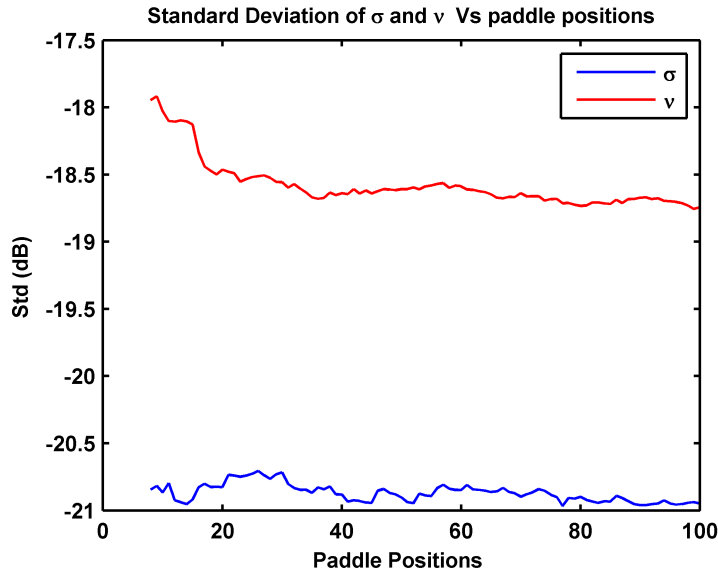


Figure 2.12: Standard deviation of K -factor estimate Vs Number of channel realizations

standard deviation shows the averaging of the power received in the signal. Standard deviation can also be interpreted as the variation of received power around the mean. It converges after approximately 30 samples, in case of the LoS component ν , however the standard deviation of σ (Power in the real or imaginary part of the multipath components, since its not multiplied by 2) keeps fluctuating with every new channel estimation. Because the power received in multipath component is due to constructive and destructive interference therefore with every channel realization we can expect this quantity to vary around the mean as it is clear by plots of mean and standard deviation. These graphs are obtained for the co-polarized antenna configuration and it can be verified from Figure (2.12), since the power in the LoS component is much higher than the power in the multipath components, it should also be clear that the power in multipath component plotted here is indicative of power only either in the real or imaginary part of the multipath components. The total power is obtained by multiplying the quantity σ^2 by 2. These graphs are plotted after 8 channel realizations since the estimate for number of samples below 8 was very poor and it scaled the graph such that these variations were not prominent.

2.5 Uncertainty in estimation of K-factor

Uncertainty analysis are important consideration in measurement sciences today. Measurements can be quiet useless without the knowledge of their associated errors or uncertainty in general terms. In general, measurement has imperfection which lead to error in the measured quantity, these errors are traditionally classified as systematic and random errors. Systematic errors can be compensated for but are not totally eliminated. In practice usually a calibration or a correction is introduced to compensate for the systematic errors and make them as small as possible, however it is only possible if we know all the sources that are contributing to the systematic errors and compensate for them. It is assumed that, after correction, the expectation or expected value of the error arising from a systematic effect is zero. Random errors arises from unpredictable or stochastic sources and can usually be reduced by increasing the number of observations since it is impossible to compensate for such errors. It is important to point out here that the experimental standard deviation of arithmetic mean is not a random error of the mean instead is the uncertainty of the mean due to random effects. A similar approach is used to estimate the uncertainty in the estimated true value of the parameters of the Rician distribution (ν, σ) and K-factor. The uncertainty in the estimation of K-factor can have contributions from both the random errors and the measurement error. To eliminate the effect of systematic errors we use simulated data that is Rician distributed amplitude of a complex Gaussian process. In this data the only errors associated are random and possibly can have contribution from sources, including:

- How good the defined model is to represent the data
- If each observations are independent or not
- Random effects associated with random number generator.

If we assume that the complex Gaussian distributions obtained from the MATLAB random number generator algorithm are totally independent than the only error in the estimate would be introduced by how well the maximum likelihood estimation fits the data to the defined Rician model and we would expect to see a different result for every channel realization because of the randomness introduced by the random number generator. This is one way to estimate the uncertainty introduced by the maximum likelihood estimation method in the estimation of K-factor. In this work the focus is on how well this method works for estimation

of channel parameters when phase information is missing and we only have the amplitude distribution of the channel. In most cases the best available estimate of the expected value of a certain quantity that varies randomly and for which n independent observations have been obtained is the arithmetic mean. Thus if for each channel realization the number of observations are large and independent it is reasonable to assume that the estimated parameters from each observation (Rician distributed data set) will combine to have a normal distribution. The mean of the distribution of estimated parameters will give the best estimate of the true value of the parameter and the standard deviation of this distribution will give the standard error in the estimation of the parameter. In maximum likelihood estimation the second derivative of the log likelihood function produces a Hessian matrix, in multi parameter models. The negative expectation of this matrix results in the ‘‘information matrix’’ inverting which gives the variance-covariance matrix. The standard errors in the estimated parameters can be obtained by taking the square root of the diagonal elements of the variance-covariance matrix. In our case, since we have two parameters to estimate, this gives a (2×2) variance-covariance matrix. Many commercial software packages offer to calculate the variance-covariance matrix. In MATLAB it is done by using the ‘MLECOV’ function. This gives the standard error or standard deviation of the sample distribution of the estimated parameters of Rice distribution $R(\nu, \sigma)$. The K-factor is defined as $K = \frac{\nu^2}{2\sigma^2}$, to find the uncertainties in the K-factor we need a way to propagate the uncertainties in the parameters. The uncertainty in K-factor is estimated by using simple error propagation formula given below.

$$\text{If } K = f(\nu, \sigma) = \frac{\nu^2}{2\sigma^2}$$

then,

$$\delta_K = \sqrt{\left(\frac{\partial f}{\partial \nu}\right)^2 \text{var}(\nu) + \left(\frac{\partial f}{\partial \sigma}\right)^2 \text{var}(\sigma) + 2\left(\frac{\partial f}{\partial \nu}\right)\left(\frac{\partial f}{\partial \sigma}\right) \text{cov}(\nu, \sigma)} \quad (2.27)$$

Where δ_K is the uncertainty associated with the K-Factor. After taking the partial derivative of $f(\nu, \sigma)$ with respect to ν and σ , We get the form of equation as

$$\delta_K = \sqrt{\left(\frac{\nu}{\sigma^2}\right)^2 \text{var}(\nu) + \left(\frac{\nu^2}{\sigma^3}\right)^2 \text{var}(\sigma) - 2\left(\frac{\nu}{\sigma^2}\right)\left(\frac{\nu^2}{\sigma^3}\right) \text{cov}(\nu, \sigma)} \quad (2.28)$$

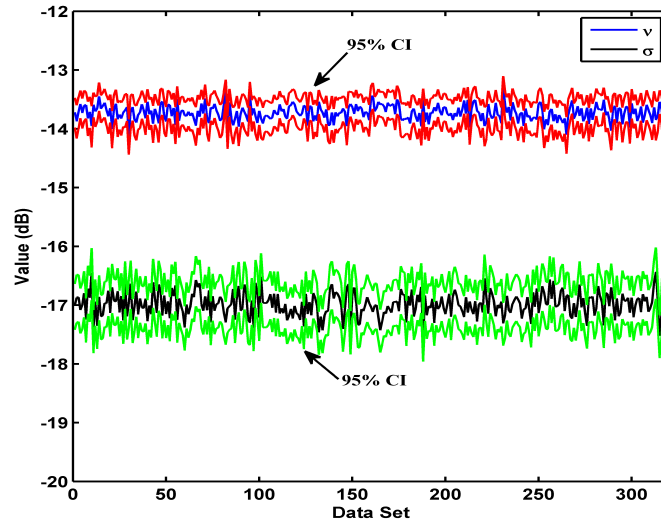


Figure 2.13: Estimated parameters by MLE with 95% confidence intervals, using simulated data with $K=3.5$ dB ($\nu = -13.7$ dB, $\sigma = -16.9$ dB)

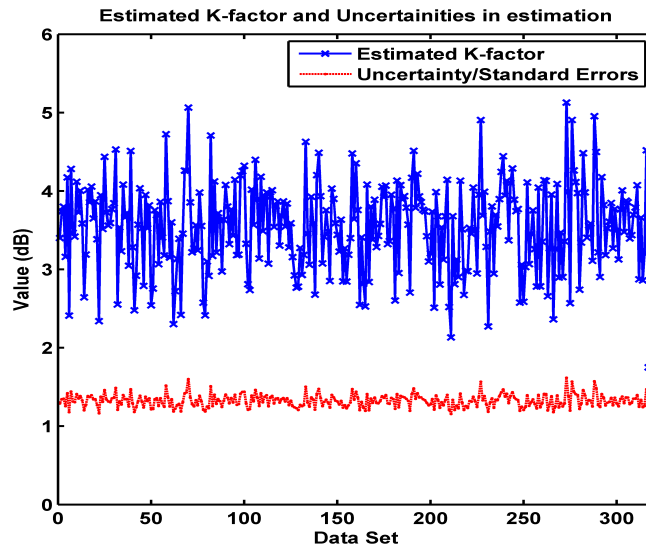


Figure 2.14: Standard error in K factor estimation

Simulated data is used by choosing parameters ν and σ for the complex Gaussian distribution such that we have a $K = 3.5$ dB. With simulated data we are sure

that all the uncertainties associated in estimating K-factor are parametric (random errors) rather than measurement uncertainties that would come into play if we used measured data to estimate the K-Factor. Figure (2.13) shows the estimated parameter value for each data set and the 95% confidence interval assuming that the sample distribution of each parameter is normal. Figure (2.14) shows the estimated K-factor for the simulated data as we can see that the K-factor varies around its true value i.e 3.5 dB in this case, therefore, for the estimate to be more meaningful the uncertainties in the estimation should also be reported which can be seen in the same figure. The standard deviation of the K-factor is 0.29 which can be translated to a corresponding decibel value according to [12].

$$\sigma_{dB} = 5 \log_{10} \left\{ \frac{1 + \sigma}{1 - \sigma} \right\} \quad (2.29)$$

In logarithmic scale the uncertainty or standard deviation is 1.32 dB calculated by (2.29). This has been verified by Monte-Carlo simulations. By propagating the parametric uncertainty in K-factor we have the uncertainty of 0.29 (1.32 dB) associated with the K-factor as shown in Figure (2.14). These results are very close and thus verifies that the propagation of uncertainty works fine for our model however in real life many processes cannot be modeled or are hard to model, therefore, techniques like Monte-Carlo are not an option, in such a case and we can rely on propagation of uncertainty since we have the data from measurements.

2.6 Conclusion

In this chapter we discussed how to emulate a wireless channel in a reverberation chamber. Rician K-factor plays an important role in wireless communication and determines if the channel has Rayleigh or Rician distributed amplitude statistics. This indicates whether or not channel has a dominant LoS component. It is important to know any contribution from the LoS component, as it effects the bit-error-rate of the received signal, which is studied in the following chapter. We studied a method based on complex channel data which gives a direct measurement for the K-factor from the scattering parameter S_{21} . In propagation measurements, where we usually do not have access to the phase information of the channel and only amplitude statistics are known, there is a need to determine the K-factor in the channel by alternative methods. Maximum Likelihood Estimation is one potential

approach that estimates the K-factor based on amplitude statistics. We have studied this method and addressed the uncertainties in its estimation. The MLE method works well for the case when there is a strong LoS component but in the absence of a LoS component the estimation is poor. Since the defined model is Rician it does not estimate very well for a no LoS scenario, therefore, we need to select the right model when doing parametric estimation. Parameter estimation in a no-LoS scenario when Rician model is used can also be improved if we have more samples of the channel which is usually not suitable for real time processing.

3

Characterization of a Wireless Channel in RC

3.1 Time-Varying Channel Impulse Response

Multipath structure is important in determining the small-scale fading effect, therefore a number of wideband channel sounding techniques have been developed [7]. These techniques may be classified as:

- *Direct pulse measurement*
- *Spread Spectrum sliding correlator measurement*
- *Swept frequency measurement*

In this work the swept frequency measurement technique is chosen because it provides amplitude and phase information in both time and frequency domain and the availability of VNA and digital computer for processing render this technique for measuring channel impulse response suitable and less painful, impedance mismatch correction is straight forward and VNA also offers higher dynamic range.

3.2 Frequency Domain Technique for Channel Sounding

The dual relationship between time domain and frequency domain allows one to measure the channel impulse response using the frequency domain methods. The vector network analyzer controls a synthesized frequency sweeper. The sweeper scans a particular frequency band by stepping through discrete frequencies. The spacing and number of these frequency steps impacts the time resolution of the calculated impulse response. At each frequency step, the S-parameter test set transmits a reference signal level at port 1 and monitors the signal level at port 2. These signal levels allow the analyzer to determine the complex response of the channel (i.e. $S_{21}(\omega)$) over the measured frequency range. The complex response of the channel is a frequency domain representation of the channel impulse response. This channel response is then converted to the time domain using inverse discrete Fourier transform (IDFT) processing, giving a band-limited version of the impulse response. This method provides amplitude and phase information in the time domain. However the system requires careful calibration and synchronization between the transmitter and receiver, making it useful for close measurements, at NIST close measurement requires that the T_x and R_x must be separated by less than 200 m, like indoor channel measurements. The drawback of this technique is that we cannot measure a time-varying channel impulse response as the frequency response for such a channel can change rapidly giving an erroneous impulse response measurement. This can be overcome by using fast sweep times to keep the total frequency response measurement interval as short as possible. A faster sweep time can be accomplished by reducing the number of frequency steps but this sacrifices time resolution and excess delay range in the time domain. However this setup is very efficient and successful for indoor propagation measurements and for a facility like a reverberation chamber where indoor channels are emulated, this setup is decent choice. A typical setup is shown in Figure (3.1).

3.3 Impulse response of a Rayleigh Fading Channel

In order to characterize the wireless channel in a reverberation chamber, we first begin with the time-varying channel impulse response. The measurement configuration described in Section 2.1 is used such that both the transmitting and receiving antennas are placed facing towards the stirrers. By this arrangement it is ensured

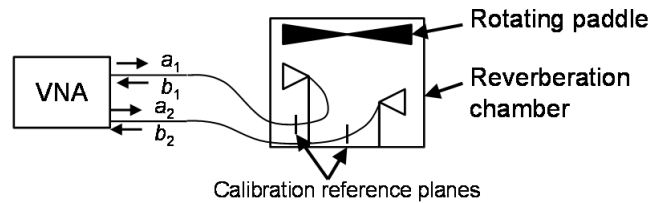


Figure 3.1: Graphical illustration of Measurement Setup at NIST.

that there is a negligible contribution from the unstirred energy in the chamber and thus the channel envelope is Rayleigh distributed as explained above. We make the channel time-varying by rotating the stirrers in discrete steps or continuously, depending upon the application such that the receiver antenna experiences a changing environment as the modes are stirred in the chamber by the stirrers. A vector network analyzer is used to measure the frequency response of the chamber at 100 different stirrer positions such that the stirrers are rotated through one complete revolution with a step of 3.6° . Frequency stepping is chosen so that the sampling rate of the channel is high enough to avoid aliasing as studied later in this section. Each measurement can be thought of as an impulse response of a time varying channel at a particular point in time. The frequency is swept over a bandwidth of 5.2 GHz from 0.8-6 GHz. The frequency response of the channel is sampled every 325 kHz which gives 16001 frequency points. This frequency band covers most of the communication band today in use for the operation of commercial devices. In the frequency domain we sweep over a wide range of frequencies, such that its a wideband signal centered at the carrier frequency of approximately 3.5 GHz. It is well established from the Fourier theory that a wide band signal corresponds to a very short pulse width in the time domain which is supported by the known result that an infinite bandwidth signal like white noise would give a delta function or im-

pulse in the time domain and vice versa. It is therefore equivalent to transmitting an impulse $\delta(t)$ through the channel which would give a channel impulse response $h(t)$. Mathematically we model the impulse response as:

$$h(t) = \sum_{i=0}^{M-1} a_i \delta(t - \tau_i) e^{-j(\theta_i + \Delta\theta_i)} \quad (3.1)$$

where M is the total number of multipath components, the delays τ_i , the gains or losses a_i , phases θ_n and phase displacement $\Delta\theta_i$. The phase displacement results from the motion of the receiver or other spatial changes of the receiver location relative to the rest of the propagation environment which may itself include moving objects. In our case we get the complex channel response which corresponds to the S_{21} parameters collected from the vector network analyzer. When an inverse DFT is applied to such a wideband signal we get the impulse response of the channel at different time delays (τ), where the maximum delay τ_{max} is determined by the spacing of the samples in the frequency domain, which in our case is $\delta F = 325 \text{ KHz}$. The Fourier relationship is given by $\tau_{max} = \frac{1}{\delta F}$. It is worth mentioning here that we should consider a wideband signal in order to estimate an impulse response of the channel. A narrowband signal instead of approximating an impulse in the time domain would rather give a sinc pulse with a certain null-null width given as ($T_{bb} = \frac{2}{B}$), where B is the bandwidth of the pulse, therefore, wider the bandwidth the more sinc pulse would approximate a delta function ($\delta(t)$). When the signal is narrowband we do not get fine resolution of the channel response in the time domain and it would look more like envelope of the over all channel response. This is illustrated in Figure (3.2) which shows the averaged power delay profile (*i.e.* impulse response squared ($|h(\tau)|^2$), here averaging is done over 100 stirrer positions or channel realization so it gives an average power delay profile of the chamber. As it can be seen that when we have a relatively narrowband signal it does not give a fine resolution of the channel response however increasing the bandwidth gives us more information of how channel is behaving since now the sinc pulse is approaching a delta function. This can also be thought of a pulse train sampling the channel, if the pulses are delta function then we can sample very fine otherwise wider pulses would give more of an envelope approximation of the channel impulse response. This discussion motivates why we use a wideband frequency measurement to estimate the channel impulse response.

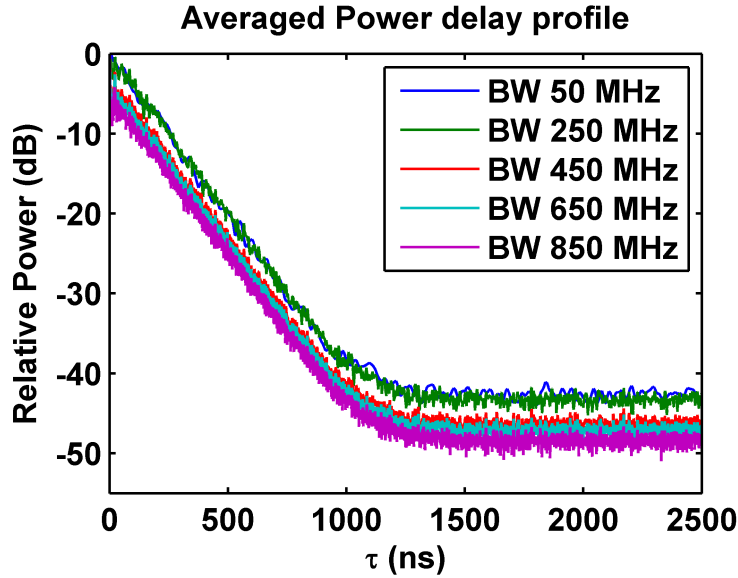


Figure 3.2: Effect of signal BW on the estimation of channel impulse response

From the frequency sampling theory ¹ we can conclude that the channel impulse response $|h(\tau)|$ or the Power delay profile $|h(\tau)|^2$ should decay down to zero or the noise floor of the instrument after certain delay time τ . If the PDP does not reach a noise floor we can conclude that we are aliasing. In the RC we can control the decay rate of the PDP by loading the chamber. By ‘loading’ it is meant that a block of RF absorber is added to the reverberation chamber which absorbs the RF power, this reduces the ringing time of the energy in the chamber causing power to decay more rapidly. Loading is used interchangeably for adding absorbers to the chamber. Loading 0 means no absorbers are added, loading 1 means one absorber block is added to the chamber and so on, however loading affects the uniformity of the averaged fields in the chamber, therefore, care must be taken while loading such that the statistical uniformity is preserved [13]. The channel impulse response for the reverberation chamber is plotted in Figure (3.3) for loading 0, 1, 3 and 5.

In Figure (3.3) it is obvious that the power in the chamber decays exponentially. The power delay profile is plotted for the case when the chamber is unloaded and loaded with one, three and five absorbers. Each PDP is then fitted to an exponential function. It is well known from the statistical theory that the mean and standard

¹see Appendices

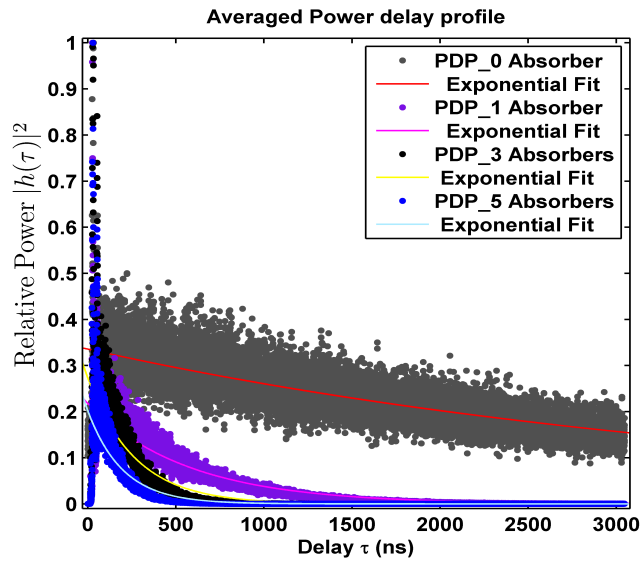


Figure 3.3: Power delay profile in linear scale averaged over 100 stirrer position for a bandwidth of 5.2 GHz.

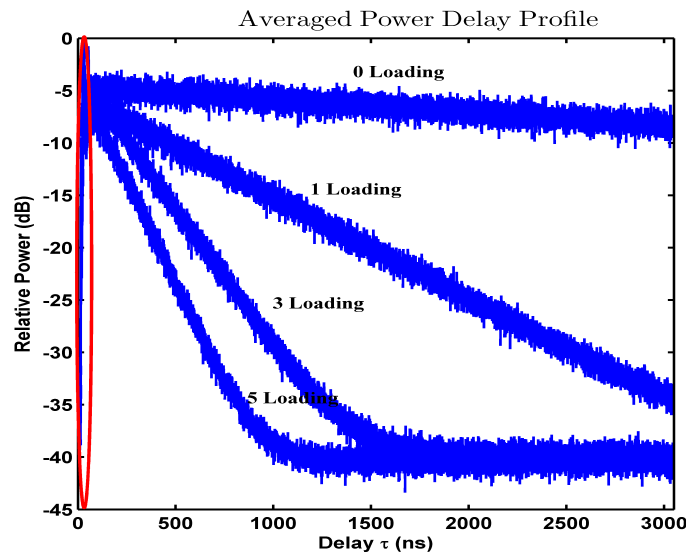


Figure 3.4: Power delay profile in logarithmic scale

deviation of the exponential distribution are the same [14] and [7]. Important quantities which characterize the power delay profile are the mean and root mean square

(RMS) delay spread. As we know that $\mu_{T_m} \approx \sigma_{T_m}$ in many channels with large number of scatterers, the exact relationship between them depends on the shape of autocorrelation function $A_c(\tau)$, where T_m is the transmitted symbol duration². In a reverberation chamber the PDP is exponential, therefore, we would expect these quantities to be approximately the same. It can be easily shown that for an exponential function of the form $P(t) = P_0 e^{-\frac{t}{\tau}}$ where $P(t) = 0$ for $t < 0$, the decay constant turns out to be equal to the mean delay.

3.3.1 Power Delay Profile

To calculate the RMS and mean delay from the measured power delay profile we need to set a certain threshold to discard noise samples of the PDP [11], where the study shows that the values of RMS delay spread converge as the threshold approaches the noise floor, so a reasonable choice of the threshold is 3 dB above the noise floor. Table 3.1 shows values of mean delay, RMS delay and decay constant of an exponential function fitted to the PDP shown in Figure (3.3). The values are not close so the PDP is plotted in the log scale in Figure (3.4) to see the decay on a magnified scale, it clearly shows that for the case of zero and one absorber we are not sampling at a high enough rate in the frequency domain such that the condition $\tau_{max} > 2\tau$ discussed in Appendix (B.1) is not satisfied and we are aliasing. The PDP does not decay down to the noise floor which in this case is approximately -40 dB below the normalized maximum. This can also be interpreted as the power in the multipath components have not died down to the noise level. In the case of loading three and five the PDP decays down to the noise floor as can be seen in the figure. It is also noted that the PDP is not a pure exponential because of the early rise time or charging time of the chamber as can be seen in the early part of the PDP marked in red. Thus the PDP consist of two contributions, the charging time and the exponential decay after the chamber has reached its reverberant condition [15]. To get the actual decay time of the power we must discard the early samples of the charging time in order to get only the pure exponential PDP of the chamber. In case of loading zero and one a much higher frequency sampling rate is needed such that there is no aliasing. To show the effect of rise time on the estimation of delay parameters we plot and calculate the delay parameter by discarding the rise time samples to get only the exponential decay of power in the

²See Appendix A

chamber. Figure (3.5) and Figure (3.6) shows the PDP in linear and logarithmic scale respectively, where the charging time samples are discarded and Table 3.2 shows the values of calculated delay parameters. In the case of 3 and 5 absorbers the values of μ_{T_m} , σ_{T_m} and $Slope_{T_m}$ are very close to each other whereas in the case of 0 and 1 absorber these parameter still do not agree closely and that is due to aliasing. In order to verify that we perform another experiment where frequency sampling rate is much higher.

Table 3.1: Mean Delay, RMS Delay and Delay Constant from Slope

	$\mu_{T_m}(ns)$	$\sigma_{T_m}(ns)$	$Slope_{T_m}(ns)$
0 Absorber	719.2	432.2	3900.2
1 Absorber	426.87	337.69	571.7
3 Absorber	197.0	163.02	265.3
5 Absorber	139.18	109.11	197.1

Table 3.2: Mean Delay, RMS Delay and Delay Constant from Slope after discarding the charging time samples

Loading	$\mu_{T_m}(ns)$	$\sigma_{T_m}(ns)$	$Slope_{T_m}(ns)$
0	695.1	426.6	3692.8
1	396.8	336.7	469.4
3	169.2	164.3	178.03
5	115.05	114.68	120.3

From Figure (3.2) it can be concluded that a wideband pulse of 1 GHz approximates a delta function such that we have a reasonable impulse response estimate of the channel. The VNA can only collect 20001 samples, therefore, to sample at a higher rate we need to take samples in a narrower bandwidth. In this study we are interested in the frequency band around 2 GHz. A bandwidth of 1 GHz centered at 2 GHz is selected and 20001 frequency samples are collected which gives $\delta F = 50KHz$ that implies a much larger τ_{max} compared to the τ_{max} from $\delta F = 350KHz$ in the previous experiment. If $\tau_{max} > 2\tau$ there will be no aliasing

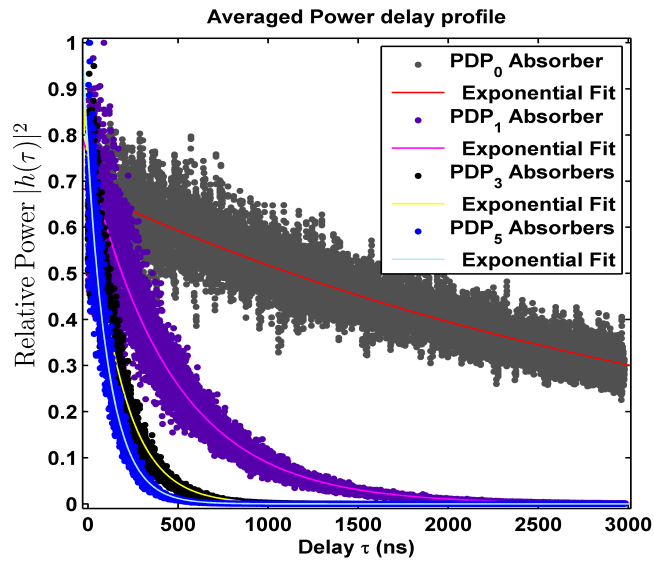


Figure 3.5: Power delay profile in linear scale after discarding the charging time samples

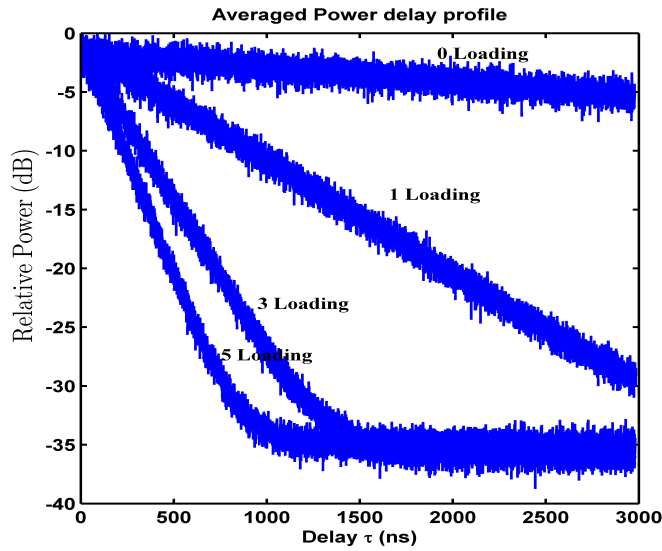


Figure 3.6: Power delay profile in logarithmic scale after discarding the charging time samples

and the PDP will decay down to the noise floor. As discussed above, for the case of 0 and 1 absorber we need a much higher sampling rate than $\delta F = 50KHz$ to avoid

aliasing. In order to find the appropriate sampling rate, the coherence bandwidth was measured by doing an autocorrelation of the frequency samples over a bandwidth of 1 GHz. It was seen from the autocorrelation curve that in the case of no absorbers the coherence bandwidth at $R_f(\Delta F) = 0.5$ was 0.28 MHz, this shows that at $\delta F = 50\text{KHz}$ we will have only 5 samples above $R_f(\Delta F) = 0.5$. Another way of interpreting this is that only 5 samples of the autocorrelation function are sampled at this frequency sampling rate which is not high enough. It is desired to have at least 20 samples to calculate coherence bandwidth from an autocorrelation curve. This is discussed in Section (3.5.1) in detail. Since we are limited by the sampling rate of VNA and also interested in the bandwidth of 1 GHz, so there is no compromise between the two in our existing measurement setup, therefore, an alternative way to solve this problem was to sample the bandwidth in chunks such that the sampling rate inside the small chunk is high enough to give a reasonable number of samples for calculating the coherence bandwidth from the autocorrelation curve which also means we are sampling the autocorrelation function at a much higher sampling rate. If the sampling rate is above Nyquist criterion it would give $\tau_{max} > 2\tau$ in the time domain such that there would be no aliasing. This approach is used to determine the frequency sampling rate to avoid aliasing in both the time and frequency domain.

Table 3.3: Mean Delay, RMS Delay and Delay Constant from Slope with no aliasing and charging time samples

Loading	$\mu_{T_m}(ns)$	$\sigma_{T_m}(ns)$	$Slope_{T_m}(ns)$
0	1668.5	1664.1	1659.5
1	493.7	510.2	481.9
3	222.7	219.2	221.04
5	101.8	100.6	103.00

Chunks of 5 MHz bandwidth are acquired using the multiple measurement option of the VNA such that 1501 frequency samples were taken in each chunk. This gives total of 21 chunks of 5 MHz bandwidth which are each 50 MHz apart in the total bandwidth of 1.5-2.5 GHz. Figure (3.7) shows the power delay profile for 0 and 1 absorber case and it decays almost to the noise floor, which tells us that now we are sampling above Nyquist rate. If we are above Nyquist rate for

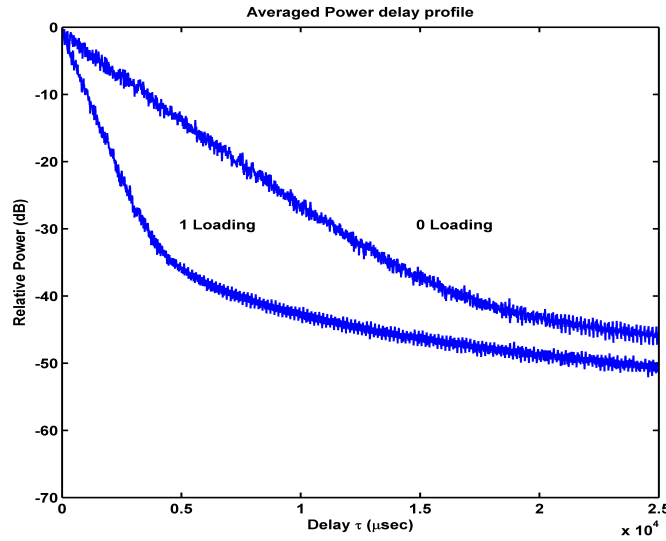


Figure 3.7: Power delay profile in logarithmic scale for 0 and 1 Absorber case with no Aliasing

0 absorber case then we are also above Nyquist rate for 1 absorber case as the coherence bandwidth increases with loading [16]. Figure (3.8) shows power delay profile for all absorber cases when there is no aliasing and Table 3.3 shows that the calculated values of the delay parameters agrees closely as we expected. These power delay profiles are calculated by using a wideband frequency data and the chamber is expected to show the frequency dependent behavior due to the wall losses or the surface resistance, which is given by (3.2).

$$R_s = \sqrt{\frac{\omega\rho}{2\varsigma}} \quad (3.2)$$

where ς and ρ are the conductivity and permeability of the conductor. Ideally as the frequency increases the surface resistance go higher thus reducing the Quality Factor³(Q) of the chamber neglecting all other loss mechanism in the reverberation chamber.

From the frequency dependent behavior of the chamber it is natural to assume that the RMS delay spread could also be dependent on the frequency range of the

³See Appendices

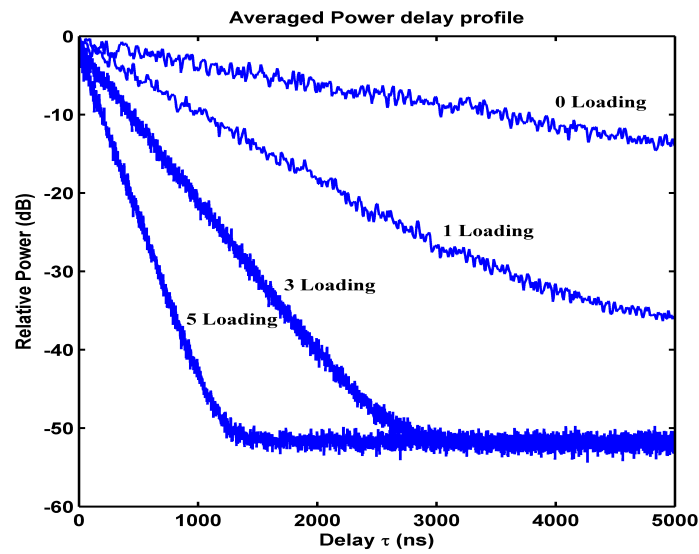


Figure 3.8: Power delay profile in logarithmic scale for all loading cases with no Aliasing

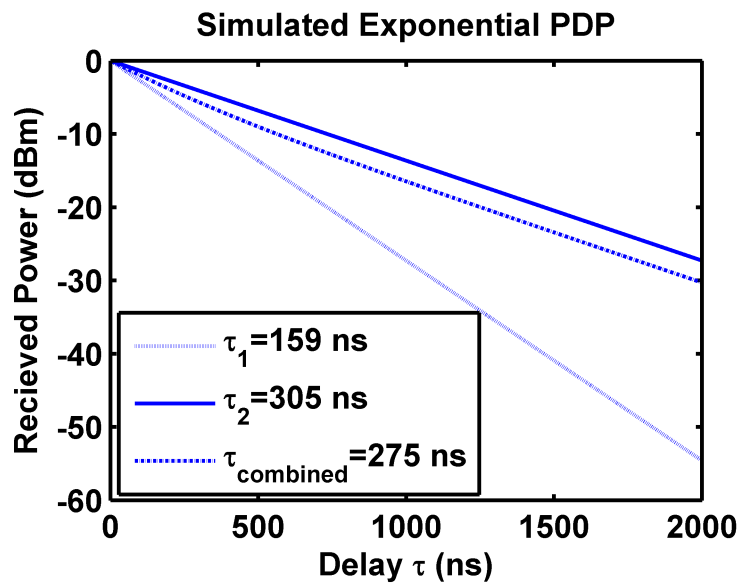


Figure 3.9: Simulated Power Delay Profiles to show that the combination of the two power delay profiles is dominated by the one with greater value of τ

data used to obtain the time domain representation using an IDFT. This frequency dependence of τ is studied in [11], where it is shown that the RMS delay spread

Table 3.4: Mean Delay, RMS Delay spread for theoretical exponential function with decay constant $\tau = \frac{Q}{\omega}$

	$\mu_{T_m} (ns)$	$\sigma_{T_m} (ns)$	$\tau = \frac{Q}{\omega} (ns)$
PDP1	158.6	159.0	159.1
PDP2	313.9	305.9	318.3
Combined	261.9	275.7	

is dependent on frequency and when we use a very wide range of frequencies (e.g, 0.8-6 GHz), the result could be misleading since the combination of two power delay profiles with the exponential behavior but different delay spread would result in a PDP in which the greater τ would dominate. This is demonstrated in Figure (3.9) which is the sum of two power delay profiles with different delays τ_1 and τ_2 , normalized to its maximum shows that after certain delay time the PDP with smaller decay constant or greater τ will start to dominate the decay constant of the combined PDP. Table 3.4 shows the values of mean, RMS delay spread calculated for a particular delay spread $\tau = \frac{Q}{\omega}$. From this it is concluded that the RMS delay spread should be calculated over the frequency band of interest otherwise it could result in misleading values. In practice many wireless communication systems are narrowband therefore we should calculate PDP for a frequency band over which the communication system operates. This gives a more accurate representative value of RMS delay spread to study the wireless system and is indeed the true delay spread of the power in the chamber. We can then relate this RMS delay spread to the symbol duration while studying the affect of channel on a particular data rate or symbol duration, this is discussed in Chapter 4. To be more careful with the delay spread calculation, a bandwidth of 100,200 and 300 MHz around the carrier frequency of 2 GHz is selected for processing, these values are given in Table 3.5 which represent more accurately the delay spread that will be experienced by a modulated signal introduce in the chamber. It should be noted that the values of delay parameter are almost the same as those calculated over 1 GHz bandwidth in Table 3.3, this is because we are already operating in a relatively narrower bandwidth as compared to delay spreads measured over 200 MHz bandwidth every 5 GHz from 1-12 GHz, as was studied in [11]. The delay spread is frequency dependent as long as the losses in the chamber are due to wall and/or antenna but

when the absorber losses are added then this dependence goes away as the losses due to absorbers start to dominate it can be see from (3.3) [17].

$$\tau_{RMS} = \frac{1}{C_1\sqrt{f} + C_2N\sigma_{absorber} + \frac{C_3}{f^2}} \quad (3.3)$$

Table 3.5: RMS Delay Spread for different bandwidths centred at 2 GHz

Loading	Bandwidth (MHz)	σ_{T_m} (ns)
0	100	1620.0
	200	1617.8
	300	1619.6
1	100	507.1
	200	502.3
	300	501.9
3	100	221.6
	200	218.7
	300	218.4
5	100	101.6
	200	101.2
	300	100.7

3.4 Impulse response of a Rician Fading Channel

In the section above we have studied the RMS delay spread in the chamber for Rayleigh channel. We are also interested in emulating Rician channels for different values of K. In this section we study how RMS delay spread is affected when there is a LoS component present in the channel. For small values of K the RMS delay spread is not affected too much however when there is a strong LoS component the RMS delay spread changes quiet a bit. The power in the early arriving multipath components at the receiver influences the LoS (unstirred) symbol (typically assumed to be the first arriving symbol) where as all later arriving multipath components which were influential when there was no strong LoS component are not

significant any more since the power in LoS component is relatively much higher than the power in the late arriving multipath components. The strong LoS component can be seen in Figure (3.10), It should be noticed that the noise floor is -30 dB down compared to the case when there is no LoS component in Figure (3.8). This is just the scaling in the power since the PDP is normalized to the LoS component and it shows relative power, in reality the noise floor is the same. We can conclude that when calculating the RMS delay spreads for Rician channel the only effective contribution would be from the early arriving multipath components. Table (3.6) shows the values of mean delay and RMS delay spread for different loading cases for a K-factor of 5 dB. As anticipated the mean delay and RMS delay spread have decreased but they are not the same any more since the power delay profile is not a pure exponential function because of the LoS component. To emulate a fading channel with certain delay spread in a reverberation chamber we also need to consider the K-factor in addition to loading. We have two degrees of freedom for tuning the RMS delay spread in the channel, the loading and the K-factor. Evgeni showed that RMS delay spread is also a function of K-factor which can be seen from (3.4), [11].

$$\tau_{RMS} = \frac{Q}{w} \sqrt{\frac{2\alpha \ln(\alpha) - \ln^2(\alpha)\alpha - 2\alpha + 2}{(1-\alpha) + K} - \frac{(\alpha \ln(\alpha) + 1 - \alpha)^2}{((1-\alpha) + K)^2}} \quad (3.4)$$

Where α is the threshold in dB for truncating the noise samples from the PDP, as discussed earlier.

Table 3.6: RMS Delay spreads for PDP in the presence of LoS component with K=5 dB

Loading	$\mu_{T_m} (ns)$	$\sigma_{T_m} (ns)$
5	38.5	78.5
3	103.4	175.3
1	354.8	471.8
0	1663.9	1819.9

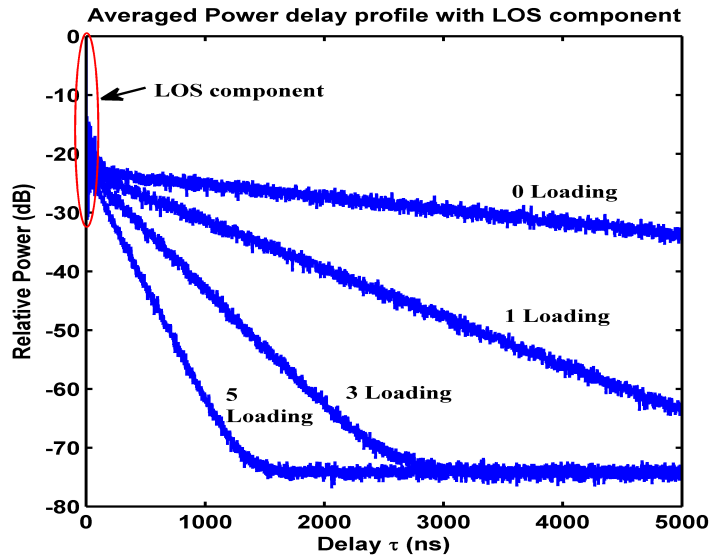


Figure 3.10: Power delay profile in logarithmic scale for all loading cases with average $K=5$ dB

3.5 Coherence Bandwidth

Coherence bandwidth is defined as the frequency range over which the channel is correlated as discussed in Appendix A.4.2. It is a key parameter to determine if the channel is frequency selective or frequency flat for transmission at a particular data rate. It is the frequency domain view of determining if the symbol duration is much lesser than the delay spread which would give frequency selectivity also known as wideband fading. Otherwise the signal would experience flat or narrowband fading.

When a reverberation chamber is excited at a single frequency, modes resonant at neighboring frequencies will also be excited due to the finite Q-factor. The Q of a resonance is given by $f/\Delta f$, where f is the resonance frequency and Δf is the half-power (3-dB) bandwidth. Thus, the mode bandwidth is defined as the frequency range over which the power in an adjacent excited mode is larger than half the power in the mode when it is excited at its resonance frequency. The modes are distributed over frequency, therefore, it is convenient to use an average mode bandwidth Δf to determine the approximate number of excited modes by counting modes within Δf around the frequency of operation. In [16] it is shown that the average mode bandwidth and the coherence bandwidth are the same in the rever-

beration chamber, which may be an intuitive but was experimentally shown for the first time in this letter. In this thesis work we calculate the coherence bandwidth of the chamber for different loading cases.

In the reverberation chamber the time varying frequency response of the channel is a function of frequency and stirrer position $H(f, n)$, this is the same as S_{21} measured between the two ports of the antenna, assuming perfect impedance matching. The frequency data is collected by a VNA at different stirrer positions. Each stirrer position gives a new channel realization, as discussed earlier. The coherence bandwidth can be calculated by doing a complex or amplitude autocorrelation over the frequency range. The complex $R_f(\Delta f)$ and envelope $\rho_f(\Delta f)$ auto correlation functions (ACFs) of the frequency response of the channel and the theoretical relationship between them are derived in [18] and are given as,

$$R_f(\Delta f) = \frac{\mathbf{E}[H^*(f, n).H(f + \Delta f, n)]}{\mathbf{E}[|H(f, n)|^2]} \quad (3.5)$$

$$\rho_f(\Delta f) = \frac{\mathbf{E}[A(f, n).A(f + \Delta f, n)]}{\mathbf{E}[A(f, n)^2]} \quad (3.6)$$

$$A(f, n) = |H(f, n)| - \mathbf{E}[|H(f, n)|] \quad (3.7)$$

$$\rho_f(\Delta f) \approx |R_f(\Delta f)|^2 \quad (3.8)$$

In this study the complex frequency correlation function is evaluated. The expectations $\mathbf{E}[\cdot]$ here is taken over the stirrer positions 'n' each one corresponding to an independent channel realization. The coherence bandwidth here is defined as the frequency range for which the normalized frequency correlation function $R_f(\Delta f)$ is above 0.5. This is the most commonly used and relaxed definition in the communication world [7], however other definitions also exists.

3.5.1 Measurements in reverberation chamber

In order to calculate the coherence bandwidth, we use the same frequency data that has been used for calculating the RMS delay spread above. For the case of 3 and 5 absorbers the correlation was calculated over the data where we had 20001 frequency samples in a bandwidth of 1 GHz (1.5 GHz - 2.5 GHz). This gives $\Delta F = 50kHz$, that is, a frequency sample every 50 kHz apart. Figure (3.11) shows the frequency autocorrelation function which gives the coherence bandwidth for 5 and 3 loading cases at $R_f(\Delta f) = 0.5$.

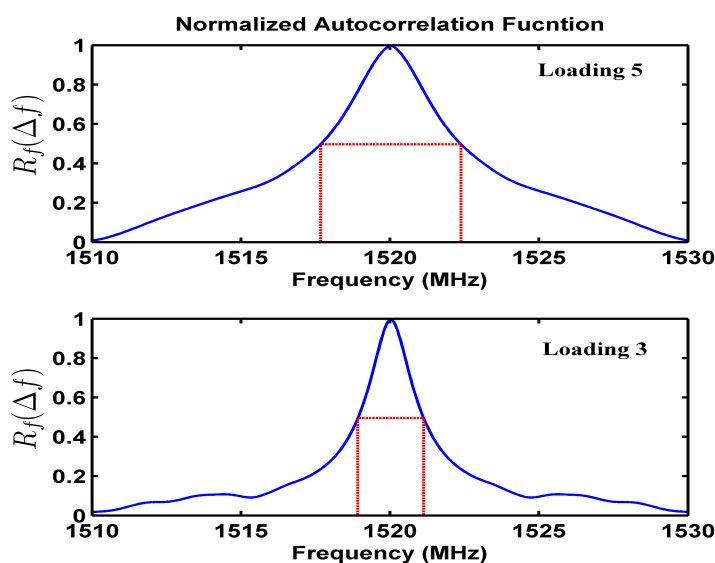


Figure 3.11: Coherence BW for loading 5 and 3 over 20 MHz BW at center frequency of 1520 MHz

The autocorrelation function shows a smooth curve and coherence bandwidth is calculated by stepping every 10 MHz over the whole bandwidth. These coherence bandwidths gives 82 and 42 samples above $R_f(\Delta f) = 0.5$ for 5 and 3 loading cases respectively, which are enough for estimating an autocorrelation function. The auto correlation function falls almost to zero which shows we have enough samples to see a decorrelation and as we have seen that the PDP decays almost to zero for the same data so we are not aliasing i.e. the autocorrelation function is sampled above Nyquist rate. We can use the same argument for 0 and 1 loading cases as we need enough samples to avoid aliasing. Since we are limited by the number of samples the VNA can collect, it was decided to take 1500 samples over a bandwidth of 5 MHz spaced every 50 MHz apart such that we get a total of 21 chunks of 5 MHz in the total bandwidth of 1 GHz. The frequency samples spacing and bandwidth of the chunks were selected after a number of experiments which helped determining these frequency parameters for a reasonable estimate. Autocorrelation plot for 1 and 0 loading cases around 1502.5 MHz is shown in Figure (3.12).

In Figure (3.13) coherence bandwidth over a frequency range of 1.5 to 2.5 GHz is shown for all the loading cases. It can be seen that the coherence bandwidth for

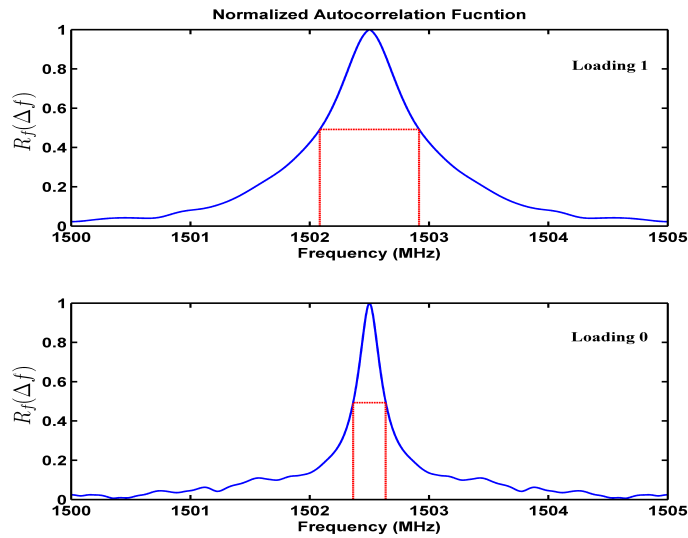


Figure 3.12: Coherence BW for loading 1 and 0 over 5 MHz BW at center frequency of 1502.5 MHz

all loading cases is almost flat over the frequency band of interest. Coherence bandwidth of the channel is an important measure in the wireless communication to determine if the transmitted signal would undergo wideband or narrowband fading, therefore, we decided to plot it over a wide band of frequencies, see Figure (3.14). This enables us to have a ball park estimate of the coherence bandwidth in the chamber for any wireless communication system under test since many commercially available communication system operate in the range of 0.8-6 GHz.

When there is a strong LoS or an unstirred component present the coherence bandwidth would increase. To verify this intuition we plotted the coherence bandwidth for different loadings, because K-factor increases with loading as the power in the multipath components die out more rapidly with more loading. For the case of high loading the autocorrelation over the frequency bandwidth of 20 MHz does not fall below 0.5 which means that there is a strong correlation over a wide frequency bandwidth owing to a high K-factor. In this situation the coherence bandwidth gives a misleading estimate, therefore, a more reliable estimate of the coherence bandwidth in the chamber can be obtained from the RMS delay spread. For the reverberation chamber the relationship between RMS delay spread and co-

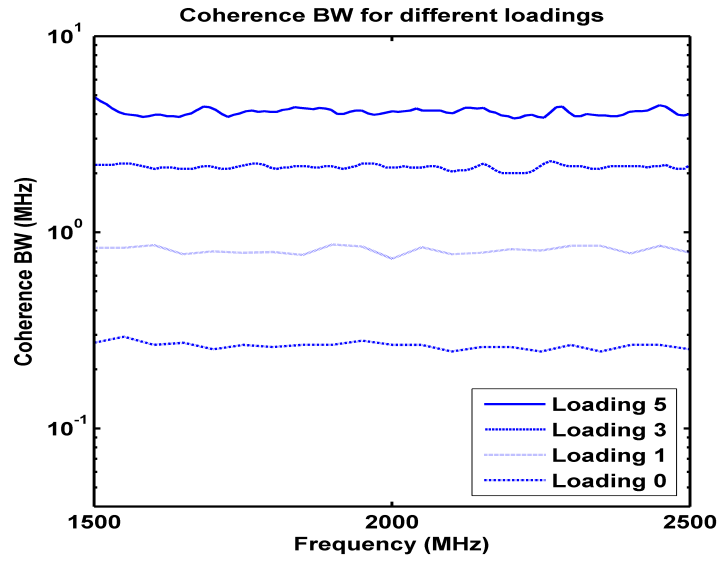


Figure 3.13: Coherence BW for all loadings over 1 GHz bandwidth

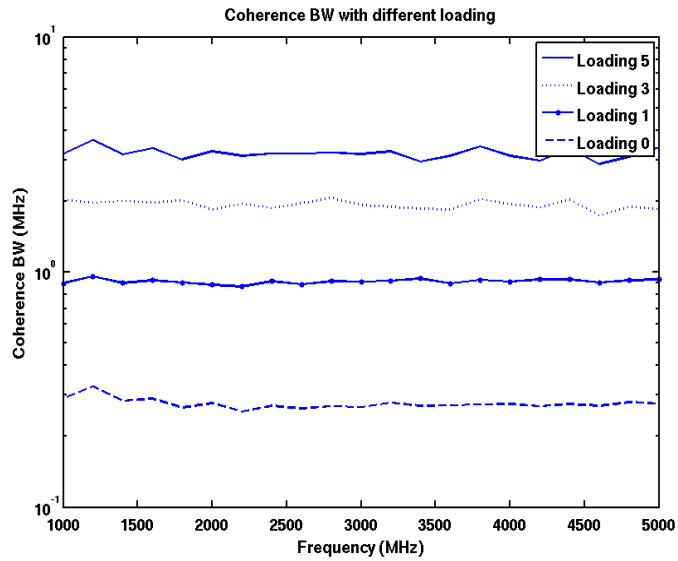


Figure 3.14: Coherence BW for all loading over 5 GHz Bandwidth

herence bandwidth is derived ⁴ and in general it is given as ⁵,

⁴See Appendix C

⁵See Appendix A

$$A_c(\Delta f) = \frac{k}{\tau_{RMS}} \quad (3.9)$$

The constant k for the chamber theoretically turns out to be 0.55. In Figure (3.15) and (3.16) we showed the autocorrelation over frequency bandwidth of 40 MHz for loading 3 and 5 and over frequency bandwidth of 20 MHz for loading 0 and 1. From the figures it can be seen that the noise floor has increased and the autocorrelation function does not go to zero. This correlation is due to the LoS component in the signal and it gives misleading results.

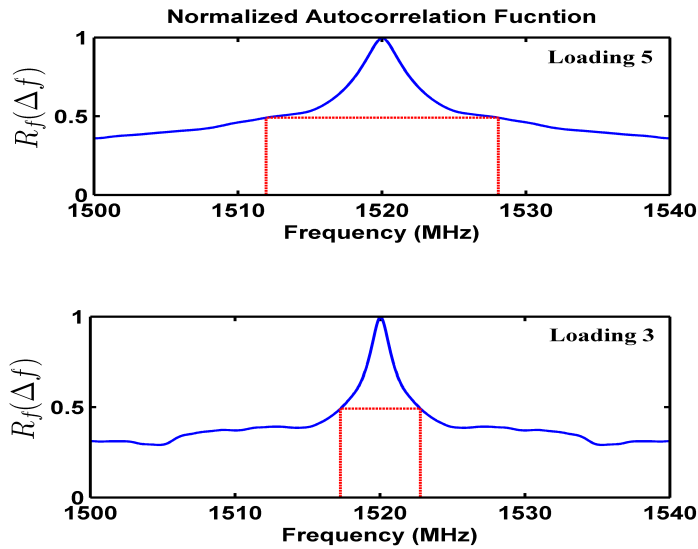


Figure 3.15: Coherence BW for loading 3 and 5 over 40 MHz in the presence of LoS component

When there is no or low loading many multipath components arrive at the receiver with sufficient power such that we can get a reasonable estimate of coherence bandwidth but it should be noticed that the noise floor still does not go down to zero for 0 and 1 loading cases however the estimated coherence bandwidths are close to the Rayleigh environment case. It is still suggested that a better estimate of coherence bandwidth in the case of LoS component could be estimated from the delay spread τ_{RMS} measured from the power delay profile, once the constant for the environment is determined. In Figure (3.17) we plotted the RMS delay spread τ_{RMS} using the relation in (3.9). For $k = 0.45$ it shows a very close agreement

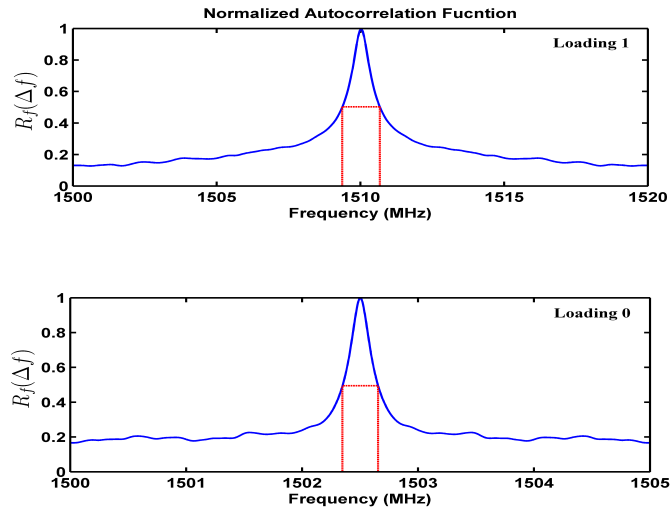


Figure 3.16: Coherence BW for loading 0 and 1 over 5 and 20 MHz respectively in the presence of LoS component

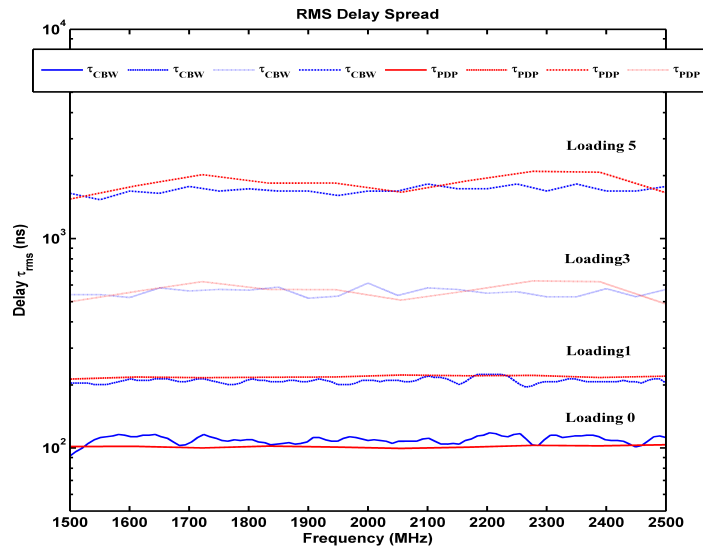


Figure 3.17: RMS Delay spread calculated from PDP and Coherence bandwidth

with the delay spread calculated from the power delay profile. Delay spread from the power delay profile is evaluated over a frequency range of 1.5-2.5 GHz for

center frequencies every 100 MHz apart and using filter bandwidth of 200 MHz around the center frequencies.

3.6 Coherence Time

Delay spread and coherence bandwidth are the parameters that describes the time dispersive nature of the channel in a local area. However, they do not offer any information about the time-varying nature of the channel caused by the relative motion between the mobile and base station or by movement of scatterers in the channel or environment. To completely characterize the channel we need to know how it behaves both in the time and frequency domains. Coherence time gives the second-order statistics of the channel and is used to characterize the time-varying nature of the frequency dispersiveness of the channel in the time domain. The basic theory for characterizing the channel in the time domain is presented in Appendix A.4.3. Coherence time is a statistical measure of the time variation over which the channel impulse response is essentially invariant, and quantifies the similarity of the channel response at different times. If the symbol duration is greater than the coherence time of the channel than the channel will change during the transmission of the baseband signal, thus causing frequency distortion at the receiver. If the coherence time is defined as the time over which the time correlation function is above 0.5 then it is given approximately as [7]

$$T_c \approx \frac{9}{16\pi B_D} \quad (3.10)$$

where B_D is the maximum Doppler shift or Doppler spread given by $B_D = \frac{v}{\lambda}$, where v and λ are the velocity of the moving object and the wavelength of operational frequency respectively. The general relation between coherence time and Doppler spread is given as,

$$B_D \approx k/T_c \quad (3.11)$$

In practice for $k = 1$ the relation suggests the time duration during which a Rayleigh fading signal may fluctuate widely, where (3.10) is often too restrictive. A popular rule of thumb for digital communication is to define the coherence time as a geometric mean of both (3.10) and (3.11). That is

$$T_c = \sqrt{\frac{9}{16\pi B_D^2}} = \frac{0.423}{B_D} \quad (3.12)$$

3.6.1 Measurements in reverberation chamber

In the reverberation chamber the transmitter and the receiver are fixed and the only motion or cause of time selectivity of the channel is due to the movement of stirrers. This corresponds to a channel in which the environmental motion is the primary cause of fading, thus we need to know the velocity of the object moving around the transmitter since that would determine the maximum Doppler shift experienced by the modulated signal. In order to calculate the angular velocity of the stirrers a vector network analyzer is used in the continuous wave mode, the chamber is unloaded, the antennas are cross-polarized and facing towards the stirrers away from each other. This configuration is setup to emulate a Rayleigh channel in the chamber by stirring in the most effective way. Loading can have an effect on the channel statistics as we have seen in the frequency domain therefore initially we do not load the chamber to study a purely Rayleigh channel. The stirrers in the chamber are controlled by a controller via software and can be rotated at different angular velocity by selecting different speeds designated RPM on the controller from 1-8. To verify what speed each number corresponds to we transmitted a continuous wave at 2 GHz in the chamber and recorded the complex received signal over time. We made sure to record the signal for at least 3 complete revolutions of the stirrer at each speed so that we can pick out the periodicity in the envelope autocorrelation every time the stirrers make one complete revolution. As the VNA also reports the time vector we can determine the time by picking out the autocorrelation peaks and extracting the corresponding time taken by the stirrers to complete one revolution. In this measurement we relied on the repeatability of the chamber, see Table 3.7.

The revolution time can be related to angular velocity which is a measure of traversed angle per unit time. This is given by $\omega = \frac{2\pi}{t}$, where t is the time each stirrer takes for one complete revolution. The angular velocity of the paddles, the difference and the accumulative error over one complete revolution are given in Table 3.8.

This table shows that for different speeds the controller moves each paddle with a different angular velocity. This can be seen from the difference where for lower speed the offset is higher such that after 360° both the stirrers are offset by 9.2°

Table 3.7: RPM settings relation to Revolution time

RPM	Time per revolution		
	Stirrer 1 (sec)	Stirrer 2 (sec)	Stirrer 1 and 2 (sec)
1	31.6	30.8	31.2
2	15.9	15.71	15.77
3	10.54	10.47	10.5
4	7.89	7.86	7.87
5	6.32	6.30	6.31
6	5.42	5.40	5.41
7	4.64	4.63	4.64
8	4.061	4.048	4.05

relative to the point where they started. This can be seen in Figure (3.18). However we are still able to pick up a small peak in the autocorrelation function for the first revolution but since this autocorrelation function is over 4 revolutions, it is obvious that for the second and third revolutions the channel is completely decorrelated since now the accumulative error is 18.4642° and 27.6960° respectively. The low autocorrelation peak after the first revolution gives us an average time of the revolution of both the stirrers. This average time turns out to be the same as if we take the average of revolution time of each stirrer as can be seen in Figure (3.18) and verified from Table 3.7.

The accumulated error is minimum for RPM 6 and it increases for RPM 7 and 8. This can also be seen in the autocorrelation functions where it shows a stronger correlation after each revolution for RPM 6 compared to RPM 7 and 8. Thus we conclude that the offset in the stirrers' velocity is due to some calibration error in the controller which depends on the speed of the stirrers. Plot of the autocorrelation for RPM 8 in Figure (3.19) shows how the accumulated error lowers the autocorrelation function as the stirrers keep revolving. This should be taken into account since this affects the chambers' repeatability testing. In order to do repeatable test either the controller should be calibrated or each measurement should be done by moving the stirrers back to their initial position and then performing another measurement. This was studied in [19] that when the stirrers are revolved back they move with the same offset such that they come back to their

Table 3.8: RPM Settings relationship to Angular Velocity

RPM	Angular Velocity			Accumulated Error over 360° (θ°)
	Stirrer1 (θ°/sec)	Stirrer2 (θ°/sec)	Difference(θ°/sec)	
1	11.3924	11.6883	0.2959	9.2321
2	22.6415	22.9153	0.2738	4.3178
3	34.1556	34.3840	0.2284	2.3982
4	45.6274	45.8015	0.1740	1.3694
5	56.9620	57.1429	0.1809	1.1415
6	66.4084	66.5927	0.1843	0.9971
7	77.4360	77.6867	0.2507	1.1636
8	88.6481	88.9328	0.2847	1.1543

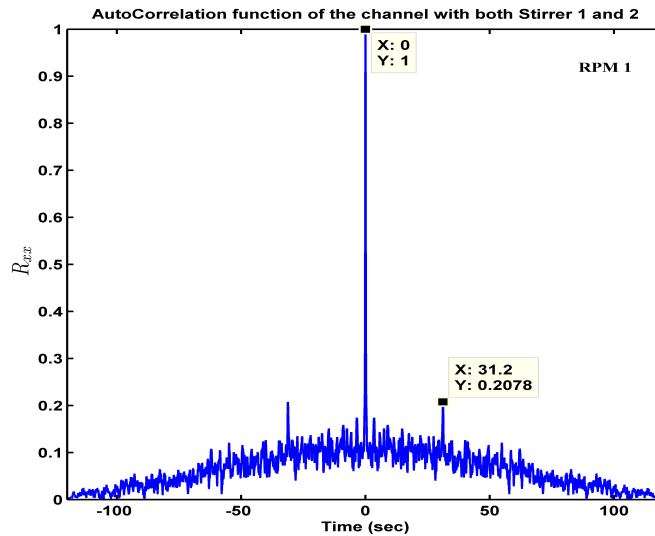


Figure 3.18: Autocorrelation function of the channel with both stirrer 1 and 2 revolving continuously at RPM 1

initial position with negligible displacement error, this is a necessary calibration procedure for the use of chamber facility at NIST.

We have determined the revolution time of the stirrers, for both case when they move one at a time and when they move simultaneously. Now we are in a position to calculate the coherence time of the channel. The coherence time is calculated from the autocorrelation function at a threshold of 0.5 [7]. Figure (3.20) shows the coherence time of the stirrers for RPM 8 and Table 3.9 shows the coherence time of the channel for different angular velocities and stirrer configurations. The angular velocity is a meaningful and representative measure of the speed and can be related to RPM from Table 3.8.

It should be noted that stirrer 2 has a higher angular velocity than stirrer 1 for all RPM settings and therefore it is more effective in stirring the modes in the chamber. Thus it results in lower values of coherence time of the channel. This is due to fading which is related to the speed of the stirrers in our application. Fading is an important phenomena and it owes to constructive and destructive interference of the multipath components at the receiving end. To see how coherence time and Doppler spread is effected as a function of stirrer speed and frequency, a measurement is done where S_{21} parameters are collected over a frequency range of 0.8-6

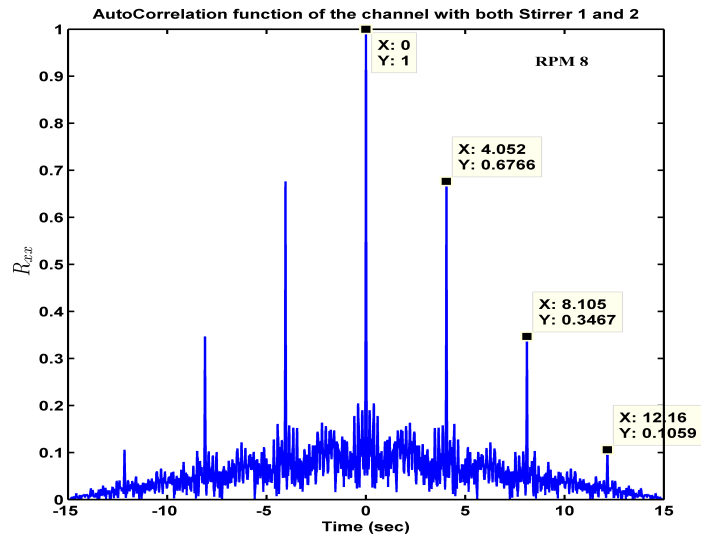


Figure 3.19: Autocorrelation function of the channel with both stirrer 1 and 2 revolving continuously at RPM 8

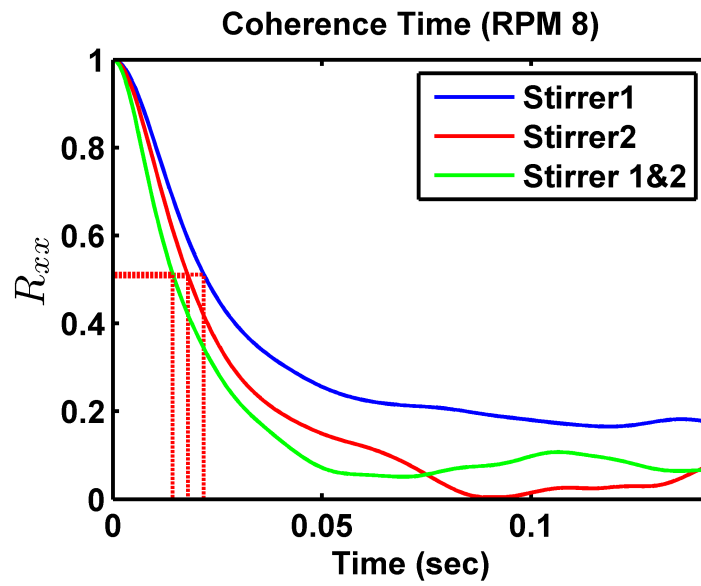


Figure 3.20: Autocorrelation function of the channel at 2 GHz with all stirrer configurations

Table 3.9: Coherence time of the channel emulated in RC

RPM	Coherence Time		
	Stirrer 1 (sec)	Stirrer 2 (sec)	Stirrer 1 and 2 (sec)
1	0.1920	0.1680	0.1080
2	0.0870	0.0720	0.0600
3	0.0680	0.0440	0.0360
4	0.0405	0.0540	0.0255
5	0.0315	0.0300	0.0240
6	0.0260	0.0240	0.0180
7	0.0255	0.0210	0.0150
8	0.0217	0.0180	0.0134

GHz by stepping the paddles every 0.5° . This data is collected for loading 0, 3 and 5. From Table 3.9 we can see that stirrer 2 is more effective than stirrer 1 and both stirrer 1 and 2 together result in smaller coherence time values which means that the channel decorrelates faster. We showed in Figure (3.21) that coherence time is a function of frequency and stirrer speed. It decreases for higher frequencies and stirrer speeds. This is intuitive since at higher frequency a small change in path length can change the phase significantly because each multipath component will be more random in phase, the addition of multipath components at the receiver would result in relatively severe fading. The same argument holds for stirrer speed since at higher angular velocity they stir the EM waves more effectively and the Doppler spread in the frequency increases meaning that coherence time decreases. Coherence time also depends on loading of the chamber, loading reduces the number of effective multipath components as RF absorbers are used as loads to absorb the power in the EM waves thus it increases the coherence time since the fading is relatively less severe due to lesser multipath components. Figure (3.22) shows how coherence time is effected by loading the chamber.

The underlying physical phenomena of fading as discussed in Appendix A.2 is an important concept as it relates both to coherence time and Doppler spread of the channel. If we relate the coherence time values to the symbol duration we can characterize the channel as slow or fast fading channel.

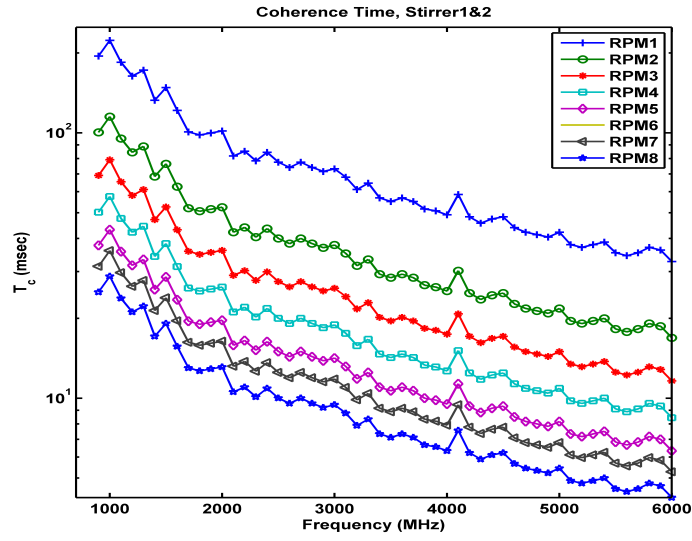


Figure 3.21: Coherence time as a function of frequency and stirrers speeds

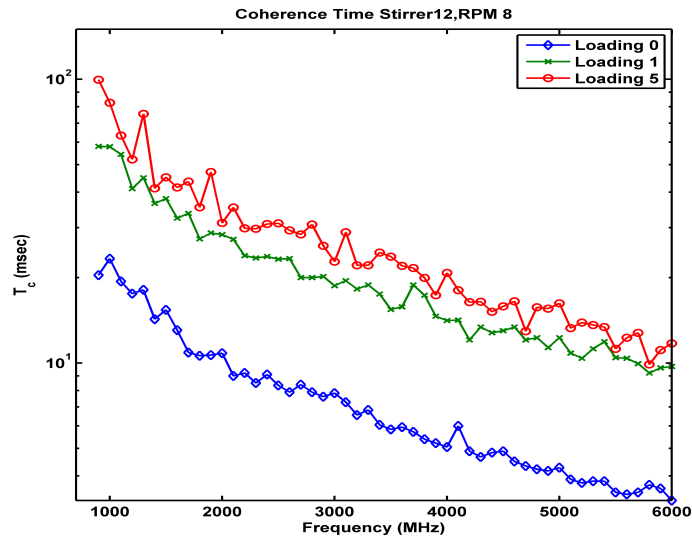


Figure 3.22: Coherence time as a function of Loading

3.6.2 Fading

If the received signal is given by (3.13),

$$r(t) = Re \left\{ \sum_{n=0}^{N(t)} \alpha_n(t) u(t - \tau_n(t)) \exp^{j(2\pi f_c(t - \tau_n(t)) + \phi_{D_n})} \right\} \quad (3.13)$$

and if the stirrers or scatterers are revolved in the reverberation chamber, the channel gain becomes time-varying. Thus for the received signal $r(t)$, the strength will vary at a rate governed by the fluctuations of amplitude α_n , Doppler phase shift $\phi_{D_n}(t)$ and phase changes in the carrier frequency f_c due to path delays τ_n . At higher frequencies a small path delay could result in a large phase change. If we assume that $u(t - \tau_1) \approx u(t - \tau_2)$, then all the multipath components arrive on top of each other, we then argue that over local area α_n varies little but the phase changes owing to the path delays τ_n and Doppler shift $\phi_{D_n}(t)$ causes large fluctuations of $r(t)$. That is, since $r(t)$ is the phasor sum of the individual multipath components, the instantaneous phase of the multipath components cause large fluctuations which typifies small scale fading for CW signal. This is also referred to as narrowband fading since the bandwidth of the received signal is much smaller than that of the channel. However, if $|\tau_1 - \tau_2| \gg B_u^{-1}$ that is if the two multipath components are resolvable then the received power varies very little since the individual multipath amplitudes do not change rapidly over a local area. This is also referred to as wideband fading. In [7] it has been shown that the received local ensemble average power of the wideband and narrowband signal are equivalent.

From the coherence time values given in Table 3.9, we concluded that the channel is varying in time much faster when both stirrers are perturbing the fields in the chamber. Figure (3.23) shows coherence time as a function of frequencies and different stirrer configurations. It is obvious that stirrer 1 and 2 together are more effective in stirring the EM waves thus lesser coherence time followed by stirrer 2 and then stirrer 1. This is due to the physical size of the stirrers since in the reverberation chamber at NIST stirrer 2 is bigger in size than stirrer 1 and it has more effective area to scatter the fields. Figure (3.24) shows the envelope of the channel normalized to the RMS amplitude of the fading envelope, for the cases when only one stirrer is moving and when both stirrers are moving simultaneously. It should be noticed that this channel is fast varying and fading dips are deeper when both stirrer 1 and 2 are moving. It is important to point out that we are plotting the $H(t)$ here and not the received signal $r(t)$. We obtain the scattering function S_{21} of $H(f, n)$ in the chamber over a frequency range of 0.8 to 6 GHz by stepping the

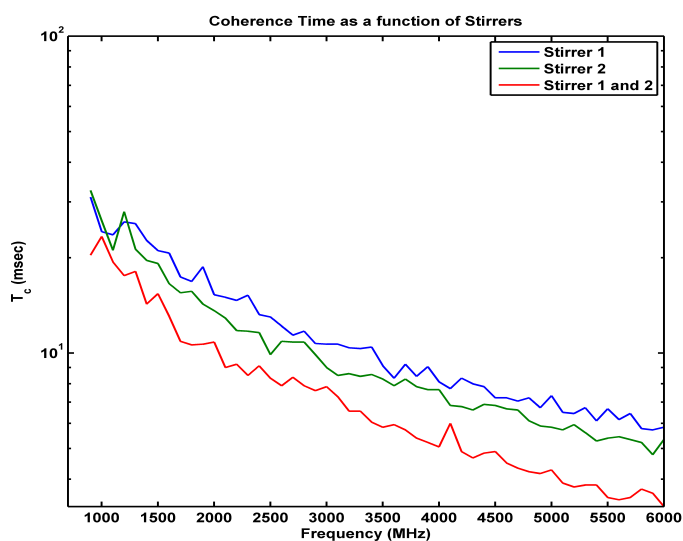


Figure 3.23: Coherence time as a function of stirrers

paddles every 0.5° . This gives us 720 channel realizations as mentioned earlier, for each frequency point where the frequency step is 325 kHz which gives us a total of 16000 frequency points uniformly spaced over the range of 0.8 to 6 GHz. In the post processing we can pick out the frequency of interest and see the channel variations $H(t)$ at the particular frequency. In this case we are interested in the carrier frequency of 2 GHz. From the underlying physical process of fading we can conclude with confidence that both stirrers together increases the scattering in the channel and at the receiver there are more scattered multipath components with approximately the same power and random phases. These multipath components add up together constructively and destructively resulting in variations in the received signal envelope. This physical phenomena is less severe when only one stirrer is rotated. In that case, in the reverberation chamber there is more unstirred received energy which makes the power variation less severe since the phase and the amplitude of the unstirred components dominates that of the multipath components. The multipath components now add up on top of some averaged received power in the unstirred fields.

To prove the underlying physical process of fading owing to phasor addition of multipath components we plot the channel envelope normalized to RMS voltage level of the signal for different frequencies of CW signal and compare them in

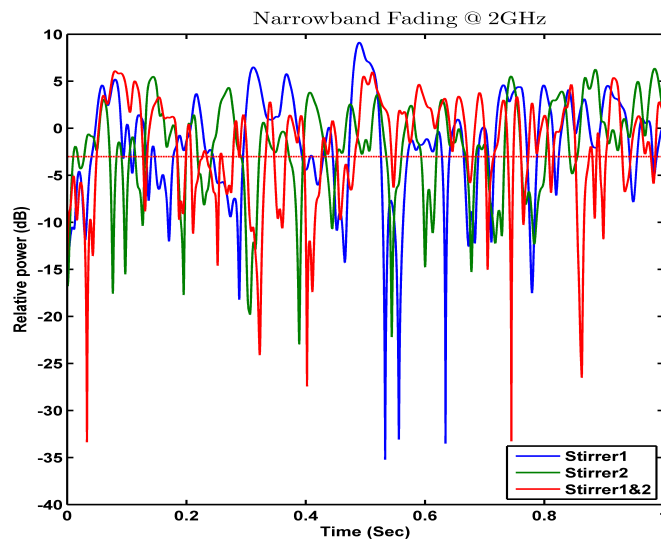


Figure 3.24: Channel fluctuations (Fading) for different stirrer configuration @ 2 GHz

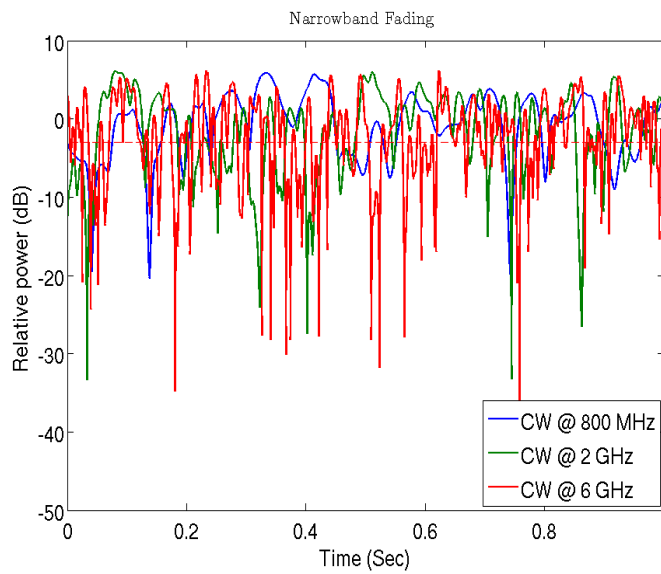


Figure 3.25: Channel fluctuations for different CW frequencies when both the stirrers are moving at RPM 8, Threshold is defined at $\rho = \sqrt{0.5}$

Figure (3.25). It shows that as we increase the frequency the fading become more rapid. This is because at higher frequencies a small path delay results in a large

phase shift, also the motion due to the stirrers adds to the phase variation because of the Doppler shift in the frequency. At a higher frequency the Doppler spread is higher because a small shift in frequency translates to a larger frequency deviation. This can be seen from (3.14).

$$B_D = \frac{v}{\lambda} \cdot \cos\theta \quad (3.14)$$

Where v is the velocity of the receiver and transmitter with respect to each other, λ is the wavelength of the carrier frequency and θ is the direction of arrival of the incoming signal.

In our case the velocity v is due to the stirrers. Keeping v fixed and assuming the maximum Doppler shift is for $\theta = 0$, we can see that at higher frequencies the Doppler shift would be larger. Thus fading depends on the frequency of operation and the relative motion of the receiver or transmitter. Fading is also influenced by the motion of objects in the environment in the case where receiver and transmitter motion are very slow compared to objects in the environment. This is the case in the reverberation chamber where the channel is emulated by moving the stirrers while receiver and transmitter are fixed. This is referred to as fixed wireless communication. From these experiments we can conclude that small scale variations or fading depends upon a number of factors:

- Multipath Propagation
- Relative Speed of the Tx or Rx
- Relative Speed of the surrounding objects
- Carrier frequency of the transmitted signal

Flat fading or narrowband fading is historically the most common type of fading described in the technical literature. The envelope of narrowband fading signal is modeled as Rayleigh distributed when there is no LoS component and Rician distributed when there is a LoS component and the power in the signal is modeled as exponentially distributed. These are the first order statistics of the channel and provide no information about how fast or slow varying the channel is. The rate at which the signal fading occurs may be characterized by the Level Crossing Rate (LCR) and Average Fade Duration (AFD) at a selected threshold below the

mean signal strength (which depend on first and second-order statistics of the fading signal) or by the Doppler spectrum (which depends only upon the second order statistics)⁶.

3.7 Fast fading

In a fast fading channel the channel impulse response changes rapidly with in the symbol duration i.e. $T_c \ll T_s$, this causes frequency dispersion (also called time selectivity) due to Doppler spreading, which leads to signal distortion, where T_c is coherence time and T_s is symbol duration. In the frequency domain, signal distortion due to fast fading increases with increasing Doppler spread relative to the bandwidth of the transmitted signal. In summary the signal undergoes fast fading if,

$$T_c \ll T_s \quad (3.15)$$

$$B_D \gg B_s \quad (3.16)$$

where B_D and B_s are Doppler spread and signal bandwidth respectively.

3.8 Slow fading

In a slow fading channel, the channel impulse response changes at a much slower rate than the transmitted base band signal. In this case the channel may be assumed to be static over one symbol or several symbols duration. In the frequency domain this implies that the Doppler spread of the channel is much lesser than the bandwidth of the baseband signal. The signal goes slow fading if

$$T_c \gg T_s \quad (3.17)$$

$$B_D \ll B_s \quad (3.18)$$

⁶See Appendix A

It should be clear that the velocity of the T_x or R_x (or velocity of objects in the channel) and the baseband signaling determines whether a signal undergoes fast fading or slow fading.

3.9 Level Crossing Rate

To characterize the temporal behavior of the channel we can calculate the envelope level crossing rates (LCR) at different thresholds. The channel envelope is normalized to its RMS value and the crossings of the envelope in the downward direction per second are counted. This shows how fast varying the channel is in time. Channel variation determined by the LCR also depends on the selected threshold. The maximum crossing rate is obtained for the threshold level set to 3dB below the RMS envelope level, level crossing rate is decreased below and above the RMS level. The signal envelope experiences very deep fades occasionally but shallow fades are frequent, this can be seen in Figure (3.24) where the threshold is marked at 3 dB below the signal RMS level which corresponds to $\rho = \sqrt{0.5}$ in (3.19). This equation is valid if there is no LoS component and the channel statistics are Rayleigh distributed.

$$L_z = \sqrt{2\pi} f_D \rho e^{-\rho^2} \quad (3.19)$$

In case of a LoS component the (3.20) gives the level crossing rate of the channel envelope.

$$L_z = \sqrt{2\pi(K+1)} f_D \rho e^{-K-(K+1)\rho^2} I_0(2\rho\sqrt{K(K+1)}) \quad (3.20)$$

Since the chamber is unloaded and antennas are cross polarized we know the channel statistics are Rayleigh distributed see Section 2.2. An algorithm calculates the crossings of the channel envelope per second at certain thresholds in the downward direction. The calculated LCR is then compared to the LCR calculated from (3.19), which is based on the maximum Doppler (f_D) in the channel. The RMS Doppler spread in the channel is calculated as described in Section 3.11. The theoretical curves are then calculated based on RMS Doppler spread. The experimental LCR curves were a little offset from the theoretical curves where theoretical curves gave lower LCR, it was expected because we used the RMS Doppler spread

in the (3.19) instead of maximum Doppler spread in the channel. To get the actual maximum Doppler in the channel the theoretical LCR curves should agree with the experimental curves for certain value of maximum Doppler spread f_d . The RMS Doppler value was multiplied with a factor which gave the best agreement between the curves. Intuitively the factor has to be greater than 1 to get the maximum Doppler in the channel and it turned out to be 1.4. In Figure (3.26) the LCR curves for different threshold level are shown. The LCR curves are plotted for all stirrer configurations, here stirrers configuration are defined as configuration 1, when only stirrer 1 is used. Configuration 2, when only stirrer 2 is used and configuration 3, when both the stirrers are used and these are summarized in Table (3.10).

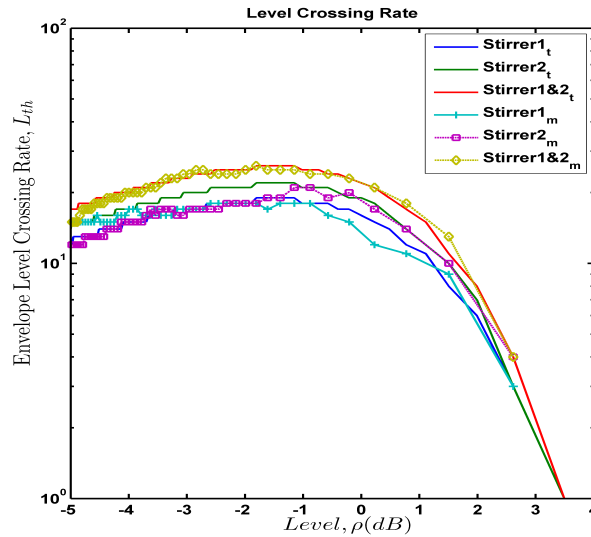


Figure 3.26: Envelop Level Crossing Rate for all stirrers configuration at different threshold levels, ρ

From previous findings on coherence time value for stirrer configurations, we can see that LCR for configuration 3 is higher than for configuration 2 and 1. Each stirrer shows the maximum LCR at the threshold level of $-1.5dB$ which corresponds to $\rho = \frac{1}{\sqrt{2}}$ i.e (3 dB below the RMS envelope level). The curves for configuration 1 and 2 show disagreement for very low and very high threshold levels but this is only because we do not have data for channel variation over longer periods of time otherwise these curves would also have agreed closely for very low and higher threshold levels since the theoretical curves are based on infinite real-

Table 3.10: *Stirrers Configuration in the Chamber*

Configuration Number	Stirrer used
1	Stirrer 1
2	Stirrer 2
3	Stirrer 1 and 2

ization of a random process (in this case Rayleigh Channel). When configuration 1 and 2 are used, there is also some unstirred energy (LoS component) which can change channel statistics from Rayleigh to Rician with low value of K . Although for very low values of K the first order statistics do not change significantly. It can still effect the second order statistics such that the LCR curves for lower or higher threshold levels than $\rho = \frac{1}{\sqrt{2}}$ starts to disagree from the theoretical curves ($K=0$). The deep fades that we observe in a Rayleigh channel are not so frequent in a Rician channel. This can be explained from Figure (3.16) where the autocorrelation function of the channel in case of a LoS component with some $K > 0$ and with 0 loading case does not fall off to zero showing some degree of correlation because of the LoS component. When we talk about the fading process, the phasor sum of all the multipath components is dominated by the phase and amplitude of the LoS component and thus deep fades which occur due to total cancellation in the phases and amplitude of all the component adding up at the receiver is now less likely because of phase and amplitude of LoS component dominates the phasor addition. It is shown in [20] that for values of $K > 0$ the LCR decreases at lower and higher thresholds levels than $\rho = \frac{1}{\sqrt{2}}$. Thus in the RC we can get higher Doppler by stirring more effectively (i.e both the stirrers) and also by changing the speed of the stirrers which is most commonly related to Doppler spread in the channel thus in a reverberation chamber we have two degrees of freedom to emulate a channel with different Doppler spreads.

Level crossing rate characterizes the fading envelope. In mobile wireless communication it is an indicator of how fast the receiver and transmitter are moving relative to each other and in fixed wireless communication it indicates how fast the environment is changing between the transmitter and receiver. As we discussed that the fading rate depends on the frequency of operation and the speed of the stirrers, in the chamber it also depends on the number of stirrers used to scatter

the multipath components since all these factor changes the Doppler spread in the channel. In the real world the analogy to more stirrers is more scatterers in the environment producing the multipath components with different Doppler shifts that depends on the speeds of the scatterers. All these factor would effect the LCR estimate of the fading envelope too. Figure (3.30) shows how Doppler spread changes as a function of frequency and speed of the stirrers, in the chamber when both the stirrers are revolving at different angular velocities.

3.10 Average Fade Duration

Average fade duration is an important quantity that gives an average amount of time for which the signal envelope is below a certain threshold. As level crossing rate help us to relate the fading rate to the speed of the mobile terminal (in case of mobile communication) similarly average fade duration helps us to predict the bit-error-rate of a communication link by comparing the symbol duration T_b to average fade duration \bar{t}_z given by (3.21). This equation is valid for Rayleigh distributed channels.

$$\bar{t}_z = \frac{e^{\rho^2} - 1}{\rho f_D \sqrt{2\pi}} \quad (3.21)$$

For Rician distributed channels the average fade duration is calculated by (3.22).

$$\bar{t}_z = \frac{(1 - Q(\sqrt{2K}, \sqrt{2(K+1)\rho^2}))e^{K+(K+1)\rho^2}}{\sqrt{2\pi(K+1)}f_d\rho I_0(2\sqrt{K(K+1)\rho})} \quad (3.22)$$

To calculate the average fade duration at different threshold levels for experimental data, an algorithm was written which calculates the average time for which signal envelope is below a certain threshold. Thus we obtain curves for AFD for the same threshold levels as we used in calculating the LCR. To calculate the theoretical curves based on (3.21) same Doppler spread was used as for calculating the LCR. The chamber configuration is same as used before, therefore, we compare the experimental curves to the theoretical curves for Rayleigh channel. Figure (3.27) shows the comparison between measured and theoretical curves. For a fast fading envelope the average time for which envelope is below a threshold level is lesser compared to slow fading envelope which has greater average fade durations. This

can be verified from the Figure (3.27) which shows that average fade duration for stirrer configuration 1 at a certain threshold level is greater than stirrer configuration 2 followed by configuration 3. If symbol duration $T_b \approx \bar{t}_z$, where \bar{t}_z is average fade duration of a signal, then the system will likely experience single error event where the bits received in error have previous and subsequent bits received correctly (since signal level is greater than the threshold level). On the other hand, if $T_b \ll \bar{t}_z$ then for many subsequent bits the signal level is below the threshold level, so large burst of errors are likely. Finally if $T_b \gg \bar{t}_z$ then, since fading is integrated over a symbol time in the demodulator, the fading gets average out and so can be neglected. Thus it is a very important parameter in designing error control codes.

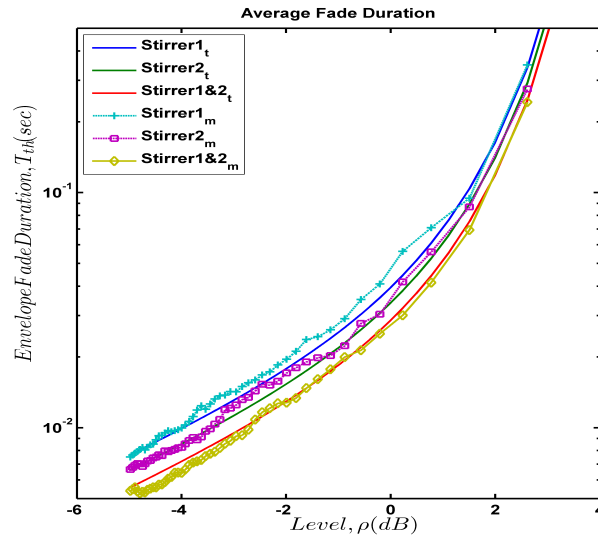


Figure 3.27: Envelop average fade duration for all stirrer configuration at different threshold levels, ρ

3.11 Doppler Spread

The fading rate of signal can also be characterized by the Doppler spread in the channel. This representation is useful because it is a key input for many algorithm used to simulate fading channels. The time variation in the channel due to motion causes Doppler shift in the signal. This Doppler can be characterized by taking the Fourier transform of $R_H(\Delta f; \Delta t)$ relative to Δt .

$$S_c(\Delta f; \rho) = \int_{-\infty}^{\infty} R_H(\Delta f; \Delta t) e^{-j2\pi\rho\Delta t} d\Delta t. \quad (3.23)$$

To characterize Doppler at a single frequency, Δf is set to zero and then define $S_c(\rho) \triangleq S_c(0, \rho)$, then,

$$S_c(\rho) = \int_{-\infty}^{\infty} R_t(\Delta t) e^{-j2\pi\rho\Delta t} d\Delta t. \quad (3.24)$$

In the equation above $R_t(\Delta t)$ is an autocorrelation function which tells how the channel impulse response decorrelates over time, see Appendix A.1 . To measured the Doppler spread in the reverberation chamber we begin with the time varying channel transfer function $H(f, n)$. A vector network analyzer is used to obtain the channel transfer function $H(f, n)$ from the reverberation chamber at different stirrer positions 'n', which corresponds to discrete time. Each stirrer corresponds to a new channel realization and makes the channel transfer function time varying as the stirrers revolve. In this experiment the stirrers were stepped every 0.5 degrees such that we had 720 channel realizations over a complete (360°) revolution, the frequency was swept from 0.8 to 6 GHz. During the data collection process all stirrer configurations were used. The aim was to study the contribution of each stirrer to the Doppler spread in the channel.

The Doppler spread is estimated from the time autocorrelation function, in our case it is the autocorrelation over the stirrer position at each frequency point which is given as,

$$R_t(f, \Delta n) = \mathbf{E}[H(f, n)^* H(f, n + \Delta n)] \quad (3.25)$$

where $\mathbf{E}[\cdot]$ represent the mathematical expectation, if ρ represent the Doppler frequency then it can be estimated from the time autocorrelation function of the channel by (3.24). For computational convenience we resort to the mathematical operator of convolution and properties of the Fourier transform. Note that with $R_t(f, \Delta n)$ being complex conjugate symmetric, its Fourier transform $S_c(f, \rho)$ is real. Thus the autocorrelation function given by (3.25) is equivalent to,

$$R_t(f, \Delta n) = H(f, n) \otimes H(f, -n) \quad (3.26)$$

where \otimes represents convolution. Applying Fourier transform to both sides of (3.26) with respect to Δt , we obtain

$$S_c(f, \rho) = H(f, \rho)H^*(f, \rho) = |H(f, \rho)|^2 \quad (3.27)$$

Equation (3.27) gives the power spectral density with respect to Doppler frequency (ρ) and is equivalent to (3.24). The later equation is computationally intense to estimate the power spectral density, therefore, we resort to (3.27). This equation is handy to implement since the time varying channel transfer function $H(f, n)$ is the same as the $S_{21}(f, n)$ measured with the VNA under stationary conditions. It should be mentioned that we used complex channel amplitude to estimate the Doppler spectrum. Since VNA sweep time is much longer than the coherence time of the channel, therefore, it would not give the frequency response at a particular stirrer position and at all frequencies in the sweep range if the stirrers were moving during the sweep. To get the channel response for a particular stirrer position over the frequency range, we measure the VNA response under stationary condition which means no Doppler shifts. However we can relate the stationary measurement to time axis and by the Fourier transform relationship we can estimate the Doppler spread in the channel. To relate the Doppler axis (ρ) to time axis we measured the time it takes for the stirrers to complete one revolution at different speeds. The time for different speed settings are given in Table 3.7. If the total time for one complete revolution of the stirrers is given by T_{rev} and the measurement is taken while stepping 0.5° then we get 720 samples for every frequency point. Thus the sampling time is given as $\Delta T = T_{rev}/720$. From the Fourier theory we know that the maximum frequency that can be captured in a signal is related to sampling frequency by $F_s = 2F_{max}$ and also that $\Delta T = 1/F_s$ by virtue of these relations we can translate stirrer revolution speed to Doppler frequency axis by (3.28).

$$\rho_{max} = \frac{1}{2\Delta T} \quad (3.28)$$

By convention the Doppler spectrum ranges from $[-\rho_{max}, \rho_{max}]$. To follow the convention we map the discrete frequency points to the Doppler axis by the equation $((-N/2 : N/2 - 1)/N) * F_s$, where N is the total number of frequency samples. This novel approach enables us to determine the Doppler spread in the channel even though the measurements were taken under static conditions. This

approach was discussed during the preparatory work of this thesis and was implemented at Chalmers University [21]. The Doppler spread B_D is defined as the maximum Doppler frequency ρ for which $S_c(f, \rho)$ is greater than zero or above a defined threshold. To avoid the ambiguity in selecting different threshold levels we decide to use RMS Doppler bandwidth as a measure of Doppler spread in the channel. Once we have the Doppler power spectrum by using (3.27) and the Doppler frequency axis, it is straight forward to calculate RMS Doppler spread from (3.29).

$$\rho_{max} = \left[\frac{\int \rho^2 S_c(f_o, \rho) d\rho}{\int S_c(f_o, \rho) d\rho} \right]^{1/2} \quad (3.29)$$

In the above equation f_o indicates that the Doppler power spectrum is estimated for a particular frequency of interest. Figure (3.28) shows the average Doppler spectrum of channel over 1 GHz bandwidth centred around 2 GHz, for configuration 3. We used a theoretical model proposed in [22] for indoor wireless channel where the fading or Doppler spread is due to the motion of objects moving in the environment and their motion is typically very slow. The model is defined as,

$$S_c(\rho) = \frac{1}{1 + A\rho^2} \quad (3.30)$$

where A is a constant selected such that at a given Doppler frequency ρ_d , $(S_c(\rho))|_{\rho=\rho_d} = 0.1$ it can be calculated as.

$$A = \frac{9}{f_d^2} \quad (3.31)$$

Since ρ_d corresponds to $S_c(\rho) = 0.1$ which is 10 dB below the maximum it approximately equals to the RMS bandwidth of the Doppler spectrum in this case. We use RMS Doppler spread to calculate the constant 'A' for the fit. This model shows good fit for Doppler spectrum estimated for CW signal but in Figure (3.28), we have plotted the Doppler spectrum averaged over 1 GHz bandwidth thus we calculate the RMS Doppler spread for this spectrum and used it to determine the factor A which shows a good fit and it turned out that the Doppler spectrum at lower frequencies dominate the average Doppler power spectrum. The RMS Doppler spread is decreased for the average Doppler spectrum as compared to the Doppler spread estimated at 2 GHz.

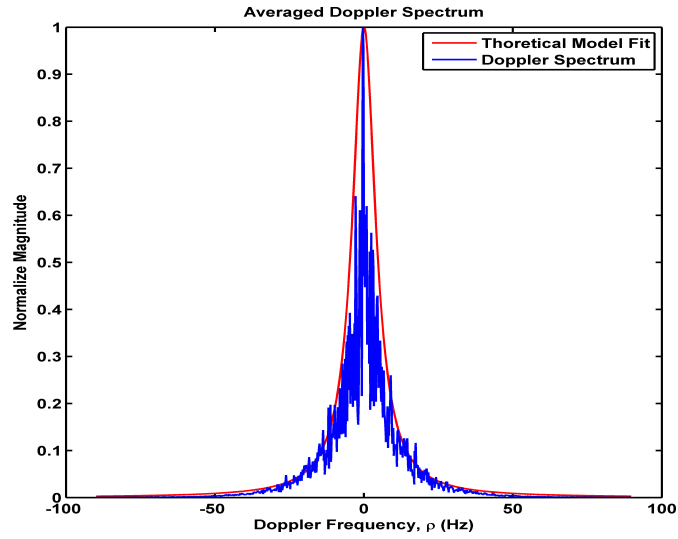


Figure 3.28: Average Doppler spread in the Reverberation Chamber

3.12 Shape of the Doppler Spectrum

It is interesting to point out that the shape of the measured Doppler spectrum is not the most well-known U or tub-shaped Doppler spectrum introduced by Jakes [23]. In general there are two primary aspects of wireless channel time variations. In the first type the user is moving relative to the base station or vice versa. In this case the time variation of the received signal are related to the spatial variation of the electromagnetic fields through a constant (i.e relative velocity). In the second type, the base station and the user are both stationary, but the reflectors in the environment are moving, causing time variation in the channel. In the reverberation chamber we encounter the second type of channel variation that is caused only by the motion of stirrers in the chamber. This type of communication where the T_x and R_x are fixed is also known as fixed wireless communication. A theoretical model has been studied in [24] for fixed wireless communication channels. It describes the time-variation of indoor channels when both the transmitter and receiver are stationary and only reflector move in the environment. It has been shown that the resulting Doppler spectrum peaks at the center (i.e. the carrier frequency) and falls off exponentially. This agrees with the shape of Doppler spectrum that we measure in the chamber as shown in Figure (3.28). It should be very clear here that in

the reverberation chamber the type of fading on the channel is due to the stirrers revolving in the chamber. We have seen that our emulated channels second order statistics i.e. LCR and AFD agrees very well with the theoretical curves which are derived for a Jakes spectrum that is when we have mobile communication. We conclude that the fading characteristics are the same as long as the Doppler shift introduced by the motion of either the T_x , R_x itself or scatters is the same. The Doppler spectrum shape shows what kind of motion is causing the time variations. For fixed wireless communication the same exponential decaying spectrum shape has been reported in [25], [26] where measurements were conducted in the real world environment.

3.12.1 Measurements in reverberation chamber

We have calculated the Doppler spread for each stirrer configuration over the frequency range of 0.8 - 6 GHz. Figure (3.29) and (3.30) shows the Doppler spread as a function of stirrers angular velocity and frequency, for Stirrer configuration 1, 2 and 3. It shows that Doppler spread increases linearly with frequency. As discussed in Section 3.6.2 that for higher frequencies the Doppler spread at the same velocity is higher than for lower frequencies. Doppler spread also increases with velocity of the scatters in a fixed wireless communication system and it agrees with our findings. From these figures by choosing the desired Doppler frequency we can tune the chamber to emulate a desired fading channel for wireless device testing. The maximum Doppler that can be emulated in the chamber in our experiment is approximately 38 Hz at 6 GHz when configuration 3 is used at an RPM 8.

As we have seen in Section 3.6 that the Coherence time and fading also depends on the stirring configuration, therefore, it is also expected to see the inverse dependence in case of Doppler spread since coherence time and Doppler are Fourier transform pair and are related by the inverse relationship.

$$T_c \approx k/B_D \quad (3.32)$$

Where k is a constant depending on the environment. Figure (3.31) shows that configuration 1 is least effective in emulating the Doppler spread followed by configuration 2 and then 3. To determine the constant of proportionality k we plot the autocorrelation function of the chamber with x-axis ($f_d\tau$) having normalized units.

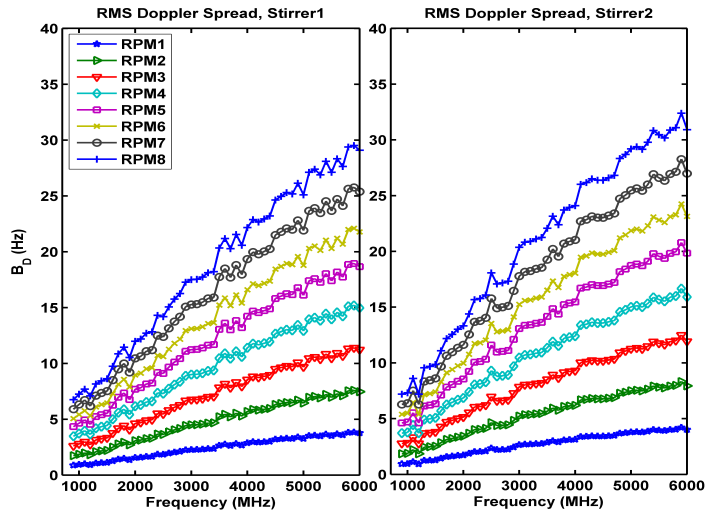


Figure 3.29: Doppler spread as a function of Frequency and Stirrers speed for configuration 1 and 2

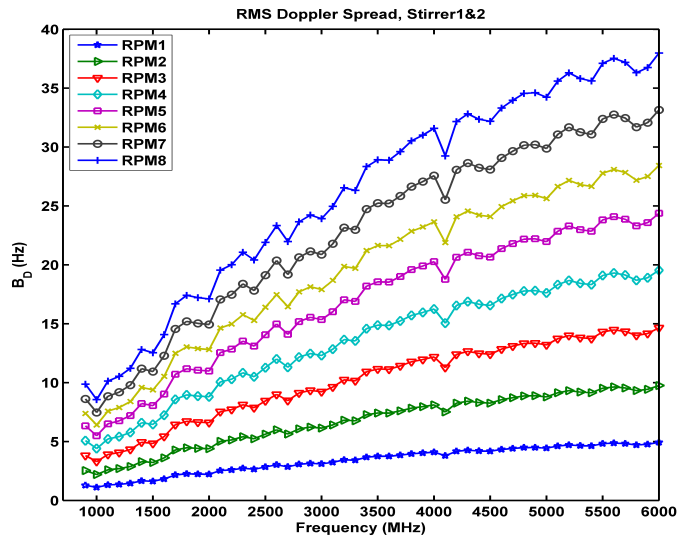


Figure 3.30: Doppler spread as a function of Frequency and Stirrers speed for configuration 3

f_d is the RMS Doppler spread in the channel, since we proposed RMS Doppler as a measure for Doppler spread to avoid ambiguities in defining the threshold level for measuring Doppler see Section 3.11. In Figure (3.32), we showed the normalized autocorrelation function of the channel versus normalized x-axis for stirrer configuration 3 measured for continuous wave at 2 GHz.

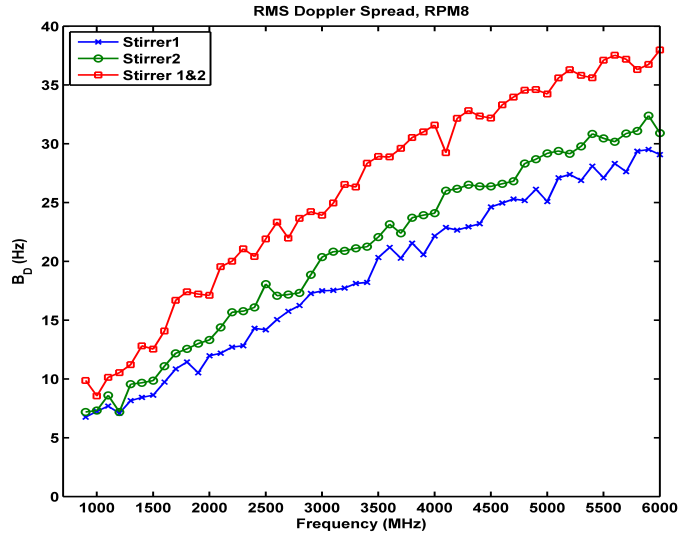


Figure 3.31: Doppler spread as a function of Stirrer configurations

If we consider the decorrelation of channel autocorrelation function at the threshold of 0.5 then we can determine the constant k which turns out to be 0.22. If we use this constant and determine the coherence time from the RMS Doppler spread at 2 GHz for stirrer configuration 3, which can be seen from Figure (3.30) is 17.11 Hz, then using (3.32), coherence time turn out to be 0.0134 sec. This can be compared to the coherence time values in Table 3.9 for stirrer configuration 3 at RPM 8. This also gives us an idea of how much wavelength a part two antennas should be placed for MIMO measurement, as $f_d\tau \approx 0.23$ then $v\tau \approx 0.23\lambda$. One might question that the emulated Doppler spread is too low to replicate a real life environment where the Doppler spread is relatively much higher since the motion is due to the velocity of the R_x and T_x moving at much higher speeds than objects in the environment, e.g. A mobile user traveling in a car at 100 Mph. In such a scenario the fading experienced by the R_x is due to motion of the user as the R_x experiences fading in the channel when it moves through the EM wave interfer-

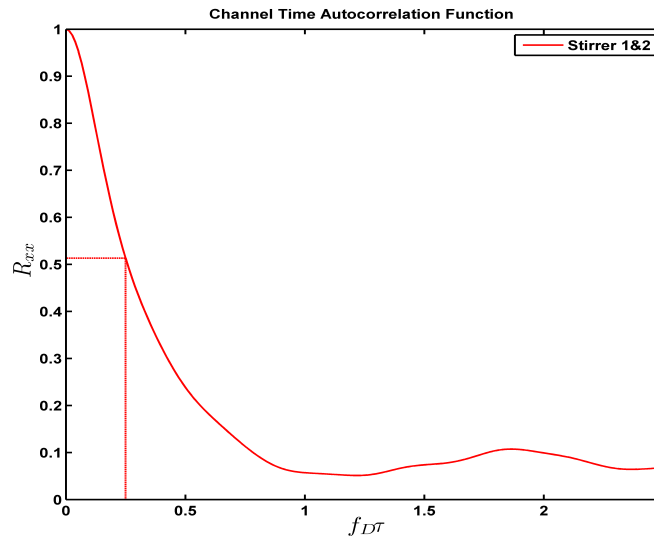


Figure 3.32: Autocorrelation of Channel for stirrer configuration 3 and RPM 8

ence pattern created due to the scatters in the environment. In this case the Doppler spectrum is a Tub or U-shaped assuming isotropic scattering in the environment, which would be almost true for dense urban environment. The fading experienced by a R_x in the reverberation chamber is typical for indoor WLAN communication since it experiences similar indoor environment however if we want to test a mobile phone R_x we need to have a U-shaped or Jakes Doppler spectrum so that the mobile phone experiences fading as if it were moving with a certain velocity that can be determined by the Doppler spectrum. In the recent work with the reverberation chamber it has been shown that Jakes spectrum can be emulated in the reverberation chamber by using a channel fading emulator. In [27], it has been shown that using a channel emulator it is possible to create a fading channel which would give a Doppler spectrum that is convolution of the Jakes Doppler spectrum for mobile wireless communication and the peaky Doppler spectrum for the fixed wireless communication. Figure (3.34) shows the convolution of two Doppler spectrum, this figure is obtained by simulations where discrete-time white complex Gaussian noise is multiplied by the theoretical Jakes and Fixed wireless communication spectrum. This is known as Spectrum method for simulating a wireless channel with spectral properties shaped according to a given spectrum. In this experiment we have simulated Jakes and Fixed wireless channel with different

Doppler spreads and convolved the two Doppler spectrum to show the resulting Doppler spectrum, such a channel is currently being studied by many researchers and is known as a double Rayleigh fading channel where each Rayleigh fading signal has different AFD and LCR corresponding to the Doppler Spread due to the motion of objects and the mobile Rx/Tx. A similar Doppler spectrum has also been emulated in the reverberation chamber by the use of fading emulator to emulate a mobile channel and the stirrers emulate a fixed wireless communication channel where the multiplication of two independent Rayleigh random variables results in a double Rayleigh channel such a channel spectrum is reported and shown in [27].

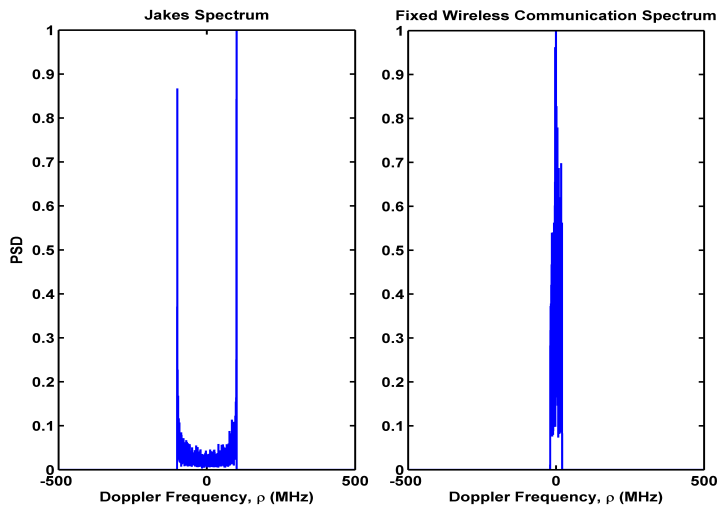


Figure 3.33: Jakes and Fixed Wireless Communication Doppler spectrum's at $F_{D_{max}}$ 100 Hz and 20 Hz respectively

This is typically the type of fading that a mobile receiver would experience in an urban environments where the object (e.g. traffic) plays the role of moving scatterers and the mobile user travelling in a car at 40-50 Mph would experience fading which results in a U shaped Doppler spectrum. Thus by using a fading emulator it is possible to use the reverberation chamber to emulate both fixed and mobile wireless channels specifically for indoor and dense urban environment where the fading is usually much severe. Thus R_x for different applications can be tested in the worst case scenarios in a reverberation chamber. It is also important to show the effect of loading on Doppler since we need to load the chamber to emulate

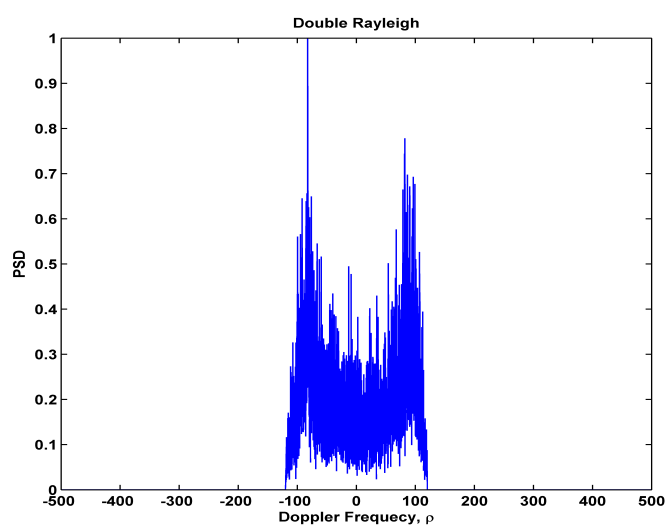


Figure 3.34: Convolution of the Jakes and Fixed Wireless Communication Doppler spectrum's. A typical Double Rayleigh channel Doppler spectrum

low RMS delay spreads typical for indoor wireless communication, fixed or mobile. Figure (3.35) shows how Doppler spread is effected by loading the chamber. It shows that for 0 loading we have a higher Doppler spread since there is more EM waves in the chamber that bounces back and forth and interacts with the stirrers, however as we start to load the chamber this energy get absorbed by the RF absorbers and dies down to the noise floor after a couple of reflections, thus we have less stirred electromagnetic waves in the chamber for higher loading and the Doppler spread start to get smaller. It is interesting to note that for Loading 3 and 5 the RMS Doppler spread is almost in the same order which shows that after a certain Loading the spread in the chamber does not decreases at the same rate as it would for loading 3 compared to no loading case.

3.13 Conclusion

In this chapter we studied a frequency domain channel sounding technique to estimate the impulse response of a wireless channel in the reverberation chamber. This technique is suitable for indoor measurements where the distance between transmitter and receiver is less than 200 meters and measurement equipment like

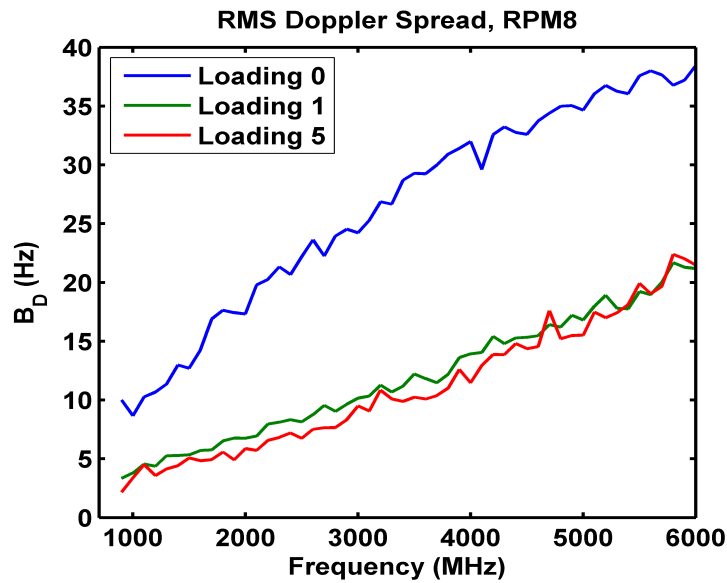


Figure 3.35: Doppler spread as a function of Loading

VNA can be used. The advantage with this technique is that it provides both the phase and amplitude information in the time and frequency domain. To determine the frequency selective nature of the channel at a particular data rate we need to study the power delay profile and coherence bandwidth of the channel. To estimate the power delay profile in the chamber we can IDFT the channel transfer function $H(f, t)$ with respect to frequency. This gives us access to the delay domain. We have seen that in the reverberation chamber the power has an exponential decay and thus we conclude that the mean and RMS delay spread of the channel should be the same as for an exponential power delay profile. However we did not get the same mean and RMS delay spread until we processed the data correctly. It was found that the samples from the chamber rise time have to be discarded from the calculation of the delay spreads so that we only process the exponential power decay. Also aliasing effects have to be considered, when dealing with Fourier transforms. Because the chamber has frequency dependence for no loading case due to wall and antenna losses, it is also concluded that we should operate in the bandwidth of interest to determine the RMS delay spread of the channel in the chamber. When the chamber is loaded the frequency dependence goes away. Typically to get a RMS delay spread that compares to a real life indoor channel, the NIST chamber has to be loaded with at least 4 absorbers. Therefore, to test a wireless system we do not

have to strictly estimate the RMS delay spread in the frequency bandwidth as that of the system under test (Usually narrowband). A wideband frequency measurement would give the same value of RMS delay spread in the chamber as it would be for a narrow bandwidth system but only for high loading cases. We have seen that a high K-factor can also change the delay spread of the channel. Therefore, it is important to know if the channel has any LoS component or not. This gives us 2 degrees of freedom to control the delay spread of the channel either by loading it or by varying the K-factor. However it is important to point out that we might be able to tune the channel to give the same delay spread by both these different methods but it will have totally different effect on the bit-error-rate measurement of a modulated signal in the chamber. For the case of loading the chamber we still have no LoS component so we can expect a low received signal power as compared to the case when we have a LoS component.

For a particular system under test it is important to know how the channel would effect the signal transmission both in the time and frequency domain. To see if the channel is frequency selective or frequency flat we can measure the coherence bandwidth of the channel. Previously we studied how RMS delay spread can give us an idea if the channel exhibits narrowband or wideband fading. For a given data rate same information can be obtained from the frequency domain by studying if the channel is frequency selective or frequency flat for a given bandwidth of the transmitted signal. The coherence bandwidth is calculated by taking a complex auto-correlation of the frequency samples over a bandwidth of 20 MHz for loading 5 and 3. We defined coherence bandwidth as the frequency separation over which the normalized frequency auto-correlation function would fall down to a threshold of 0.5 and we considered the full bandwidth around the center frequency since the auto-correlation function is symmetric. For 0 and 1 loading case we had to sample at a much higher rate to have enough samples to see a decorrelation over a bandwidth of 5 MHz. We found out that the coherence bandwidth is flat over frequency range of 5 GHz so it gives us an idea of how to load the reverberation chamber to emulate a frequency selective or frequency flat channel for a system under test. We have also studied that when there is a strong LoS component the auto-correlation does not fall below 0.5, and this correlation between the samples is due to the LoS component that is always present. In such a case the coherence bandwidth gives a misleading result and we can estimate it from the RMS delay spread by using the inverse Fourier relationship between coherence bandwidth and

RMS delay spread. The constant of proportionality between them depends on the channel environment and for this case it turns out to be $k=0.45$.

To completely characterize the channel we need to know how it behaves both in time and frequency domains. Coherence time gives the second-order statistics of the channel and is used to characterize the time-varying nature of the frequency dispersiveness of the channel in the time domain. In the reverberation chamber we make the channel time-varying by rotating the stirrers. We have shown that by rotating the stirrers at different speeds we can control the coherence time of the channel. Loading the chamber gives a second degree of freedom to control the coherence time. By using different stirrer configurations the coherence time can also be tuned— this gives a third degree of freedom. We have also seen that depending on the frequency of operation, the coherence time can change. Coherence time is a measure of how fast or slow the channel changes in time, therefore, we can characterize the channel as slow or fast fading depending upon the transmitted symbol duration. If the channel coherence time is much lesser than the transmitted symbol duration, it is referred to as a fast fading channel, similarly if the symbol duration is much smaller than the channel coherence time, it is known as a slow fading channel. To characterize how fast the channel is changing in time we calculated the level crossing rate of the channel. Usually the level crossing of the channel envelope are counted in the downward direction by specifying a certain threshold. We calculated the LCR at different thresholds. The maximum LCR is found to be at a threshold of 3 dB below the normalized signal envelope. The signal envelope is normalized to its RMS value. We compared these results to theoretical curves for level crossing rate by using RMS Doppler spread as the input to the theoretical equations, which assume a Rayleigh channel and mobile wireless communication. The theoretical curves seemed to be offset by a constant factor which turned out to be 1.4. This offset was seen because the theoretical curves are based on the *maximum* Doppler spread of the channel. We used RMS Doppler instead of the *maximum* Doppler spread and attained lower values of LCR. After multiplying the RMS Doppler spread with this factor of 1.4, a close agreement was achieved. Thus, we can determine the effective *maximum* Doppler of the channel in this way too. Level crossing rate curves for different stirrers verify that it is a good measure of fading rate, since we see that for the same threshold levels the level crossing rate for configuration 3 is higher than configuration 1 and 2. Level crossing rate helps us determine the rate of fading which can be related to the speed of the stirrers in

the reverberation chamber. For mobile communication LCR is used to determine the speed of the mobile terminal.

Another important measure that characterizes the time-variations in the channel is average fade duration. Average fade duration is an important quantity that gives an average amount of time for which the signal envelope is below a certain threshold and helps us to predict the bit-error-rate of a communication link by comparing the symbol duration to average fade duration. The average fade duration is calculated for different threshold levels as used for LCR calculations. We concluded that for fast fading channels, the average fade duration is less which agrees with the theory. Configuration 3 gives lower average fade duration curves followed by configuration 2 and then 1. Since the theoretical equations for average fade duration also assume the maximum Doppler spread, the factor of 1.4 had to be multiplied. An important finding here is that the theoretical equations are derived for a mobile communication channel which assumes a classical Jakes spectrum, whereas in the chamber we have a fixed wireless communication channel which has an exponential spectrum arising due to the objects in the environment. From the experimental results we conclude that as long as the Doppler spread in the channel is the same either due to the relative motion between the transmitter or receiver or by the scatterers in the environment, the time domain second-order statistics of the channel will be the same. The shape of the Doppler spectrum only tells us if the wireless link is fixed or mobile or in other words, what kind of motion is causing the frequency dispersiveness in the channel.

Fading rate of the signal can also be characterized by the Doppler spread in the channel. If we FFT the channel transfer function $H(f, t)$ with respect to time we get access to the Doppler domain of the channel. In the reverberation chamber we Fourier transform the S_{21} with respect to the stirrer positions and map the stirrer position to time axis. This gives us a way to calculate the Doppler spread in the channel. A reasonable measure of estimating the Doppler spread is the RMS criteria which has been used in this study. In this study we found that the shape of the Doppler spectrum in the chamber is not the classical U-shape of the Jakes spectrum. In the chamber we get an exponential shaped Doppler spectrum which agrees with the spectrum shapes reported for fixed wireless communication channel. Jakes spectrum is derived for a mobile communication channel. Therefore, we would not expect that in the chamber unless the only motion in the environment is due to either the transmitter or the receiver. In the chamber the spread of the

Doppler spectrum is also a measure of the fading rate of the signal, so intuitively, it can be controlled by the speed of the stirrers. A second degree of freedom is to control the Doppler spread by loading the chamber. Different stirring configurations emulate different Doppler spreads and give a third degree of freedom to control the Doppler spread in the channel. It has also been shown that Doppler spread is a function of frequency too, which is true both in the real world and chamber.

This chapter is a comprehensive study of how to emulate a wireless channel in the chamber with desired frequency and time domain characteristics. The reverberation chamber offers repeatability and control over the wireless channel. Thus this knowledge can be used to tune the wireless channel in the chamber for testing the performance of the wireless devices. The repeatability of the chamber enables different devices to be tested in the same wireless environment. This makes reverberation chamber a potential facility for standardized testing of wireless devices and systems.

4

Channel Impairments in RC

The effects of static and dynamic multipath channels, emulated in the reverberation chamber on bit-error-rate of digitally modulated signals are studied. Algorithms have been developed to separate the system errors from the channel errors for evaluating the bit-error-rate performance of the modulated signals. Individual sources of errors have also been identified such as errors arising due to frequency selectivity of the channel and due to higher Doppler when stirrers are moved faster in the chamber. Channel impairments are studied in depth in order to develop testing procedure for wireless devices. Reverberation chamber is currently being studied as a potential facility for repeatable wireless device testing environment [28] [29].

4.1 Modulated signal measurements in NIST chamber

In order to perform modulated signal measurements an Agilent's Vector Signal Generator (E4438C ESG) and Agilent 89600 Vector Signal Analyzer were used at NIST to develop a simplex communication system. Figure (4.1) shows the measurement setup for modulated signal measurements.

A LabView program is written to control the vector signal generator, vector sig-

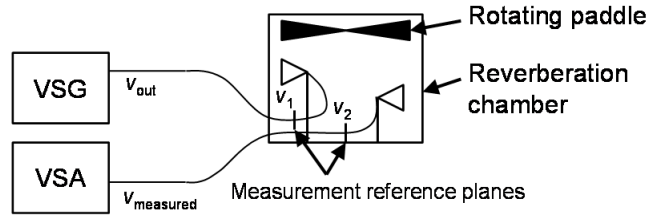


Figure 4.1: Channel Variations in time and frequency for loading 3

nal analyzer and paddles in the reverberation chamber. The VSG is used to BPSK modulate a known sequence of 2048 bits at 24.3 kbps at different power levels. Root-raised cosine pulses were generated with a roll-off ($\alpha = 0.35$), the center frequency was set to $2GHz$. This known signal is repeatedly transmitted into the chamber at different paddle position. In this experiment we use stepped paddle configuration which means that the paddles were stepped every 0.5 degree and the bit sequence was transmitted at each paddle position. Every paddle position gives a new channel realization. The bit sequence used is a pseudo-random sequence which has a white noise like properties, which helps in correcting for the delay that the signal experience in transmission through the chamber, the autocorrelation of the sequence is shown in Figure (4.2). This sequence of 2048 bits is generated by Marsenne Twister algorithm.

The VSA receives the modulated signal and demodulates the signal into stream of bits. Synchronization is done by using an external trigger which also helps to separate repetitive frames (each 2048 bit sequence is treated as a frame). In this work, BPSK modulation is studied since it requires only in-phase information and synchronization is simpler to understand so its a decent start to learn how reverberation chambers can effect modulated signals. Once the signal is demodulated by the VSA it is post processed to see if the in-phase component of the signal syn-

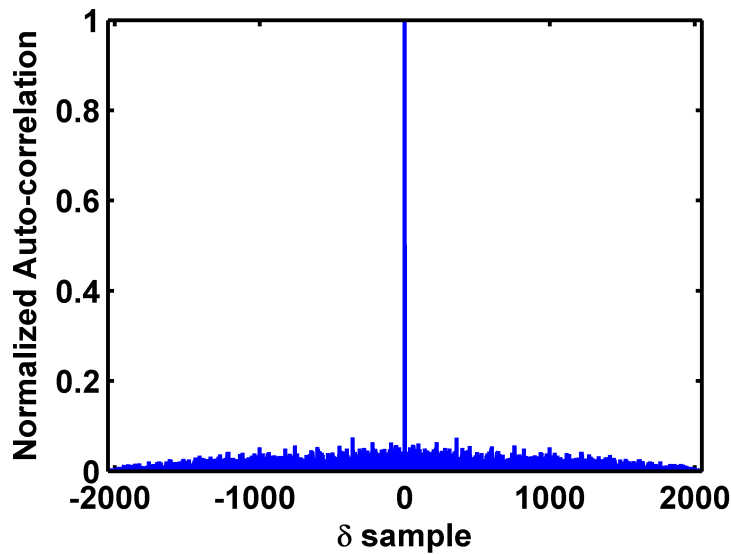


Figure 4.2: Auto-Correlation of the bit sequence

chronized with the right bit. If there is a time offset in reception of the signal and the trigger used for synchronization, then the in-phase component might align out of phase which would interpret 0 for a 1. In such a situation the whole bit sequence is flipped and it has to be taken care of in the post processing of data. It is also intelligently corrected for any system errors arising due to loss of synchronization. When a signal is in a deep fade, it is a possibility that the signal might lose phase lock and would not recover synchronization until a new trigger is sent for a new frame. This situation can result in a frame with burst of errors that would start anywhere during the frame depending upon where it experienced the deep fade and will last till the end of the frame. Similarly another situation where two deep fades would result within the transmission of a frame could result in the loss and recovery of phase synchronization, this is also taken care of in post processing, usually such a situation is experienced during continuous paddle stirring measurements which we are not dealing with in this study.

After correction it is assumed that any error in the received signal is due to the channel and no other error sources. The BPSK modulated signal at 24.3 Kbps is transmitted at different power levels for all stirrer positions and the power received in the demodulated bit stream is recorded by integrating over the power spectral density of the received signal. Bit-error-rate is a function of received power, there-

fore, for each frame the BER is calculated and plotted versus signal-to-noise ratio in the frame. This would give the BER curve for static channel conditions, it can be thought of calculating the bit-error-rate of each frame at a single time instant of a fading channel. However the transmitted signal still experiences the multipath channel and can have errors both due to multipath interference (fading) and frequency selectivity. Figure (4.3) shows BER curve for BPSK modulated data at 24.3 kbps. If we integrate the BER over the fading channel that is for all stirrer positions this would have the same effect as if the signal was transmitted through a dynamic environment. Post processing the data by taking the average power and BER over stirrer position for a certain transmit power would give a received signal that experiences a Rayleigh fading environment. This is also shown in Figure (4.3). It can be seen that for static channel measurement there is high BER for certain high SNR which shows effects due to insufficient number of bits or frames at the received power to determine the actual bit-error-rate. The average BER over the fading envelope shows a similar behavior that would be expected from a BPSK signal that experience a Rayleigh channel.

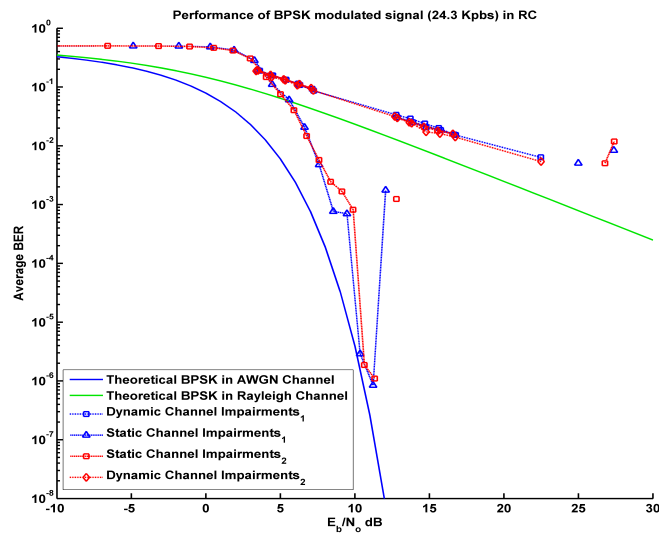


Figure 4.3: Performance of BPSK modulated signal at 24.3 kbps in static and dynamic channel environment in the reverberation chamber

4.2 Modulated signal measurements in BlueTest chamber

In order to explain the modulated signal measurements in a BlueTest chamber it would be helpful to understand the physical measurement setup. Figure (4.4) shows the measurement setup at Chalmers where we use a BlueTest chamber. This chamber has rotating platform on top of which a device under test (DUT) is mounted. It has two rectangular plate along each of the wall as shown in the figure. These plates are used to stir the fields in the chamber and are referred to as horizontal and vertical stirrer. Each stirrer move along the dimension of the wall one along the length of the chamber and other along the height. The chamber has three bow-tie wall antennas at three different walls mounted such that we have orthogonal polarization, an electronic switch is used to switch between all the antennas. In this chamber a head phantom is used for loading and this configuration is referred to as loading 1, to increase the loading a PVC cylinder filled with EM energy absorbing material is added at the corners in the chamber. Addition of every 2 cylinder increases the loading by one, example 1 head phantom and 2 cylinder configuration is known as loading 2 and so on.

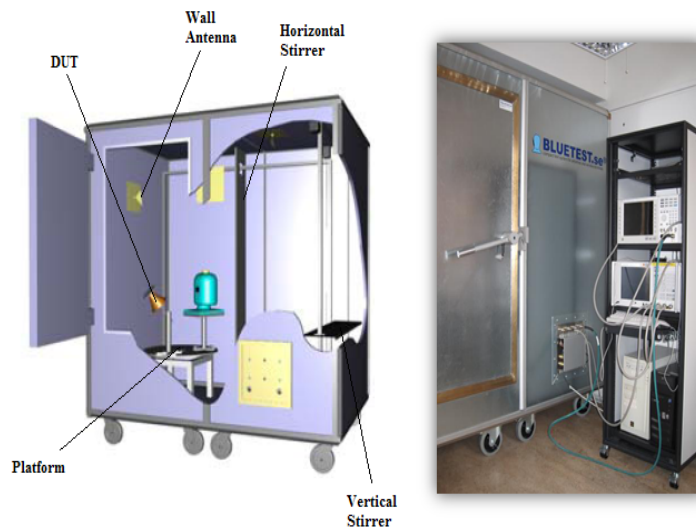


Figure 4.4: *Measurement setup at Chalmers*

Modulated signal measurements were done in a BlueTest chamber. The commercially available Bluetest software was used to control an Agilent base station

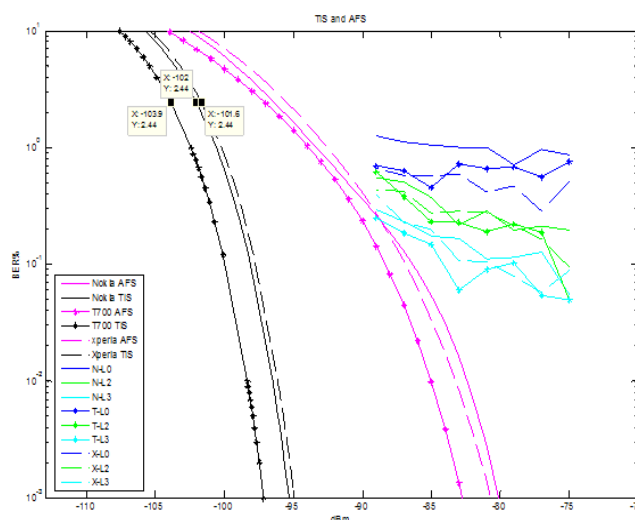


Figure 4.5: TIS and AFS measurement in BlueTest chamber

simulator (8960 Series) and measure the bit-error-rate performance of different communication systems [30]. In this study we evaluate the performance of GSM and WCDMA system under different channel conditions that can be emulated by loading the chamber or moving the stirrers with different speeds as studies above. For GSM measurements, a connection is established between the phone and the base station. A GMSK signal is then sent out to the phone at a certain transmit power, as the stirrers and platform steps. The bit-error-rate is calculated by the base station and no error correction is used. In the CTIA¹ community it is also commonly known as Total Isotopic Sensitivity (TIS) measurements. Similarly when the stirrers and platform are continuously moving during the transmission of the signal, it experiences a dynamic or Rayleigh fading environment. Such a measurements are commonly known as Average Fading Sensitivity (AFS) measurements. These performance evaluation quantities are documented in detail in [31], interested reader can refer to the document to get an insight into how these quantities are calculated and their physical significance. In Figure (4.5) the TIS and AFS measurements of three different phones are shown.

The phones used are Nokia 6120, Sony Ericsson T700 and Sony Ericsson Xpe-

¹CTIA-The Wireless Association is an international non-profit membership organization that has represented the wireless communications industry since 1984.

4.2. MODULATED SIGNAL MEASUREMENTS IN BLUETEST CHAMBER93

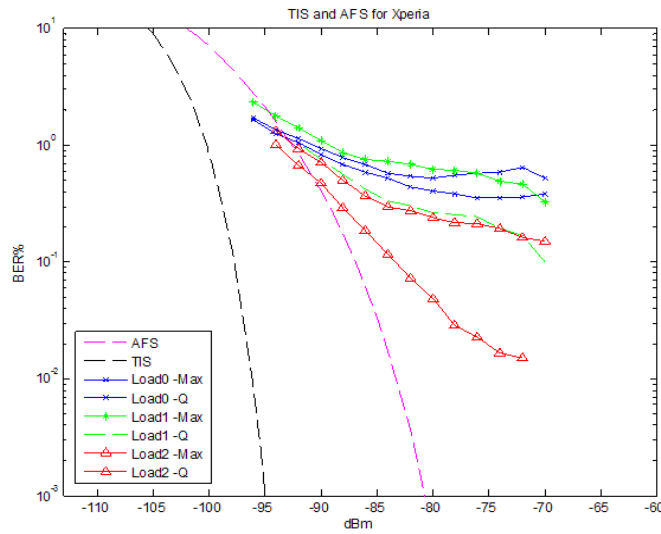


Figure 4.6: Effect of Loading and Doppler shift on BER performance of GMSK modulated signal in BlueTest chamber. 'Q' is used to indicate that stirrers are moving at quarter of the maximum speed settings

ria. In the figure above 'N' is used to abbreviate Nokia phone, 'T' is used of Sony Ericsson T700 and 'X' is used of Sony Ericsson Xperia phone respectively. The TIS curves (in black) are integrated over all stirrer and platform positions to get an average BER which results in the AFS curves from TIS measurement, these are shown in pink. However the measured AFS curves shown in blue, green and cyan for three different loading cases do not agree closely with the estimated AFS curves. It is suspected that there might be errors due to Doppler shift which comes into consideration when the stirrers and phones are moving. It is also suspected that there might be a source of error in the uplink since the phone transmit the received bits back to the base station in order to determine the bit-error-rate. This can be a topic of future research to investigate the unknown sources of errors in the BlueTest measurement techniques. It is shown in Figure (4.6) that by reducing the speed of the stirrers and platform to a quarter of the maximum speed and by increasing loading we can improve the BER performance of the system in the chamber. The improvement we see here is both due to the loading which reduces the severe fading of channel and also the Doppler shift which reduces as the stirrers now move much slower. The improvement in the slope of BER curve is most

apparent for the case of loading 2, this clearly shows how Doppler shift contribute to the errors in a GMSK modulated signal.

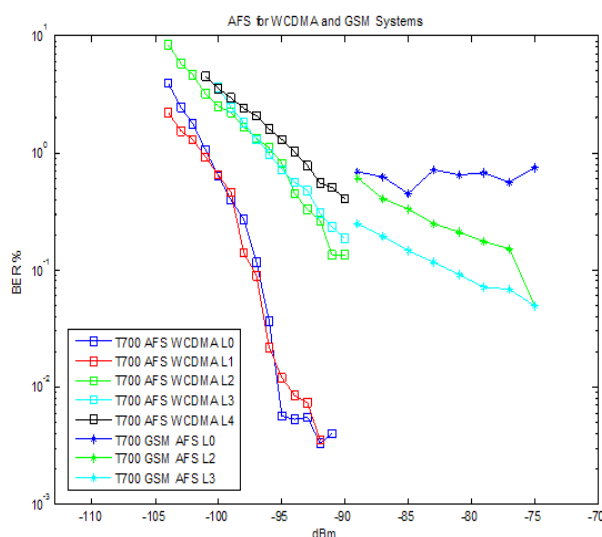


Figure 4.7: Performance of Sony Ericsson T700 in WCDMA and GSM mode, in a multipath fading environment

Performance of Wideband Code Division Multiple Access (WCDMA) system is also evaluated under fading environment. Since WCDMA system is designed to explore diversity in the multipath environment, it should perform better. For details on how the diversity is implemented, interested reader should refer to the base station application note. In Figure (4.7) the performance of a Sony Ericsson T700 phone is evaluated when used under WCDMA and GSM operation modes. As we see that the average fading sensitivity performance of a GSM system in terms on bit-error-rate gets better as we increase the loading which shows that a GSM system degrades when there is a multipath environment on the other hand the WCDMA system is designed to explore the multipath nature of the channel and it can also be seen in the figure that WCDMA performance degrades as we increase the loading. The coherence bandwidth of BlueTest chamber is estimated in [16], where it has been shown that for loading 2, the coherence bandwidth of the channel in the chamber exceeds 5 MHz which is the operating bandwidth of the WCDMA system. As the coherence bandwidth exceeds the operating bandwidth of the WCDMA system it does not explore any diversity inherent in the multipath

channel, therefore, the performance degrades with increasing loading unlike GSM system. Thus a reverberation chamber can potentially be used as a facility for wireless device testing in a multipath environment. By tuning the chamber it can exhibit various desired wireless channel characteristics. In this thesis work the effort has been geared towards understanding how to use the NIST reverberation chamber for wireless device measurements.

4.3 Conclusion

In this chapter we studied the performance of a BPSK modulated signal in a multipath environment. The modulated signal was transmitted at different power levels such that we can receive signals at various power levels as we step through the stirrers. Since the received power is a function of multipath interference and chamber characteristics, we used an unloaded reverberation chamber at NIST to avoid any power losses due to absorbers. Our aim was to study the channel impairments; therefore, we did not use any error correction code. The algorithm for estimating the bit-error-rate of the received signal corrected for any errors that could have arisen due to the measurement setup such that we would only get the errors due to the channel itself. We processed the received signal for different received powers by binning them and plotted their respective bit-error-rate, this kind of measurement is typically recognized as Total Isotropic Sensitivity measurement by the CTIA community. If we process the same data by averaging the received power over stirrer positions and plot it versus the average bit-error-rate, the result should be comparable to the theoretical BPSK curve for a Rayleigh channel. Averaging over stirrer positions is equivalent to the case where the stirrers are constantly moving and the bit-error-rate is calculated at the receiver. Because the measurement was done in a static environment, averaging over stirrer positions does not account for any errors that would arise due to Doppler shift. These curves shown in Figure (4.3) indicates that modulated signals behave much the same in the chamber as they would in a real multipath environment. We used an unloaded chamber, which is not comparable to real life indoor environment in terms of delay spread and coherence bandwidth. A more comparable result can be achieved by doing the same measurement for an indoor environment and then repeating it in the chamber by tuning the chamber to exhibit similar wireless channel characteristics. These results would definitely be of interest and hopefully would agree closely.

Another interesting measurement would be testing an off-the-shelf wireless LAN router which can support MIMO and exploits the spatial diversity in the multipath environment. To comparison of throughput performance in an office corridor and a reverberation chamber tuned to exhibit the same power delay profile and coherence time would demonstrate the reverberation chamber's capability as a wireless channel emulator.

System level performance is also of interest to many vendors. Currently there is no standard or comparable test to tell if mobile phone 'A' performs better than mobile phone 'B' on a system level in terms of bit-error-rate performance. One such experiment has been performed at Chalmers by testing three different phones by Nokia and Sony Ericsson. We tested the performance of these phone in a GSM system and clearly showed that all these phones showed better bit-error-rate performance in a weak multipath environment. However when the chamber was unloaded and there was a strong multipath environment the performance of these phones decreased.

These phones can work with 3G systems which mean they can be tested for WCDMA system. We tested the average fading sensitivity performance of all the three phones in the Bluetest chamber in WCDMA mode. Since WCDMA systems can exploit frequency diversity in a multipath environment they tend to perform better. This is exactly what the measurement results confirmed. For higher loading cases the WCDMA performance tend to get worst as the coherence bandwidth became greater than the system bandwidth.

5

Summary

The main topic of this thesis work was to emulate and characterize a wireless channel in the reverberation chamber. The chamber was also tested as a channel emulator by evaluating the bit-error-rate performance of the modulated signals transmitted through it. Chapter 1 gave a very brief introduction about reverberation chambers and their utility as a wireless channel emulator that has been the new area of research.

Chapter 2 studies the EM field distribution in the chamber which told us how the ‘wireless channel’ would behave. We studied the Rician K-factor in the channel, which is an important parameter to characterize it. Maximum likelihood estimation method based on amplitude statistics of the channel was studied, which complement the direct measurement method of the K-factor from the S_{21} data. Usually in outdoor propagation measurements, we only have the amplitude information of the channel. Therefore, a method that can determine the K-factor from only amplitude information is useful to study the channel. It was found that if the fields in the chamber were not stirred effectively, the K-factor was high. A strong LoS component was also observed in the data when the antennas were pointing towards each other and were co-polarized. To make sure we have a purely

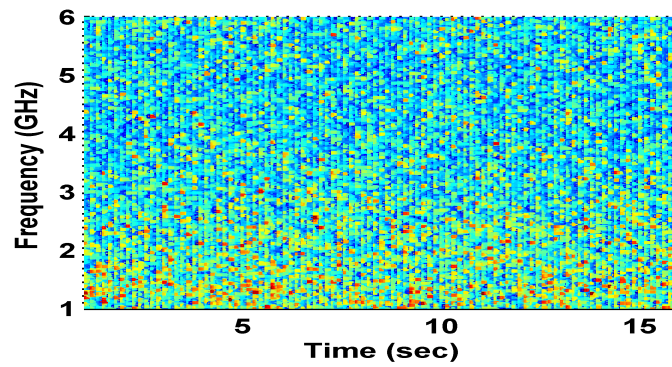
Rayleigh channel in the chamber, the antennas were adjusted such that they were cross-polarized and facing towards the stirrers in the chamber. This arrangement guaranteed a well stirred EM fields in the chamber and thus a low K-factor.

In Chapter 3 we focused on how to characterize a wireless channel in the reverberation chamber. We performed several experiments to study the power delay profile, coherence bandwidth, coherence time and Doppler spread of the channel. These parameters characterize the channel completely in both the time and frequency domain. We concluded that the RMS delay spread in the chamber is a function of loading, antenna configuration and frequency. The power delay profile in the reverberation chamber is exponential, therefore, the mean delay spread and RMS delay spread are expected to be the same. To process the data correctly we had to get rid of the chamber charge up time samples and only process the exponential power decay sample. It was also concluded that aliasing can be an issue when inverse Fourier transforming the frequency domain data. A simple way to know if we had aliasing in the data was to look at the mean and RMS delay spread: if both converge to approximately the same value then there is no aliasing. Being Fourier transform pairs, coherence bandwidth and RMS delay spread are inversely related to each other. Coherence bandwidths were estimated, and it was found to be constant over a wide band in the chamber. This gives us an idea if a signal of a particular bandwidth would experience flat or frequency selective fading. Coherence bandwidth is a function of loading in the reverberation chamber. For zero loading we saw some frequency dependence due to high antenna losses at low frequencies and high wall losses at high frequencies. This dependence goes away as we loaded the chamber since absorber losses dominated. Time variations of the signal are better understood by looking at the coherence time and Doppler spread of the channel. We discussed that the coherence time and Doppler spread are both functions of stirrer speeds, configuration, loading and frequency of operation. Coherence time and Doppler spread are Fourier transform pairs and are inversely related to each other. We found out that the coherence time in the chamber can only emulate slow fading channels for the data rates that are typically used in any commercial wireless system. Similarly the Doppler spread measured in the chamber is very low and comparable to Doppler spread experienced by a mobile terminal walking speed. To study the time variations of the channel we looked into the level crossing rate and average fade duration of the channel. LCR gives an idea of how quickly the channel changes during a symbol transmission and average fade duration gives an

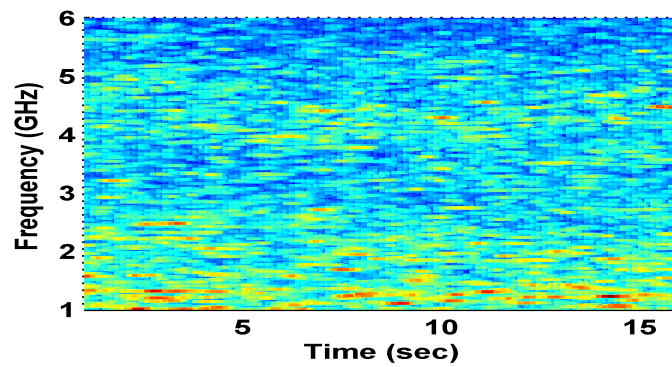
idea of how to design error correction codes and the time for which a symbol(s) would be in a fade. A important finding was that the shape of the Doppler spectrum is an exponential which is typical for fixed wireless communication channels. The shape of the Doppler spectrum only tells what kind of motion is causing the variations in the channel. Another important finding is that for fixed wireless channels and mobile channels the time domain, first and second order characteristics are the same and they agree closely in LCR and AFD measures. In the chamber we can control all of these parameter to emulate a wireless channel that has the exact same characteristics as that of a particular real world wireless channel. When a device operates in such an emulated channel, we can argue that it will behave the same as it were operating in a real world channel. It is a topic of interest to research if we can emulate a mobile wireless channel in the reverberation chamber. Some researchers have shown that by using a fading simulator with the reverberation chamber it is possible to emulate a channel that has two independent realizations. One from the fading simulator itself and one from the chamber. Thus, the convolution of these two independent complex Gaussian processes result in a double Rayleigh channel. It is believed that the performance of a wireless device in a double Rayleigh channel will be poorer. It is of interest to emulate a double Rayleigh channel and study its characteristics. Wireless devices performance in such a channel is also of interest and can be continuation of this research.

In the reverberation chamber we have the freedom to choose from a number of parameters that can be used to control the channel characteristics. Loading as well as stirrer configuration and speed can be changed to control both Doppler spread and coherence time of the channel. Similarly RMS delay spread and coherence bandwidth can be controlled by changing the loading and Rician K-factor. Figure (5.1) summarizes how the channel gain in time and frequency changes as the loading is changed in the chamber.

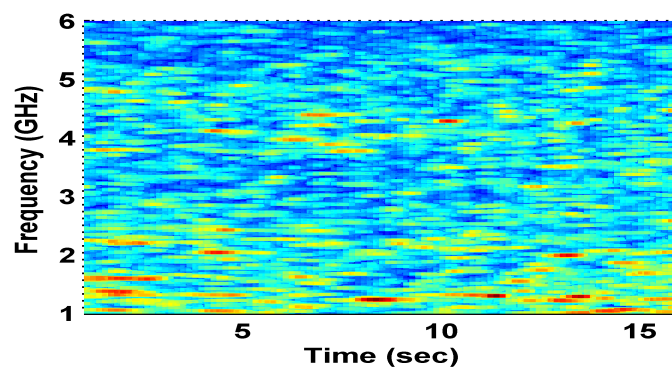
For no loading it shows that the channel changes fast both in time and frequency. In the frequency domain it is because of the multipath components arriving at different delays at the receiver, which introduces frequency selectivity in the channel or time distortion. It should be emphasized that when we talk about a channel being frequency flat or frequency selective, it depends on the bandwidth of the signal being transmitted through the channel. In the time domain, the channel changes faster with higher Doppler. Typically Doppler is related to the speed of the Tx or Rx relative to each other and indicates how fast the Tx or Rx would pass



(a) Channel Variations in time and frequency for loading 0



(b) Channel Variations in time and frequency for loading 3



(c) Channel Variations in time and frequency for loading 5

Figure 5.1: Channel Gain as a function of Loading

through a static environment's spatial electromagnetic interference pattern. The

R_x would see time variations much faster when moving at higher speeds, so ultimately coherence time is related to fading rate. For fixed wireless communication this change in the interference pattern of the EM waves is a result of motion of objects in the environment. A fast moving object would be very effective at disturbing the electromagnetic interference pattern, especially at high frequencies. In the chamber, loading reduces the number of effective multipath components. This introduces some correlation in the fading envelope because the stirrers must move quite a bit more in order to completely change the electromagnetic pattern at the receiver arising due to the phasor addition of the multipath component.

Chapter 4 studies GSM and WCDMA system performance in a reverberation chamber. From the bit-error-rate performance it is obvious that the GSM system does not perform well in a strong multipath environment since it sees a harsh fading environment in a strong multipath component whereas WCDMA systems exploits frequency diversity and perform better in a multipath environment. It was observed that GSM system performance improved with higher loading whereas, the WCDMA performed better when there was no loading and performance degrades as the loading increased. The performance of these systems show the utility of the chamber as a repeatable wireless channel emulator. It is of interest to measure the throughput of a wireless system, possibly a WLAN router in an office corridor environment and an emulated wireless channel with same delay spread and coherence time in the chamber. A comparison between the two measurements is expected to agree closely and would demonstrate the chamber's utility as channel emulator for wireless device performance testing.

Part II

Appendices



Characterization of a Wireless Channel

A.1 Characterization of Wireless Channel

Reverberation chamber is a highly reflective environment. Since there is no significant path loss or any shadowing in the chamber, these effects are not taken into account in the study of wireless channel in the chamber. Reverberation chamber emulates a purely small scale fading environment which owes to constructive and destructive interference of the multipath component introduced by the channel in the chamber. Small scale fading or simply fading, is used to describe rapid fluctuations of the amplitudes, phases, or multipath delays of the radio signal over a short period of time or travel so that large scale; path loss and shadowing effects may be ignored. However this channel can be a flat fading channel or a frequency selective channel depending upon the transmitted symbol duration. In this appendix a statistical characterization of such a channel is summarized, for details see [7, 14].

If a single pulse is transmitted over a multipath channel then the received signal will appear as a pulse train, with each pulse in the train corresponding to a LoS component or a distinct multipath component associated with a distinct scatterer or a cluster of scatterer. The time delay spread of the channel can result in sig-

nificant distortion of the received signal. This delay spread equals the time delay between the arrival of the first received signal component associated with a single transmitted pulse. If the delay spread is small compared to the inverse of the signal bandwidth, there is a little time spreading in the received signal, A.K.A narrow band fading in the frequency domain or flat fading. However if the delay spread is relatively large then there is significant time spreading of the received signal, which can lead to substantial signal distortion. Another characteristic of the multipath channel is its time-varying nature. This time variation arises because of the motion of either the transmitter, the receiver or the scatterers in the environment or all of these together, which gives rise to multipath that will change over time. If we repeatedly transmit pulses from a moving transmitter we will observe changes in the amplitude, delays and number of multipath component corresponding to each pulse, these changes occur over a much larger time scale than the fading due to constructive and destructive addition of multipath component associated with a fixed set of scatterers.

A.2 Time-Varying Channel Impulse Response

A time varying impulse response can be mathematically modelled by considering a transmitted signal given by,

$$s(t) = Re \left\{ u(t) \exp^{j2\pi f_c t} \right\} \quad (\text{A.1})$$

where $u(t)$ is the equivalent low pass signal for $s(t)$ with bandwidth B_u and f_c is its carrier frequency. The corresponding received signal is the sum of the line-of-sight path and all resolvable multipath, neglecting noise. The received signal can then be written as,

$$r(t) = Re \left\{ \sum_{n=0}^{N(t)} \alpha_n(t) u(t - \tau_n(t)) \exp^{j(2\pi f_c(t - \tau_n(t)) + \phi_{D_n})} \right\} \quad (\text{A.2})$$

where $n=0$ corresponds to the LoS path, The unknown in (A.2) are the number of resolvable multipath components $N(t)$, the path length $r_n(t)$ and its corresponding delay $\tau_n(t) = r_n(t)/c$, Doppler phase shift $\phi_{D_n}(t)$ and amplitude $\alpha_n(t)$.

Two multipath component are *resolvable* if their delay difference significantly exceeds the inverse signal bandwidth, i.e. $|\tau_1 - \tau_2| \gg B_u^{-1}$. Multipath component that do not satisfy this criteria cannot be separated out at the receiver because $u(t - \tau_1) \approx u(t - \tau_2)$ and thus these components are *non resolvable*. The non resolvable components are combined into a single multipath component with delay $\tau \approx \tau_1 \approx \tau_2$ and an amplitude and phase corresponding to the sum of the different components. The amplitude of such a signal will typically undergo fast variations due to constructive and destructive combining of non resolvable multipath components. In general wideband channels have resolvable multipath components and narrowband channel have non resolvable multipath components contributing to each term in (A.2). The parameters $\tau_n(t)$, $\alpha_n(t)$ and $\phi_{D_n}(t)$ associated with each resolvable multipath component changes over time and are characterized as a random process that is assumed to be both stationary and ergodic.

A.3 Narrowband Fading Model

If the delay spread T_m of the channel is small compared to the inverse signal bandwidth B of the transmitted signal; that is, $T_m \ll B^{-1}$. The delay spread T_m of the channel is usually characterized by the RMS delay spread. $T_m \ll B^{-1}$ implies that $u(t - \tau_i) \approx u(t)$ for all i and thus (A.2) can be rewritten as,

$$r(t) = Re \left\{ u(t) \exp^{j(2\pi f_c t)} \left(\sum_{n=0}^{N(t)} \alpha_n(t) \exp^{-j\phi_n} \right) \right\} \quad (\text{A.3})$$

Equation (A.3) differs from (A.2) by the complex scale factor in the large parentheses. This scale factor is independent of the transmitted signal $s(t)$ and in particular of the low pass signal $u(t)$ as long as the narrowband assumption is satisfied then there is no signal distortion. To characterize scale factor we can assume a signal $s(t)$ given as,

$$s(t) = Re \left\{ \exp^{j(2\pi f_c t + \phi_o)} \right\} = \cos(2\pi f_c t + \phi_o) \quad (\text{A.4})$$

which is narrowband for any T_m . Now the received signal can be written in terms of in-phase and quadrature components as,

$$r(t) = r_I(t)\cos(2\pi f_c t) + r_Q\sin(2\pi f_c t) \quad (\text{A.5})$$

where the in-phase and quadrature components are given as,

$$r_I = \sum_{n=0}^{N(t)} \alpha_n(t)\cos(\phi_n(t)) \quad r_Q = \sum_{n=0}^{N(t)} \alpha_n(t)\sin(\phi_n(t)) \quad (\text{A.6})$$

for,

$$\phi_n(t) = 2\pi f_c \tau_n(t) - \phi_{D_n} - \phi_o \quad (\text{A.7})$$

where,

$$\phi_{D_n} = \int_t 2\pi f_{D_n} t dt \quad (\text{A.8})$$

If $N(t)$ is large then in-phase and quadrature signal components are jointly Gaussian and the amplitude is Rayleigh. Such a process or received signal can be completely characterized by its Mean, Autocorrelation and Cross-correlation. If it is assumed that $\phi_n(t)$ is uniformly distributed on $[-\pi, \pi]$. Thus $E[r_I(t)] = E[r_Q(t)] = 0$, which implies $E[r(t)] = 0$. Thus the received signal is a zero-mean Gaussian process given that there is no dominant LoS component. If there is a LoS component then the phase of the received signal is dominated by the phase of the LoS component. The Auto-correlation of the in-phase and quadrature component is given by (A.9).

$$A_r = \mathbf{E}[r(t)r(t+\tau)] = A_{r_I}(\tau)\cos(2\pi f_c \tau) + A_{r_I, r_Q}(\tau)\sin(2\pi f_c \tau) \quad (\text{A.9})$$

where,

$$\begin{aligned} A_{r_I, r_Q} r(t, t+\tau) &= A_{r_I, r_Q}(\tau) \\ &= -0.5 \sum_n \mathbf{E}[\alpha_n^2] \sin\left(2\pi v \tau \cos\frac{\theta_n}{\lambda}\right) \\ &= \mathbf{E}[r_Q(t)r_I(t+\tau)] \end{aligned} \quad (\text{A.10})$$

If we further assume uniform scattering environment introduced by Clarke [32] where N multipath component with angle of arrival $\theta_n = n\Delta\theta$ which give $\Delta\theta = 2\pi/N$ and that each multipath component has the same received power, $\mathbf{E}[\alpha_n^2] = 2P_r/N$. Now if we assume that the number of scatterers grows to infinity, which correspond to uniform scattering from all directions. Then $N \rightarrow \infty$, $\Delta\theta \rightarrow 0$. Then Autocorrelation of the in-phase and cross correlation of in-phase and quadrature components in (A.9) are given as,

$$A_{r_I}(\tau) = P_r J_0(2\pi f_D \tau), \quad J_0(x) = \frac{1}{\pi} \int_0^\pi \exp^{-jx \cos\theta} d\theta \quad (\text{A.11})$$

$J_0(x)$ is the Bessel function of zeroth order, similarly for the uniform scattering environment

$$A_{r_I, r_Q}(\tau) = 0. \quad (\text{A.12})$$

A.3.1 Envelope and Power Distribution

For any two independent Gaussian distributed random variable X and Y with zero mean $\mu = 0$ and equal variance σ^2 , it can be shown that $Z = \sqrt{X^2 + Y^2}$ is Rayleigh distributed and Z^2 is exponentially distributed. In Appendix A.3 it is discussed that when $\phi_n(t)$ is uniformly distributed then r_I and r_Q are both zero mean Gaussian random variables, if we assume the variance of σ^2 of both the in-phase and quadrature components, the the signal envelope can be given as,

$$z(t) = |r(t)| = \sqrt{r_I^2(t) + r_Q^2(t)} \quad (\text{A.13})$$

which is Rayleigh distributed with distribution give as,

$$P_z(z) = \frac{z}{\sigma^2} \exp\left[-\frac{z^2}{2\sigma^2}\right], \quad z \geq 0. \quad (\text{A.14})$$

by making a change of variables $z^2(t) = |r(t)|^2$ in (A.14), the power distribution can be obtained and given as,

$$p_{z^2}(x) = \frac{1}{2\sigma^2} \exp^{-\frac{x}{2\sigma^2}}, \quad x \geq 0. \quad (\text{A.15})$$

Thus the received signal power is exponentially distributed with mean $2\sigma^2$, which is the powers in the signal based on path loss and shadowing alone. If the channel has a LoS component then $r_I(t)$ and $r_Q(t)$ are not zero mean variables as shown in Section 2 for measured data. The signal envelop in this case can be shown to have a Rician distribution given by

$$Pz(z) = \frac{z}{\sigma^2} \exp\left[\frac{-(z^2 + s^2)}{2\sigma^2}\right] I_0\left(\frac{zs}{\sigma^2}\right), \quad z \geq 0. \quad (\text{A.16})$$

where $2\sigma^2$ is the average power in the multipath components and A^2 is the power in the LoS component, I_0 is the modified Bessel function of zeroth order. The Rician distribution is often described in terms of a fading parameter K , defined by

$$K = \frac{A^2}{2\sigma^2} \quad (\text{A.17})$$

Thus, K is the ratio of power in the LoS component to the power in the other multipath components. $K = 0$ gives Rayleigh fading and for $K = \infty$ we have no fading (i.e. a channel with no multipath and only a LoS component).

A.3.2 Level Crossing Rate and Average Fade Duration

$$L_z = \sqrt{2\pi} f_D \rho e^{-\rho^2} \quad (\text{A.18})$$

where $\rho = Z/\sqrt{\overline{P_r}}$ and $\sqrt{\overline{P_r}}$ is the average envelope level. Average fade duration is defined as the average time the signal envelope stay below a target level Z . This target level is usually determined by the system performance metric such as BER. Average fade duration also helps to design the error control codes. For Rayleigh distribution it is given as,

$$\bar{t}_z = \frac{e^{\rho^2} - 1}{\rho f_D \sqrt{2\pi}} \quad (\text{A.19})$$

It can be seen from (A.18) and (A.19) that both Level crossing rate and Average fade duration are a function of the speed of the terminal or surrounding object or both such that they introduce a Doppler shift (f_D) in the received signal.

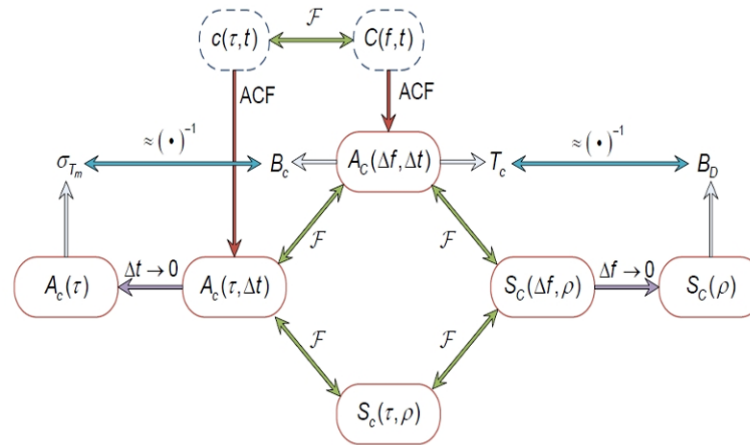
A.4 Wideband Fading Model

If the multipath delay spread $T_m \gg T$, where T is the transmitted pulse duration, then the signal is not narrowband and we get another form of distortion due to the multipath delay spread. Each other multipath can be resolved, however these multi path interfere with subsequently transmitted pulses. This effect is called *inter-symbol interference* (ISI). The wideband fading differs from narrow band fading in terms of the resolution of different multipath components. Specifically for different narrow band signal, multi path component have a time resolution less than the inverse signal bandwidth, so the multi path component combine at the receiver to yield original transmitted signal with amplitude and phase characterized by random processes. These random processes are in turn characterized by their autocorrelation (or PSD) or instantaneous distribution as discussed in Appendix A.3. The difference between wideband and narrowband fading model is that, as the transmit signal bandwidth B increases so that $T_m \approx B^{-1}$, the approximation $u(t - \tau_n(t)) \approx u(t)$ is no longer valid. The received signal is then the sum of all the copies of the original signal, where each copy is delayed in time by τ_n and shifted in phase by $\phi_n(t)$. The signal copies will combine destructively when their phase term differ significantly and will distort the direct signal when $u(t - \tau_n)$ differs from $u(t)$. If the number of multipath component are large enough and the phase of each component is uniformly distributed then the received signal will be zero-mean complex Gaussian process with Rayleigh distributed envelope. However, wide band fading differs from narrowband fading in terms of the resolution of the multipath components. For characterizing wide band channels we define the *scattering function* for random channels as the Fourier transform of $A_c(\tau, \Delta t)$ with respect to the parameter Δt , where $A_c(\tau, \Delta t)$ is the autocorrelation function of the channel impulse response $c(t, \tau)$ and is given as,

$$S_c(\tau, \rho) = \int_{-\infty}^{\infty} A_c(\tau, \Delta t) e^{-j2\pi\rho\Delta t} d\Delta t \quad (\text{A.20})$$

The scattering function characterizes the average output power associated with the channel as a function of multipath delay τ and frequency parameter ρ , known as Doppler. The most important characteristics of the wideband channel are the coherence bandwidth, power delay profile, coherence time and Doppler power spectrum which are all derived from the scattering function $S_c(\tau, \rho)$. The characteristics are

briefly discussed here in the following sub sections for more details see [14] and the Fourier relationship between these characteristics are beautifully put together in Figure (A.1). A typical scattering function in the reverberation chamber is shown in Figure (A.2). In the reverberation chamber the Power delay profile exhibits an exponential decay and the Doppler spectrum shows a spike in the center (at the carrier frequency) and decays off exponentially, which is typical for fixed wireless communication.



- The “big picture” for WSS-US reveals how coherence time and bandwidth relates to power delay profile and Doppler spectrum
- The RMS delay spread indicates how much ISI is expected

Figure A.1: Big Picture of the WSS Uncorrelated Scattering from Erik Strom lecture slides in the course of Wireless Communication at Chalmers University

A.4.1 Power Delay Profile

The power delay profile is defined as the autocorrelation $A_c(\tau, \Delta t)$ with $\Delta t = 0$: $A_c(\tau) \triangleq A_c(\tau, 0)$. The power delay profile represent the average power associated with a given multipath component and can be easily measured empirically. It is also known as the *multipath intensity profile*. The average and RMS delay spread are typically defined in terms of the power delay $A_c(\tau)$ as,

$$\mu_{T_m} = \frac{\int_0^\infty \tau A_c(\tau) d\tau}{\int_0^\infty A_c(\tau) d\tau}, \quad (\text{A.21})$$

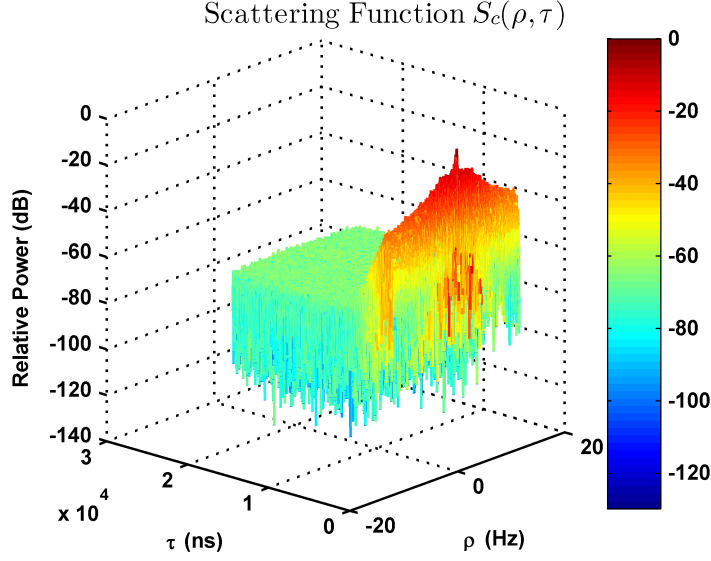


Figure A.2: Typical scattering function in the Reverberation Chamber

and

$$\sigma_{T_m} = \sqrt{\frac{\int_0^\infty (\tau - \mu_{T_m})^2 A_c(\tau) d\tau}{\int_0^\infty A_c(\tau) d\tau}} \quad (\text{A.22})$$

Although $\mu_{T_m} \approx \sigma_{T_m}$ in many channels with large number of scatterers, the exact relationship between them depends on the shape of $A_c(\tau)$. The time delay T where $A_c(\tau) \approx 0$ for $\tau \geq T$ can be used roughly to characterize the delay spread of the channel. It is typically assumed that the synchronizer locks to the multipath component at approximately the mean delay, in which case the RMS delay spread characterizes the time spreading of the channel.

A.4.2 Coherence Bandwidth

Time varying multipath channel can also be characterized in the frequency domain if we take the Fourier transform of the low pass time varying channel impulse response $c(\tau, t)$ with respect to τ . Specifically, define the random process as,

$$C(f; t) = \int_{-\infty}^{\infty} c(\tau; t) e^{-j2\pi f\tau} d\tau \quad (\text{A.23})$$

then the autocorrelation of the transfer function $C(f; t)$ can be written as $A_c(\Delta f, \Delta t)$. If we define $A_c(\Delta f) = (\text{check here for trieq sign})A_c(\Delta f; 0)$ then,

$$A_c(\Delta f) = \int_{-\infty}^{\infty} A_c \tau e^{-j2\pi\Delta f \tau} d\tau. \quad (\text{A.24})$$

Thus $A_c(\Delta f)$ is the Fourier transform of the power delay profile. Since $A_c(\Delta f)$ is an autocorrelation, it follows that the channel impulse response is approximately independent at the frequency separation Δf where $A_c(\Delta f) \approx 0$. The frequency B_c where $A_c(\Delta f) \approx 0$ for all $\Delta f > B_c$ is called the *coherence bandwidth* of the channel. By Fourier transform relationship, the minimum frequency separation B_c for which the channel response is roughly independent is $B_c \approx 1/T$, where T is typically taken to be the RMS delay spread σ . A more general approximation is $B_c \approx k/\sigma_{T_m}$, where k depends on the shape of $A_c(\tau)$ and the precise specification of coherence bandwidth.

A.4.3 Coherence Time

Usually the time variation in the channel arises due to transmitter or receiver motion and some time due to the motion of the object in the environment. Since the motion of the objects in the environment is usually very slow compared to the speed of a mobile receiver or transmitter such that it does not affect the transmitted signal in terms of Doppler shift as much compared to the Doppler shifts introduced by the mobile transmitter or receiver, however if the motion is only due to the objects in the environment or channel then the Doppler effect due to such motion should be prominent though it would generally be very small or negligible as it is due to relatively slow moving objects. The Doppler effect which occurs due to time variations in the channel can be characterized by taking the Fourier transform of $A_c(\Delta f; \Delta t)$ relative to Δt .

$$S_c(\Delta f; \rho) = \int_{-\infty}^{\infty} A_c(\Delta f; \Delta t) e^{-j2\pi\rho\Delta t} d\Delta t. \quad (\text{A.25})$$

To characterize Doppler at a single frequency, Δf is set to zero and then define $S_c(\rho) \triangleq S_c(0, \rho)$, then

$$S_c(\rho) = \int_{-\infty}^{\infty} A_c(\Delta t) e^{-j2\pi\rho\Delta t} d\Delta t. \quad (\text{A.26})$$

In the equation above $A_c(\Delta t)$ is an autocorrelation function which tells how the channel impulse response decorrelates over time. The function $A_c(\Delta t = T) = 0$ indicates that the channel impulse responses observed at time separated by T are uncorrelated and therefore independent since a channel is a random Gaussian process. The *coherence time* T_c of the channel is defined as the range of Δt values over which $A_c(\Delta t)$ is approximately non-zero. Thus the time varying channel decorrelates after approximately T_c seconds.

A.4.4 Doppler Spread

The function $S_c(\rho)$ defined in (A.26) is called the the Doppler power spectrum of the channel, Since it is the Fourier transform of the autocorrelation it gives the power spectral density of the received signal as a function of frequency parameter *Doppler* ρ . The maximum ρ -value for which $|S_c(\rho)|$ is greater than zero is called the *Doppler spread* of the channel, denoted by B_D . By Fourier relation between $A_c(\Delta t)$ and $S_c(\rho)$, we have $B_D \approx 1/T_c$. In general $B_D \approx k/T_c$, where k depends on the shape of $S_c(\rho)$.

B

Fourier Theory

B.1 Frequency Sampling

The theory behind frequency domain sampling is briefly discussed as under to clarify the concept of measuring the time domain impulse response from the spectrum or frequency domain data. This problem is mathematically the dual of sampling a signal in the time domain. If we sample the frequency domain signal or spectrum every δF then if $x(t)$ denotes the discrete time domain signal, the spectrum is,

$$X[k\delta F] = \int_{-\infty}^{\infty} x(t)e^{-j2\pi k\delta F t} dt \quad (\text{B.1})$$

If we define the reciprocal of δF as $\tau_{max} = 1/\delta F$, the the above expression can be written as,

$$X[k\delta F] = \int_{-\infty}^{\infty} x(t)e^{-j2\pi kt/\tau_{max}} dt \quad (\text{B.2})$$

The integration range of the integral can be sub divided into an infinite number of intervals of width τ_{max} and change the variable of integration to translate each integral into fundamental range $-\tau_{max}/2 \leq t \leq \tau_{max}/2$.

$$X[k\delta F] = \int_{-\tau_{max}/2}^{\tau_{max}/2} \left[\sum_{-\infty}^{\infty} x(t - n\tau_{max}) \right] e^{-j2\pi kt/\tau_{max}} dt \quad (\text{B.3})$$

The signal inside the bracket is periodic with fundamental period $1/\delta F$. Let us denote it as $x_p(t)$.

$$x_p(t) = \sum_{-\infty}^{\infty} x(t - n\tau_{max}) \quad (\text{B.4})$$

Since this signal is periodic we can expand it into a Fourier Series representation.

$$x_p(t) = \sum_{-\infty}^{\infty} c_k e^{j2\pi kt/\tau_{max}} = \sum_{-\infty}^{\infty} c_k e^{j2\pi k\delta F t} \quad (\text{B.5})$$

hence,

$$c_k = 1/\tau_{max} \int_{-\tau_{max}/2}^{\tau_{max}/2} x_p(t) e^{-j2\pi k\delta F t} dt \quad (\text{B.6})$$

comparing (B.6) to (B.3)

$$c_k = 1/\tau_{max} X(k\delta F) \quad (\text{B.7})$$

$$c_k = \delta F X(k\delta F) \quad (\text{B.8})$$

We can conclude from (B.8) that the samples of the spectrum $X(F)$ correspond to the Fourier coefficients of a periodic signal $x_p(t)$ with period $\tau_{max} = 1/\delta F$.

If the signal $x(t)$ is time limited to τ seconds and τ_{max} is selected such that $\tau_{max} > 2\tau$ there will be no aliasing, see Figure (B.1).

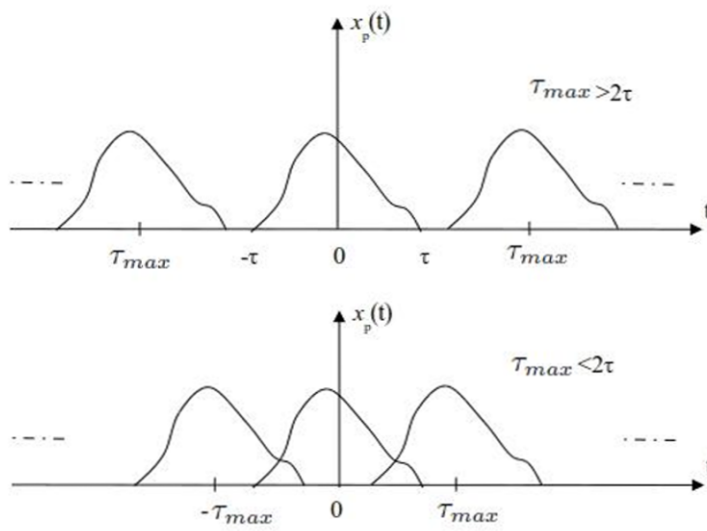


Figure B.1: (a) Time domain signal with no aliasing (b) Time domain signal with aliasing

C

Electromagnetic Theory of RC

C.1 Quality Factor of the Reverberation Chamber

The Q of a cavity is a key quantity in calculating both shielding effectiveness of the surrounding shield and the time constant of the cavity. In general, the cavity will have apertures and will contain lossy objects and at least one receiving antenna. The definition for Q is,

$$Q = \omega U_s / P_d \quad (\text{C.1})$$

where ω is the excitation (angular) frequency, U_s is the steady state energy in the cavity and P_d is the dissipated power. In our application the cavity is excited by an exterior field incident on apertures, but the Q theory does not depend on the excitation method. Thus this theory is also applicable to reverberation chambers excited by antennas. The dissipated power can be written as sum of four terms.

$$P_d = P_{d1} + P_{d2} + P_{d3} + P_{d4} \quad (\text{C.2})$$

Where P_{d1} is the power dissipated in the cavity walls, P_{d2} is the power absorbed in the loading objects within the cavity, P_{d3} is the power lost through aperture leakage and P_{d4} is the power dissipated in the loads of receiving antennas. From (C.1) and (C.2) we can write an expression for the inverse of Q.

$$Q^{-1} = Q_1^{-1} + Q_2^{-1} + Q_3^{-1} + Q_4^{-1} \quad (C.3)$$

where,

$$Q_1 = \frac{\omega U_s}{P_{d1}}, Q_2 = \frac{\omega U_s}{P_{d2}}, Q_3 = \frac{\omega U_s}{P_{d3}} \text{ and } Q_4 = \frac{\omega U_s}{P_{d4}} \quad (C.4)$$

The smallest of Q1, Q2, Q3 and Q4 will be dominant contributor to Q. Individual loss mechanism are studied in [3]. Here we only give the final equations for each loss mechanism.

$$\text{Wall Losses } Q_1 = \frac{3V}{2\mu_r S \delta} \quad (C.5)$$

$$\text{Absorption Losses } Q_2 = \frac{2\pi V}{\lambda \langle \sigma_a \rangle} \quad (C.6)$$

$$\text{Aperture Leakage } Q_3 = \frac{4\pi V}{\lambda \langle \sigma_l \rangle} \quad (C.7)$$

$$\text{Receiving Antenna Losses } Q_4 = \frac{16\pi^2}{\langle m \lambda^3 \rangle} \quad (C.8)$$

Where in (C.5) $\delta = (2/\omega\mu\omega\sigma\omega)^{1/2}$, $\mu_r = u_\omega/u_o$. The losses due to aperture and receiving antenna are inherent in the data and are not separately studied as that is not the objective here. The antenna mismatch is corrected therefore in (C.8), $m = 1$ and that is for a matched load Q_4 is proportional to frequency cubed. This means that Q_4 is small for low frequencies and is the dominant contributor to the total Q. At high frequencies, Q_4 becomes large and contributes little to the total Q. It is shown in [3] that in the chamber the delay spread of power (τ_{RMS}) is directly related to the Quality factor of the chamber given by (C.9).

$$\tau_{RMS} = \frac{Q_{total}}{\omega} \quad (C.9)$$

In Figure (C.1) the Q of the chamber is plotted as a function of frequency for 5 different loading cases. The variations in the graphs are smoothed by using a 20 MHz window. It is obvious that Q has a strong dependence on frequency and as the loading is increased the loss in the chamber increases which reduces the Q of the chamber.

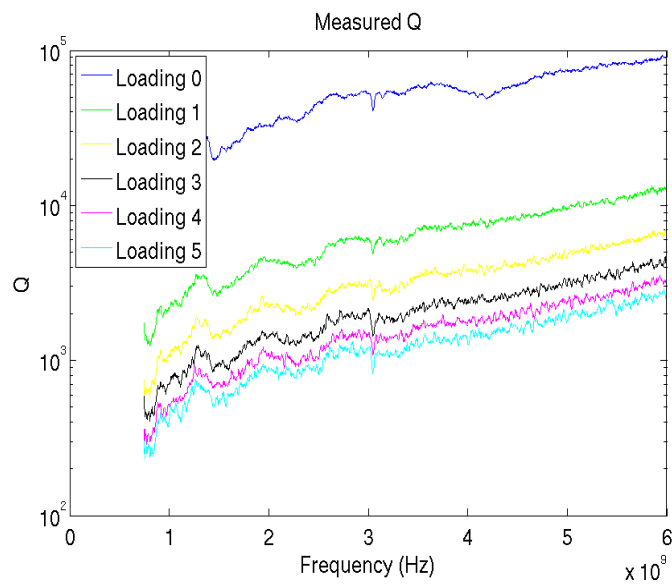


Figure C.1: Chamber Quality Factor as a function of Frequency and Loading

Nomenclature

$2\sigma^2$	Variance of the stirred electric field component (or Power)
σ^2	Variance of the real and imaginary component of stirred electric field
c	Constant for speed of light.
e_{rad}	Radiation efficiency of the antenna.
S_{ji}	Scattering Parameter when port i is excited and response is measured at port j
ACF	Auto-Correlation Function
AFD	Average Fade Duration
AFS	Average Fading Sensitivity
BER	Bit-Error-Rate
DUT	Device Under Test
EM	Electromagnetic
GSM	Global System For Mobile Communication
LCR	Level Crossing Rate
LoS	Line of Sight
LSE	Least Square Error
MIMO	Multiple Input Multiple Output
MLE	Maximum Likelihood Estimation

NIST National Institute of Standards and Technology

PDP Power Delay Profile

RF Radio Frequency

SIMO Single Input Multiple Output

TIS Total Isotropic Sensitivity

VNA Vector Network Analyser

VSA Vector Signal Analyser

VSG Vector Signal Generator

WCDMA Wide-Band Code Division Multiple Access

WLAN Wireless Local Area Network

Index

- Average Fade Duration, 69
- Bit-error-rate measurements, 87
- Channel Impulse Response, 31
- Characterization of Wireless Channel, 105
- Coherence Bandwidth in Reverberation Chamber, 46
- Coherence Time, 53
- Doppler Spread, 70
- Emulating a Wireless Channel in RC, 7
- Fading, 59
- Fast Fading, 65
- Fixed Wireless Communication, 74
- Frequency Domain Channel Sounding, 32
- Frequency sampling, 117
- Impulse Response of a Rayleigh Fading Channel, 32
- Impulse response of a Rician Fading Channel, 44
- Jakes Doppler Spectrum, 74
- K-Factor estimation, 9
- Level Crossing Rate, 66
- Maximum Likelihood Estimation for K-Factor, 13
- Narrowband Fading Model, 107
- Power Delay Profile, 37
- Rayleigh and Rician fading environment, 9
- Rayleigh Distribution, 8
- Sample biasness in the estimation of K-factor, 23
- Slow Fading, 65
- Time-Varying Channel Impulse Response, 106
- Uncertainty in estimation of K-factor, 26
- WCDMA and GSM system level performance of mobile terminals, 91
- Wideband Fading Model, 111

Bibliography

- [1] P. Kildal and K. Rosengren, "Correlation and capacity of mimo systems and mutual coupling, radiation efficiency and diversity gain of their antennas: Simulations and measurements in reverberation chamber," *IEEE Communication Magazine*, vol. 42, no. 12, pp. 102–112, December 2004.
- [2] K. Rosengren, P.-S. Kildal, C. Carlsson, and J. Carlsson, "Characterization of antennas for mobile and wireless terminals in reverberation chambers: Improved accuracy by platform stirring," *Microwave and Optical Technology Letters*, vol. 32, no. 20, pp. 145–149, September 2001.
- [3] D.A.Hill, "Electromagnetic theory of reverberation chambers," National Institute of Standards and Technology, 325 Broadway Boulder, CO, Tech. Rep. 1506, December 1998.
- [4] P.-S. Kildal, *Foundations of antennas: A Unified Approach for Line-Of-Sight and Multipath*. Compendium for the course Antenna Engineering at Chalmers, 2009.
- [5] C. L. Holloway, D. A. Hill, J. M. Ladbury, P. F. Wilson, G. Koepke, and J. Coder, "On the use of reverberation chambers to simulate a Rician radio environment for the testing of wireless devices," *IEEE Transaction on Antennas and Propagation*, vol. 54, no. 11, pp. 3167 – 3177, November 2006.
- [6] S. Rice, "Mathematical analysis of random noise," *Bell System*, vol. 23, no. 3, pp. 282–332, July 1944.
- [7] T. S. Rappaport, *Wireless Communication Principle and Practice*, 2nd ed. Prentice Hall Inc, December 2002, no. 0130422320.
- [8] J. Myung, "Tutorial on maximum likelihood estimation," *Mathematical Psychology*, vol. 47, pp. 90–100, 2003.
- [9] C. Tepedelenlioglu, A. Abdi, and G. B. Giannakis, "Performance analysis of moment-based estimator for the K-factor of the Rice fading distribution," *IEEE Transaction on Wireless Communication*, vol. 2, no. 4, pp. 799 – 810, July 2003.

- [10] D. A. Hill, M. T. Ma, A. R. Ondrejka, B. F. Riddle, M. L. Crawford, and R. T. Johnk, "Aperture excitation of electrically large, lossy cavities," *IEEE Transactions on Electromagnetic Compatibility*, vol. 36, no. 3, pp. 169 – 178, August 1994.
- [11] E. Gender, "Using reverberation chamber to simulate different wireless propagation environments," Master's thesis, Leibniz University Hannover, 2008.
- [12] P. Hallbjörner, "A model for the number of independent samples in reverberation chambers," *Microwave and Optical Technology Letters*, vol. 33, no. 1, pp. 25–28, 2002.
- [13] C. L. Holloway, D. A. Hill, J. M. Ladbury, and G. Koepke, "Requirements for an effective reverberation chamber: Unloaded or loaded," *IEEE Transaction on Wireless Communications on Electromagnetic Compatibility*, vol. 48, no. 1, pp. 187–194, April 2006.
- [14] A. Goldsmith, *Wireless Communications*. Cambridge University Press, September 2005.
- [15] C. L. Holloway, M. G. Cotton, and P. McKenna, "A model for predicting the power delay profile characteristics inside a room," *IEEE Transactions on Vehicular Technology*, vol. 48, no. 4, pp. 1110–1120, August 2002.
- [16] X. Chen, P.-S. Kildal, C. Orlenius, and J. Carlsson, "Channel sounding of loaded reverberation chamber for over-the-air testing of wireless devices-coherence bandwidth versus average mode bandwidth and delay spread," *IEEE Antennas and Wireless Propagation Letters*, vol. 8, pp. 678 – 681, July 2009.
- [17] E. Genender, C. L. Holloway, K. A. Remley, J. M. Ladbury, G. Koepke, and H. G., "Simulating the multipath channel with a reverberation chamber: Application to Bit-Error-Rate measurements," *IEEE Transactions on Electromagnetic Compatibility*, vol. 52, no. 4, p. 766, November 2009.
- [18] X. Chen and P.-S. Kildal, "Theoretical derivation and measurement of the relationship between coherence bandwidth and rms delay spread in reverberation chamber," *3rd European conference on antenna and propagation*, pp. 2687–2690, March 2009.
- [19] C. L. Patane, "Reverberation chamber performance and methods for estimating the rician k-factor," Master's thesis, CHALMERS University of Technology, September 2010, (done at NIST in Boulder, CO. Examiner: Kildal, Supervisor: Kate Remley, NIST).
- [20] G. L. Stuber, *Principles of wireless Communications*, 2nd ed. Kluwer Academic Publishers, 2001.

- [21] K. Karlsson, X. Chen, and P.-S. Kildal, "Doppler spread in reverberation chamber predicted from measurements during stationary step-wise stirring," *Antennas and Wireless Propagation Letters*, vol. 9, pp. 497 – 500, May 2010.
- [22] P. Kaveh and A. H. Levesque, *Wireless Information Networks*, 2nd ed. A John Wiley and Sons Inc, September 2005.
- [23] W. C. Jakes, *Microwave Mobile Communication*. Wiley, New York, 1974.
- [24] S. Theon, L. V. der Perre, and M. Engels, "Modeling the channel time-variance for fixed wireless communication," *IEEE Communication Letters*, vol. 6, no. 8, pp. 331 – 333, August 2002.
- [25] A. Domazetovic, L. J. Greenstein, N. B. Mandayam, and I. Seskar, "Estimating the doppler spectrum of a short-range fixed wireless channel," *IEEE Communications*, vol. 7, no. 5, pp. 227 – 229, May 2003.
- [26] R. Feick, R. A. Valezuela, and L. Ahumada, "Experimental results on the level crossing rate and average fade duration for urban fixed wireless channels," *IEEE Transaction on Wireless Communications*, vol. 6, no. 1, pp. 175 – 179, January 2007.
- [27] K. A. Remley and C. R. Wright, "A simplified method for evaluating OTA device performance using industry standard models in a uniform environment," National Institute of Information Technology and Azimuth Systems Inc, Tech. Rep., June 2010, presented at COST 2100.
- [28] P.-S. Kildal and C. Carlsson, "Detection of a polarization imbalance in reverberation chambers and how to remove it by polarization stirring when measuring antenna efficiencies," *Microwave and Optical Technology Letters*, vol. 32, no. 32, pp. 145–397, July 2002.
- [29] K. Rosengren, P.-S. Kildal, C. Carlsson, and J. Carlsson, "Characterization of antennas for mobile and wireless terminals in reverberation chambers: Improved accuracy by platform stirring," *Microwave and Optical Technology Letters*, vol. 30, no. 20, pp. 391–379, September 2001.
- [30] C. Orlenius, P.-S. Kildal, and G. Poilasne, "Measurements of total isotropic sensitivity and average fading sensitivity of CDMA phones in reverberation chamber," in *IEEE AP-S International Symposium, Washington D.C.*, 3-8 July 2005.
- [31] P.-S. Kildal and C. Orlenius, "TRP and TIS/AFS measurements of mobile station in a reverberation chamber," March 2009, contribution to CTIA working group.
- [32] W.C.Jakes, "A statistical theory of mobile radio reception," Bell System Tech, Tech. Rep., 1968.